



저작자표시-비영리-변경금지 2.0 대한민국

이용자는 아래의 조건을 따르는 경우에 한하여 자유롭게

- 이 저작물을 복제, 배포, 전송, 전시, 공연 및 방송할 수 있습니다.

다음과 같은 조건을 따라야 합니다:



저작자표시. 귀하는 원저작자를 표시하여야 합니다.



비영리. 귀하는 이 저작물을 영리 목적으로 이용할 수 없습니다.



변경금지. 귀하는 이 저작물을 개작, 변형 또는 가공할 수 없습니다.

- 귀하는, 이 저작물의 재이용이나 배포의 경우, 이 저작물에 적용된 이용허락조건을 명확하게 나타내어야 합니다.
- 저작권자로부터 별도의 허가를 받으면 이러한 조건들은 적용되지 않습니다.

저작권법에 따른 이용자의 권리는 위의 내용에 의하여 영향을 받지 않습니다.

이것은 [이용허락규약\(Legal Code\)](#)을 이해하기 쉽게 요약한 것입니다.

[Disclaimer](#)

공학박사 학위논문

**Shock Wave Formation via
Streamer-to-arc Transition in
Underwater Pulsed Spark Discharge**

수중 펄스 스파크 방전에서
스트리머-아크 천이에 의한 충격파의 생성

2019년 2월

서울대학교 대학원

에너지시스템공학부

이 건

Shock Wave Formation via Steamer-to-arc Transition in Underwater Pulsed Spark Discharge

지도교수 정 경 재

이 논문을 공학박사 학위논문으로 제출함

2018년 10월

서울대학교 대학원

에너지시스템공학부

이 건

이 건의 공학박사 학위논문을 인준함

2019년 1월

위 원 장 황 용 석 (인)

부위원장 정 경 재 (인)

위 원 김 곤 호 (인)

위 원 고 광 철 (인)

위 원 김 덕 규 (인)

Abstract

Shock Wave Formation via Streamer-to-arc Transition in Underwater Pulsed Spark Discharge

Kern Lee

Department of Energy System Engineering

The Graduate School

Seoul National University

Underwater pulsed spark discharge (PSD) is accompanied by an energetic and transient plasma that actively interacts with a surrounding water. The underwater PSD can be produced by applying a high voltage (HV) pulse across a pair of electrodes and distinguished by a large input energy (> 100 J/pulse). The electrical power deposited to the spark plasma drives the rapid expansion of the spark plasma, and the subsequent build-up of shock wave in the surrounding water. Hence, at Seoul National

University, the underwater PSD technique has been studied as a strong shock wave source that can be controlled by electrical parameters. This technique has been mainly applied to the cleaning of well screens that are clogged by incrustations in the ground water intake system and the green algae treatment in the drinking water resource facility.

A typical procedure of the underwater PSD is as follows. When the HV pulse is applied to the water gap, Joule heating is initiated in the electrode tip vicinities. After a certain formative time, vapor bubbles will emerge and expand. Then, a surface protrusion can be formed as a result of an electro-hydrodynamic (EHD) instability. This protrusion will soon be transformed into a streamer and propagate toward the opposite electrode. Finally, the electrical breakdown occurs when this underwater streamer touches the opposite electrode. At this moment, the spark plasma can be almost instantaneously formed (within several nanoseconds) from streamers, and experiences a large change in its physical properties. In particular, the electrical property of spark plasma plays an essential role in shock wave formation because it determines the power coupling between the plasma load and the pulsed power system.

In this work, the experimental observations on the time-varying characteristics of underwater streamer have been made to determine the initial state of spark plasma. Also, significant efforts have been paid to elucidate the formative process of shock wave using the self-consistent simulation model of spark discharges. Hence, the dynamic evolution of plasma parameters and the resulting hydraulic

phenomena could be described simultaneously.

A novel experimental method is proposed to characterize the subsonic streamers and observe their rapid transition to the arc state. The PSD has been operated in a negative subsonic mode of which discharge is initiated from the cathode side. Comparing with a conventional positive polarity mode, the negative subsonic streamer has a tree-like structure without large bubble clusters around the stalk and has a faster propagation speed, so that a more efficient shock formation could be expected when it causes the electrical breakdown. The slow bubble formation process due to the screening effect, which is the practical limitation of the negative discharge mode, has been successfully compensated by preconditioning the gap with water electrolysis. In the presence of initial hydrogen bubbles produced at the cathode surface, the overall pre-breakdown process could be remarkably accelerated, and thus the uncertainty originated from the stochastic nature of bubble formation has been minimized. In order to measure the time-varying characteristics of underwater PSD, the optical diagnostics are established: the shadowgraphy and the optical emission spectroscopy (OES). The hydrodynamic features of underwater streamer and spark channel are obtained from shadowgraph images, while the electron density of discharge plasma is determined by OES analysis.

With an aid of initial hydrogen bubbles in merged form, which are produced by sufficiently long electrolysis treatment, the streamer discharge could be directly ignited without additional bubble formation. The current-voltage fluctuation caused

by the charging effect of long coaxial cable (93 m) is synchronized with the electron density (n_e) variation of the internal bubble discharge, however there was no abrupt change in n_e at the moment of streamer inception. Instead, the rapid increase of n_e at a channel base is accompanied by the sudden increase of streamer propagation speed, so it is found that there is a propagation mode transition from electrohydrodynamic (EHD) to Ohmic regime. For the mode transition, the threshold n_e value at the channel base appears to be $5\text{-}8 \times 10^{17} \text{ cm}^{-3}$, and this condition is satisfied earlier in a higher conductivity water. At the moment of breakdown, the electron density (n_e) measured at head region was so high ($\sim 10^{19} \text{ cm}^{-3}$) that the four-fold variation of n_e could emerge along the channel length. Along with the measured n_e values, the radial structure of initial spark channel observed by shadowgraphy has been used in the simulation study.

For the comprehensive understanding that relates the streamer's characteristics with the formative process of shock wave, one-dimensional simulation model of spark discharge has been used intensively. Since we attempted to control the rate of streamer-to-arc transition by the length of transmission line, the pulse shaping effect became pronounced especially in the early phase of channel expansion. In this regard, the simulation model has been improved to simply calculate the electrical power transmission by treating the cable as the series connections of small segment which contains the resistor, inductor, and capacitor assembled in the shape of capital letter *T*. The numerical results demonstrated that the underwater streamer plays an

essential role in the shock wave formation by determining the shape and composition of the initial spark plasma. In fact, there found a cold layer surrounding the highly conductive core in the initial spark channel experimentally. Corresponding initial profiles of the plasma density and temperature make the outer layer to act as a shock absorber, the formation of shock wave slows down. In addition, as the internal pressure wave is dissipated within this outer layer, the initial expansion of spark channel is further influenced by the pulse forming action of the coaxial cable. Accordingly, the strong dependence of the measured peak pressure on the breakdown voltage for different cable lengths has been successfully reproduced by the numerical model. During the early phase of streamer-to-arc transition that mostly determines the physical properties of shock front, relatively low plasma temperature makes the radiation absorption length larger than the plasma dimension. Thus, the shock wave formation process can be reasonably described without considering the re-absorption of radiation power inside the plasma volume. It is also revealed that even though the current rise rate is much increased, the energy transfer efficiency to the hydraulic motion becomes significantly degraded by the rapidly increasing radiation loss.

Keywords; Underwater pulsed spark discharge, Shock wave, Streamer-to-arc transition, Pre-breakdown acceleration, Negative subsonic streamer, Electrolysis, Self-consistent simulation, Transmission line model

Student Number: 2012-21007

Contents

Abstract	i
Contents	vi
List of Figures	x
List of Tables	xx
Chapter 1. Introduction	1
1.1. Underwater Pulsed Spark Discharge	1
1.1.1. Subsonic Regime of Underwater Discharges	4
1.1.2. Bubble Mechanism	8
1.1.3. Applications of PSD Technique.....	11
1.2. Previous Work and Research Motivation	20
1.3. Author’s Contribution and Scope of Study	31
Chapter 2. Experimental Setup and Diagnostics	35
2.1. Capacitive Discharge System	35
2.2. Electrical Measurements.....	39
2.3. Shadowgraph Imaging	40

2.3.1. Principles	40
2.3.2. Optical Arrangement.....	43
2.4. Optical Emission Spectroscopy (OES)	45
2.4.1. Methods of Electron Density Measurement	46
2.4.2. Design of Spectrograph for Time-resolved OES	50
2.4.3. Calibration and Data Process.....	56
2.5. Limitations of Experiment	62

Chapter 3. Advanced Self-consistent Circuit Model of Spark

Discharge	64
3.1. Advanced Circuit Model Coupled with Magneto-hydrodynamics (MHD) Code	64
3.1.1. MHD Equations and Material Model	64
3.1.2. Initial Profile of Spark Plasma Parameters	74
3.1.3. Advanced Circuit Model.....	77
3.2. Improvements of Numerical Results	85
3.3. Limitations of Model.....	91

Chapter 4. Characterization of Negative Subsonic Streamers

.....	94
-------	-----------

4.1. Preliminary Experiments	94
4.1.1. Over-voltage Electrolysis	94
4.1.2. Role of Initial Bubbles.....	100
4.2. Streamer Initiation.....	107
4.3. Streamer Propagation	116
4.4. Streamer-to-arc Transition.....	126

Chapter 5. Development of Underwater Shock Wave by Pulsed

Spark Discharge 132

5.1. Shock Wave Formation via Streamer-to-arc Transition	132
5.1.1. Experimental Observations.....	133
5.1.2. Role of Outer Shell	144
5.2. Evolution of Spark Channel	152
5.2.1. Influence of Radiation Loss.....	153
5.2.2. Discussions on Gas Composition	161

Chapter 6. Conclusions and Recommendations for Future

Work 167

6.1. Summary and Conclusions	167
6.2. Recommendations for Future Work	171

Bibliography	174
Abstract in Korean	184

List of Figures

Figure 1.1.	(a) Circuit diagram of capacitive discharge system for underwater pulsed spark discharges and (b) typical waveforms of current, voltage and pressure	2
Figure 1.2.	Shadowgraph images of subsonic streamers in PSD: (a) positive and (b) negative streamers.....	6
Figure 1.3.	(a) Schematic diagram of experimental setup for the pilot-scale test: (1) pulsed power system, (2) coaxial cable, (3) spark generator, (4) well screen, (5) gravel pack, and (6) water. (b) Detailed cross-sectional view of the spark generator [16].....	12
Figure 1.4.	The camera images of well interior before and after the well cleaning are compared at three different well positions of 4.0, 4.5, and 5.0 m [16].....	13
Figure 1.5.	Plot of head ratio versus time obtained from the slug tests carried out before and after the well cleaning [16]	14
Figure 1.6.	Schematic diagram of the horizontal well and PSD cleaning system [36]	16
Figure 1.7.	Comparison of camera images before and after the cleaning of horizontal well by underwater PSD [35].....	16
Figure 1.8.	Schematic of a green algae treatment system installed on a sedimentation pond of the water purification plant.....	18
Figure 1.9.	Comparison of (a) camera images and (b) TEM images for the specimens with and without PSD treatment	19
Figure 1.10.	Schematic diagram of the equivalent circuit for the well cleaning system [16]	25
Figure 1.11.	Flow of calculation for the self-consistent simulation of underwater PSD given in Ref. [16]	26

Figure 1.12.	Spatial distribution of (a) pressure, (b) velocity, and (c) mass density at each time during the expansion of the spark channel calculated for the charging voltage of 14 kV. The position of peak velocity indicates the radius of the spark channel, or the interface between the spark channel and liquid water [16]28
Figure 2.1.	(a) A schematic diagram of the pulsed-spark discharge system and (b) a drawing of the electrode assembly36
Figure 2.2.	Circuit diagram of the triggered spark gap switch for high-side operation38
Figure 2.3.	Plan view of schematic for the layout of the optical diagnostic system.41
Figure 2.4.	(a) Side view of schematic for the focused shadowgraphy and (b) emission, transmission curves of the light-emitting diode and the band-pass filter [57].....43
Figure 2.5.	An example of a processed shadowgraph image45
Figure 2.6.	Dependence of the H_{α} FWHM and of the FWHA with the every combinations of T and μ considered in the simulations [66]...49
Figure 2.7.	(a) Overview of the emission spectra of underwater PSD produced in tap water ($\sim 230 \mu\text{S cm}^{-1}$) with an initial voltage of 16 kV, and (b) the raw spectrum image. This spectrum is acquired at $\sim 2 \mu\text{s}$ before the breakdown using the wide-range VPHG spectrograph.52
Figure 2.8.	Schematic drawing for the trajectories of (a) the chief-ray of central wavelength (λ_c) around the grating and (b) the chief-rays of diffracted wavelength near the imaging plane54
Figure 2.9.	Spectrum profile of the hydrogen lamp measured with VPHG spectrograph.....57
Figure 2.10.	Spectrum profile of the neon lamp (NE-1) measured with (a)

	commercial high-resolution spectrograph (Princeton Instrument, Acton 2500i) and (b) VPHG spectrograph	58
Figure 2.11.	The efficiency coefficient curve of the VPHG spectrograph.....	59
Figure 2.12.	Example fit of the H_{α} line of the underwater streamer. Emission spectra is measured with VPHG spectrograph and the picture on the upper-right corner shows a light collecting area focused on the cathode tip vicinity	60
Figure 3.1.	Maps for (a) the electron density and (b) electrical conductivity of water plasma calculated by Chung's LTE model [53]. The plot range is adjusted near the initial plasma condition of PSD	70
Figure 3.2.	Comparison of (a) non-ideality parameter, (b) pressure, (c) electrical conductivity, and (d) internal energy calculated with different ionization potential models for water plasma at 10^4 K	72
Figure 3.3.	Comparison of (a) non-ideality parameter, (b) pressure, (c) electrical conductivity, and (d) internal energy calculated with different ionization potential models for water plasma at 5×10^4 K	73
Figure 3.4.	Comparison of (a) non-ideality parameter, (b) pressure, (c) electrical conductivity, and (d) internal energy calculated with different ionization potential models for water plasma at 10^5 K	73
Figure 3.5.	Comparison of (a) non-ideality parameter, (b) pressure, (c) electrical conductivity, and (d) internal energy calculated with different ionization potential models for water plasma at 5×10^5 K	73
Figure 3.6.	Example of the radial profiles of (a) temperature, (b) electrical conductivity, (c) electron density for initial spark plasma having a	

	Gaussian-like temperature distribution.....	76
Figure 3.7.	Schematic for fitting the electrode outline to correct the axial field strength	77
Figure 3.8.	Circuit representations of (a) capacitive discharge system and (b) T-section model for transmission line.....	78
Figure 3.9.	Flow of calculation in the improved simulation model	82
Figure 3.10.	Comparison of numerical results by different power transmission models in the early stage of spark discharges with short (1.3 m) and long (93 m) cables: (a) probe current, (b) probe voltage, (c) plasma resistance, (d) delivered power, (e) radial expansion speed, and (f) wall pressure at 1 cm	86
Figure 3.11.	Comparison of current and voltage waveforms measured at inlet side of cable, with numerical results for different cable lengths: (a) 15 m and (b) 125 m.....	88
Figure 3.12.	Variation of parameters that contribute to the development of shock waves with cable lengths: (a) ratio between t^* and t_p , (b) energy delivered to the spark channel until t^* , and (c) peak pressure normalized by result of 15 m-long cable. Comparison of numerical results from new and old models.....	89
Figure 4.1.	Electrolysis of tap water ($230 \mu\text{S cm}^{-1}$) via preconditioning pulse: (a) shadowgraph images of the water gap with an exposure time of $0.3 \mu\text{s}$ and (b) synchronized gap voltage and discharge current waveforms.	96
Figure 4.2.	Shadowgraph images obtained from electrolysis of NaCl solution at different conductivity: (a) $500 \mu\text{S cm}^{-1}$ and (b) $750 \mu\text{S cm}^{-1}$	97
Figure 4.3.	Shadowgraph images obtained from electrolysis of NaCl solution ($500 \mu\text{S cm}^{-1}$) at different pressure: (a) 2 atm, (b) 3 atm	98

Figure 4.4.	Influence of the preconditioning pulse on the pre-breakdown process: measured waveforms of (a) gap voltage and (b) pre-breakdown current. The data closest to the average of 10 repeated shots were selected for display. Both the breakdown delay (τ_{bd}) and breakdown voltage (V_{bd}) values are from the waveforms shown in the figure. 101
Figure 4.5.	Initiation of bubbles and streamers at a charging voltage of 17 kV: (a) without and (b) with a preconditioning pulse (400 V, 250 ms) before the HV pulse application. The shadowgraph images shown in (a) and (b) are synchronized with the waveforms indicated by the black and blue lines, respectively, in Fig. 4.4. 103
Figure 4.6.	Influence of electrolysis pulse duration on breakdown parameters: energies required for preconditioning treatment (W_{pc}) and the entire discharge ($W_{tot} = W_{pc} + W_{pb}$), the pre-breakdown delay (τ_{bd}), and the measured peak pressure (P_{pk})..... 104
Figure 4.7.	Voltage, current, and pressure waveforms for an initial charging voltage of 17 kV: (a) without and (b) with a preconditioning pulse (400 V, 250 ms)..... 105
Figure 4.8.	Two different mode of streamer initiation: (a) pre-breakdown current waveform, shadowgraph images of (b) fast and (c) slow ignition mode. 107
Figure 4.9.	Evolutions of (a) the channel resistance and (b) the electron density measured at the channel base. Data are compared for different water conductivity at the same initial charging voltage (V_0) of 20kV..... 109
Figure 4.10.	An example of emission spectrum acquired from the initial bubble discharge. The discharge is produced at initial voltage (V_0) of 20 kV and water conductivity of $750 \mu\text{S cm}^{-1}$. A shadowgram is

	placed on the right-face.	110
Figure 4.11.	Initial bubble discharge under the current-voltage fluctuation induced by a long coaxial cable (93 m): (a) pre-breakdown current, (b) gap voltage, and (c) shadowgraph images. The initial voltage (V_0) is 20 kV and the water conductivity is $750 \mu\text{S cm}^{-1}$	111
Figure 4.12.	A series of emission spectra acquired from the initial bubble discharge under the current-voltage fluctuation. The initial voltage (V_0) is 20 kV and the water conductivity is $750 \mu\text{S cm}^{-1}$	112
Figure 4.13.	Comparison of pre-breakdown processes with different cable length (1.3 and 93 m): (a) pre-breakdown current, (b) gap voltage, and (c) electron density of channel base.....	114
Figure 4.14.	Shadowgraph images of PSD with slow ignition mode. The discharge is produced at initial voltage (V_0) of 21 kV, preconditioning duration of 170 ms, water conductivity of $500 \mu\text{S cm}^{-1}$, and hydrostatic pressure of 3 atm	115
Figure 4.15.	Comparison of pre-breakdown processes with the different number of main streamer channel: (a) pre-breakdown current, (b) gap voltage, and (c) channel resistance. Shadowgraph images are correspond to (d) dual (#8) and (e) single (#6) streamer cases, respectively	116
Figure 4.16.	Comparison of streamer propagation for different water conductivity (250 and $750 \mu\text{S cm}^{-1}$): (a) effective channel length and (b) propagation speed. Shadowgraph images are obtained from conditions: (c) $250 \mu\text{S cm}^{-1}$, 16 kV, (d) $250 \mu\text{S cm}^{-1}$, 20 kV, and (e) $750 \mu\text{S cm}^{-1}$, 20 kV, respectively.....	118
Figure 4.17.	Measured parameters during the pre-breakdown period: (a) pre-breakdown current, (b) effective channel length, (c) propagation speed, and (d) electron density at channel base for water	

	conductivity of $250 \mu\text{S cm}^{-1}$, and (e)-(f) for water conductivity of $750 \mu\text{S cm}^{-1}$	120
Figure 4.18.	Evolution of channel resistance during the streamer propagation for different water conductivity (250 and $750 \mu\text{S cm}^{-1}$)	121
Figure 4.19.	Shadowgraph images of streamer propagation in the presence of fluctuating current-voltage induced by long coaxial cable (93 m). The images are acquired from different shot: (a) #1, (b) #8, where the water conductivity is $500 \mu\text{S cm}^{-1}$ and initial charging voltage is 20 kV	122
Figure 4.20.	Comparison of streamer propagation at different cable length: (a) pre-breakdown current, (b) gap voltage, and (c) propagation speed for 93 m-long cable, and (d)-(f) for 1.3 m-long cable	123
Figure 4.21.	Streamer propagation at 1 and 3 atm condition: (a) pre-breakdown current, (b) gap voltage, (c) effective channel length, and (d) propagation speed. Shadowgraph images of discharge in slow ignition mode under conditions (e) preconditioning duration of 70 ms at 1 atm and initial voltage of 21 kV and (f) preconditioning duration of 170 ms at 3 atm and initial voltage of 18 kV	124
Figure 4.22.	Evolution of (a) electron density measured at channel base and (b) channel resistance. Discharge conditions are the same as data presented in Fig. 4.21.....	125
Figure 4.23.	Electrical measurements on the streamer-to-arc transition: (a) current, (b) gap voltage, and (c) channel resistance for different water conductivities, and (d)-(f) for different hydrostatic pressures	127
Figure 4.24.	Electrical measurements on the streamer-to-arc transition: (a) current, (b) gap voltage, and (c) channel resistance for different breakdown voltages, and (d)-(f) for different cable lengths	128

Figure 4.25.	(a) Electron density measured at different vertical position of discharge channel and (b) example of H_{α} line spectrum acquired at Z5 position marked in the shadowgram.....	129
Figure 5.1.	Variation of measured peak pressure with respect to the breakdown voltage for different (a) water conductivity, (b) hydrostatic pressure, and (c) cable length.	134
Figure 5.2.	Shadowgraph images of the spark channel and shock wave. Images are acquired from different cable lengths: (a) 1.3 m, (b) 93 m. The breakdown delays are 30.9 and 29.6 μs , respectively.....	136
Figure 5.3.	Shadowgraph images processed to measure the time-varying channel radius and shock position for different cable lengths: (a) 1.3 m and (b) 93m. Discharges are produced at water conductivity of $500 \mu\text{S cm}^{-1}$ and initial charging voltage of 20 kV. Dashed line indicates the breakdown moment	138
Figure 5.4.	Measured parameters during the streamer-to-arc transition for different cable lengths: (a) breakdown current, (b) gap voltage, (c) channel resistance, (d) delivered power, (e) channel radius and shock position, and (f) pressure waveform measured at 10 cm away from the water gap.....	140
Figure 5.5.	Shadowgraph images showing the structure of underwater shock waves produced at different cable lengths: (a) 1.3 m and (b) 93 m. The water conductivity is $500 \mu\text{S cm}^{-1}$ and the initial voltage is 20 kV	142
Figure 5.6.	Measured waveform from the underwater electrical wire explosion: (a) discharge current, (b) voltage, (c) pressure, and (d) shadowgraph images. The dimension of Cu wire and initial voltage are marked on the top of figure.....	143
Figure 5.7.	Comparison of numerical results based on different initial	

	temperature profile of spark plasma and experimental results: (a) channel resistance, (b) delivered power, and (c) channel radius	146
Figure 5.8.	Comparison of numerical results based on different initial temperature profile of spark plasma and experimental results: (a) the expansion speed of spark channel and (b) the pressure at probing position (10 cm)	147
Figure 5.9.	Spatial distribution of pressure at each time during the expansion of spark channel for different initial plasma structure in the (a) initial phase and (b) longer time period	149
Figure 5.10.	Variations of (a) expansion speed, (b) effective input energy, and (c) wall pressure (at 10 cm) calculated with increasing cable length	150
Figure 5.11.	Comparison of measured peak pressure with numerical results calculated for different cable lengths with increasing breakdown voltage	151
Figure 5.12.	Influence of radiation loss on numerical results: (a) current and (b) voltage for the 1.3 m, and (c)-(d) for the 93 m cables, respectively	153
Figure 5.13.	Numerical results for different cable length and experimental results: (a) channel resistance, (b) delivered power, and (c) channel radius. The influences of radiation loss are compared.....	154
Figure 5.14.	Influence of radiation loss on (a) the expansion speed and (b) the wall pressure	156
Figure 5.15.	Comparison of delivered power and radiation loss calculated under the assumption of optically thin, or no radiation loss	157
Figure 5.16.	Radial profiles of (a) temperature and (b) Planck mean free path calculated for 1.3 m-long cable case, and (c)-(d) for 93 m-long	

	cable case	159
Figure 5.17.	Maps for (a) the electron density and (b) electrical conductivity of hydrogen plasma. The plot range is adjusted near the initial plasma condition of PSD	163
Figure 5.18.	Comparison of electrical conductivities calculated by the this work and those by Capitelli [96] for constant pressure of 1, 10, and 100 atm	163
Figure 5.19.	Electrical conductivity maps for (a) the water plasma and (b) hydrogen plasma in higher temperature region.	164
Figure 5.20.	Comparison of electrical conductivities of water and hydrogen plasmas calculated at the sampled mass density ratios: $10^{-3} - 1$ for hydrogen and $10^{-5} - 10^{-3}$ for water.....	165

List of Tables

Table 1.1.	Morphological features of underwater streamers in subsonic regime for each polarity [4, 6, 10, 11].....	7
Table 1.2.	Comparison of present model with previous work.	30
Table 3.1.	Simulation parameters of PSD system.	80

Chapter 1. Introduction

1.1. Underwater Pulsed Spark Discharge

Pulsed spark plasmas generated by underwater electrical discharge are short-living and highly energetic plasmas that actively interact with surrounding water in a variety of ways. In particular, electrical and thermodynamic properties of spark plasma are of a special interest because they are closely linked to the pulsed power system, so a comprehensive understanding of entire system becomes very complicated. Here, the term *spark* means the transient state to become a state of an *arc* plasma, by definition. Therefore, the spark plasma tends to be localized in a small spatial dimension (\sim mm) and its properties rapidly change in time (\sim μ s).

The underwater pulsed spark discharges (PSD), also called electrohydraulic discharges can be distinguished by large input energy (> 100 J/pulse, up to several tens of kilojoules). This type of discharge converts the electrical energy into the kinetic energy of hydraulic motion of surrounding water, and emits intense radiation. Strong shock wave also can be easily formed due to the low compressibility of water which resists to the expanding motion of spark plasma. As depicted in Fig. 1.1(b), a typical PSD process can be divided into a pre-breakdown period and a breakdown period by an impedance of water gap. In the case of capacitive discharge circuit, which is a conventional power system driving the underwater PSD, its circuit response

almost instantaneously transit from an overdamping-state into an underdamping-state, at the onset of breakdown. Although there are still several missing links between the physical processes of the pre-breakdown and breakdown periods, one can presume that the initial condition of spark plasma will be determined as a result of the pre-breakdown process.

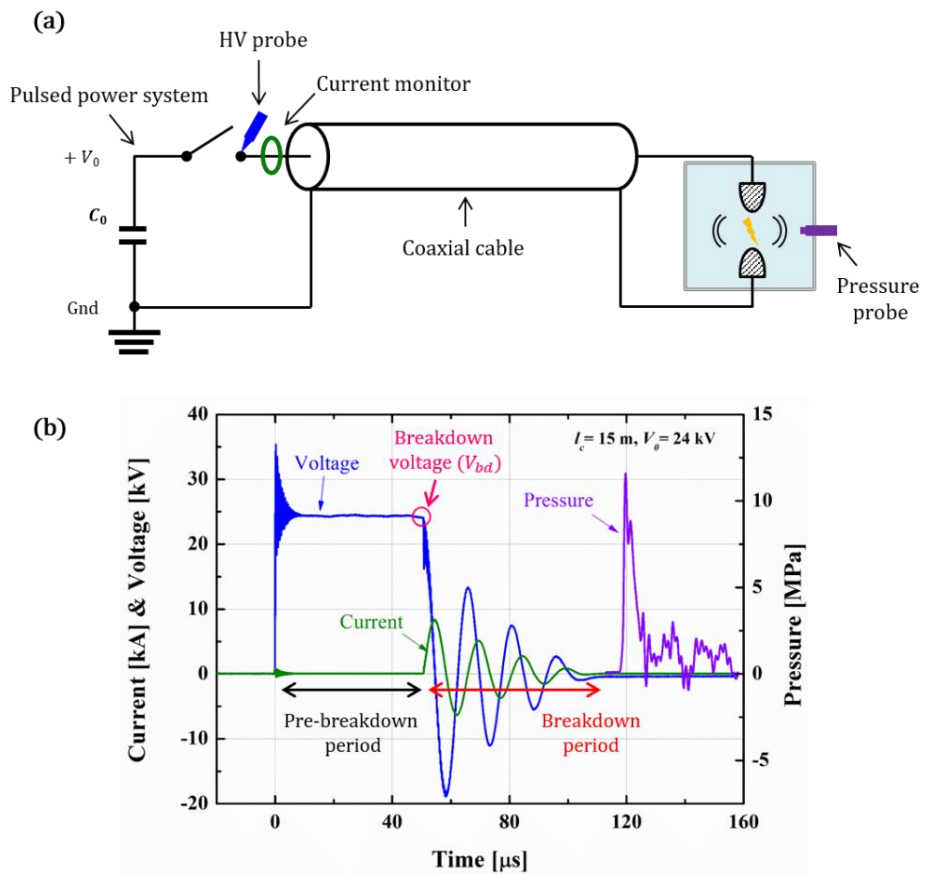


Figure 1.1. (a) Circuit diagram of capacitive discharge system for underwater pulsed spark discharges and (b) typical waveforms of current, voltage and pressure.

The pre-breakdown process of the underwater PSD can be described by the well-known bubble theory [1]. When a high-voltage (HV) pulse is applied across the water gap (i.e., pair of electrodes immersed in water), localized Ohmic heating begins in the region of strong electric field, and subsequently forms a layer of vapor bubbles. From this layer, plasma discharges called streamers can be initiated, and they propagate toward the opposite electrode to cause the final breakdown. The formation of vapor bubbles tends to require a large amount of energy in PSD system because the electrode tips are bluntly shaped to withstand surface erosion that is caused by the arc plasma developed in the breakdown period. Considering that most industrial PSD applications are operated in the high conductivity liquid ($\geq 100 \mu\text{S cm}^{-1}$), the energy loss problem during the pre-breakdown period becomes even more serious. Since this energy loss is a direct consequence of the over-damping RC (resistance-capacitance) decay of power system, the remaining energy at breakdown moment will decrease as more energy is dissipated during this period.

The breakdown delay (τ_{bd}), defined as a time duration between the application of HV pulse and the onset of breakdown, consists of four components: the time of bubble formation (τ_{bub}), the time of bubble growth and expansion (τ_{ex}), the time of avalanche growth inside a bubble (τ_{ar}), and the time of streamer propagation (τ_{prop}) [2]. In the case of PSD, the bubble formation process is so slow that accounts for more than 50% of the entire pre-breakdown period. It explains the reason why the existence of pre-existing bubbles is particularly important in PSD systems because the

bubble formation time can be significantly reduced by them. It should be noted that the propagation speed of the underwater streamer is usually slower than the sound speed of water ($c_0 \sim 1.5$ km/s), so this type of discharge is also called underwater subsonic discharges [3, 4].

This chapter has been constructed to address the main purpose and the scope of this study based on understanding salient features of the underwater PSD. Hence, some brief reviews on the several subjects related to the characteristics of underwater streamers, the bubble mechanism, and some applications of PSD will be placed in the remaining part of this section.

1.1.1. Subsonic Regime of Underwater Discharges

In a number of literatures, the term *streamers* has been widely used for luminous plasma channels appearing between the HV applied electrodes and propagate toward the opposite electrode. However, except for the similarity in their appearance, the streamers produced in liquid phase is completely different in characteristics and physical nature from the classical streamers in gas discharges [3, 5]. The characteristics of the underwater streamer tend to greatly depend on the reactor configuration, liquid properties, gas-liquid phase distribution, shape of HV pulse, and other operating conditions. In the case of PSD, the underwater streamers have been categorized according to their propagation speed and polarity [3-6]. Figure 1.2 shows

shadowgraph images of typical underwater streamers in PSD. In the subsonic discharge regime, the external shape of the underwater streamer becomes greatly different with its polarity. The positive streamer (cathode-directed streamer) has a volcano-like structure in the form of largely diffused bubble cluster. When this positive streamer gets close to the cathode, a secondary streamer with supersonic velocity can be initiated from its head. On the contrary, the negative streamer (anode-directed streamer) has a tree-like or bush-like structure with many filamentary branches around the stalk. The polarity effect on this morphological difference is mainly due to the different mobility of main charge carrier for each polarity [7]: $\mu_e \sim 100 \text{ cm}^2 \text{ V}^{-1} \text{ s}^{-1}$ for electrons [8] and $\mu_i \sim 1.31 \times 10^{-3} \text{ cm}^2 \text{ V}^{-1} \text{ s}^{-1}$ for ions [9] in water, respectively. In fact, the discharge shape observed by the optical visualization techniques such as shadowgraphy or Schlieren imaging is the external structure formed by hydrodynamic effect rather than the electronic effect. Thus, the discharge shapes of both polarity indicate that a certain amount of gas layer is formed around the highly conductive plasma channel. In a positive streamer, high mobility electrons can be transferred through the plasma channel to the anode while low mobility ions stay in the streamer region. Because of the positive charges accumulated in the head region, negative ions in the surrounding water are attracted to form another layer of negative charges. The resulting induced field exerts in outward direction, contributing to the active lateral expansion of positive streamers. In contrast, electrons are accumulated at the head region of the negative streamer but the positive ions are

so sluggish that cannot be transferred to the cathode [6]. In the presence of a gas layer containing large amount of oxygen and water vapor, the electrons injected from the streamer head will be easily attached to these molecules to form a negative charge layer. The electric field induced by this charged layer and sluggish ions staying in the negative streamer also exerts outwards, but its net intensity is much weaker than that of positive streamer. Consequently, the lateral expansion of the negative streamer becomes much slower than in the positive polarity case. Compared to the negative streamers, the larger head radius of positive streamers is primarily responsible for its slower propagation speed, because the local enhancement of the electric field is degraded by diffused structure of streamer head [6]. The salient features of the subsonic discharges can be summarized as Table 1.1.

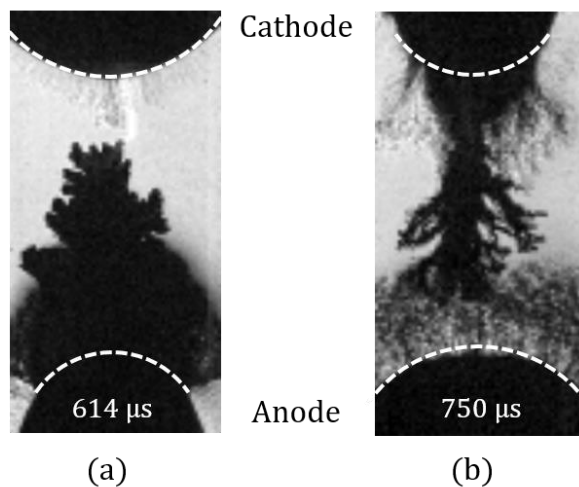


Figure 1.2. Shadowgraph images of subsonic streamers in PSD: (a) positive and (b) negative streamers.

Table 1.1. Morphological features of underwater streamers in subsonic regime for each polarity [4, 6, 10, 11].

	<i>Positive</i>	<i>Negative</i>
<i>Morphology</i>	Volcano-like	Tree-like
<i>Main charge of streamer head</i>	Positive ion	Electron + sluggish ion
<i>Propagation speed</i>	Slower (<100 m/s)	Faster (<1 km/s)

In many industrial applications, the Martin's empirical formula has given practical relation of the dielectric strength (E_{bd}), effective pulse duration (τ), and exposed electrode area (A) [12, 13]. This formula is constructed for large electrode separations in the centimeter range and large electrode areas exposed to the homogeneous electric field. The additional coefficient α has been added to the original equation by Adler [14] in order to account for field inhomogeneity as

$$E_{bd} = \alpha K A^{-n} \tau^{-1/3}, \quad (1.1)$$

where K and n are empirical parameters that depend on the liquid and polarity variations. It is believed that the Martin's formula works within several per cent of error margin in very wide range of conditions [12]. The empirical parameters (n) for the negative polarity are greater than for the positive polarity. This means that the negative streamers is more difficult to initiate due to the screening effect [7]. So far, most PSD systems have used the positive subsonic streamers because of their lower energy consumption in the discharge initiation process [15]. Consequently, relatively

little attention has been paid to the PSD using negative subsonic streamer mode. Nonetheless, the structural features such as their longer and thicker stalks indicate that their thermodynamic and electrical properties are largely differ from the positive ones. This means that the rapid spark formation as well as the subsequent hydrodynamic phenomena will strongly depend on these factors [16, 17], so the negative mode certainly deserves more attention.

1.1.2. Bubble Mechanism

The theory of streamer breakdown is mainly used to explain the electrical breakdown phenomena in gaseous media at the condition of high pressure (p) and large gap distance (d). With a sufficiently large pd value, the strong electric field can lead to a large charge amplification factor $\exp(\alpha d)$ by successive ionizations, where α is the electron impact ionization coefficient. In a single avalanche, the charge separation caused by the electrons placed at the head region and the ions left behind can lead to strong induced field to distort the external field. The localized electrons at avalanche head enhance the effective field, while the total field between the regions of separated charges will be reduced. If this induced field inside the avalanche becomes comparable to the external field, then the transformation of avalanche-to-streamer can take place. According to the Reather-Meek criterion [18], the condition can be given either by the total number of free electrons of $10^8 - 10^9$, or the charge amplification

parameter $ad \geq 18 - 20$. Unlike a gaseous medium, it is essential to form a lower density region in order to cause an avalanche-to-streamer transformation in liquid media. The most important factor which determines the mechanism of bubble formation is the leading edge characteristics of HV pulse [19]. In the microsecond timescale, Joule heating at the asperities on the electrode surface plays an essential role to form a gas pocket or vapor bubble [20]. The volumetric power density of Joule heating is determined by

$$Q_J = \sigma E^2, \quad (1.2)$$

where σ is the conductivity of water and E is the electric field intensity. With increasing field strength on the electrode surface, the current-voltage characteristic during the bubble formation varies within three different current limiting regimes: the Ohm's law, the field emission of the charge carriers from the electrode surface, and the space-charge limiting effect [21]. For most PSD systems having low electric field strength in the water gap, the Joule heating governed by Ohm's law is the dominant mechanism for the bubble formation. In this regime, a significant amount of time (up to several hundreds of microseconds) is required to produce a visible layer of vapor bubbles. Accordingly, some additional physical processes such as thermal conduction ($\sim 10 \mu\text{m}$) and bubble motion become relevant to the pre-breakdown process [22]. Schaper *et al.* also suggested that the hydrodynamic effect of water and vapor bubble should be taken into account, based on the coupled model of thermal and electrical effects for the slow vapor layer formation in the conductive liquid [23].

The distribution of preexisting micro-bubbles is another important factor promoting the breakdown initiation process. Korobeynikov carried out experiments using a heated electrode to produce bubbles with the radius of 15-50 μm prior to the application of HV pulse, and he reported that the breakdown was initiated from this pre-formed bubbles [24]. Korobeynikov *et al.* concluded that the breakdown of liquid can be possibly initiated from the preexisting micro-bubbles or air pockets on the surface of electrode, even in the absence of artificially produced macroscopic bubbles. In a similar context, various reactor configurations have been suggested to inject the gas bubble into the reactor from the application-oriented viewpoint. According to the extensive review of Bruggeman and Leys, it is possible to make numerous combinations of the electrode geometry, the method of gas injection (or production), the regime of plasma (i.e., glow, arc, corona), the type of power source (i.e., DC, AC, microwave, pulsed), and other factors [25]. An additional gas injection system tends to make the reactor configuration more complicated form, but gives the common advantage of operating the system with much lower electric field by allowing the breakdown to begin from the gas bubbles. Although most of the reviewed cases are devoted to the production of reactive species in liquid phase, there are some interesting cases that can be applied to the PSD system. In particular, recent reports on the electrical breakdown of water in the plate-to-plate electrode configuration assisted by additional bubbling methods present a strong cathode preference in the breakdown initiation [26, 27]. This preference has been observed only under weak electric field,

and it recovers to the ordinary preference of positive polarity under sufficiently high field strength. The lower initiation voltage observed in the bubble near the cathode is partly attributed to the electron emission from the cathode surface, but this alone does not adequately explain the preference transition with the electric field strength, and thus this topic needs further investigations.

1.1.3. Applications of Underwater Shock Wave Produced by PSD Technique

Underwater shock waves produced by PSD technique have been used in various applications, such as extra corporeal lithotripsy [28], rock fragmentation [29, 30], biofouling prevention [31], high-power ultrasound source [32], well cleaning [16, 33], and green algae treatment. Here, we briefly introduce last two subjects, i.e., well cleaning and green algae treatment, which have been mainly studied at Seoul National University.

Well cleaning

Most of domestic groundwater wells have a shallow depth and a small diameter, so that they usually have low well performance. Even worse, deteriorated wells hardly recover its performance due to lack of efficient well rehabilitation technique. Well clogging, one of the causes of degrading the well performance, gradually progresses

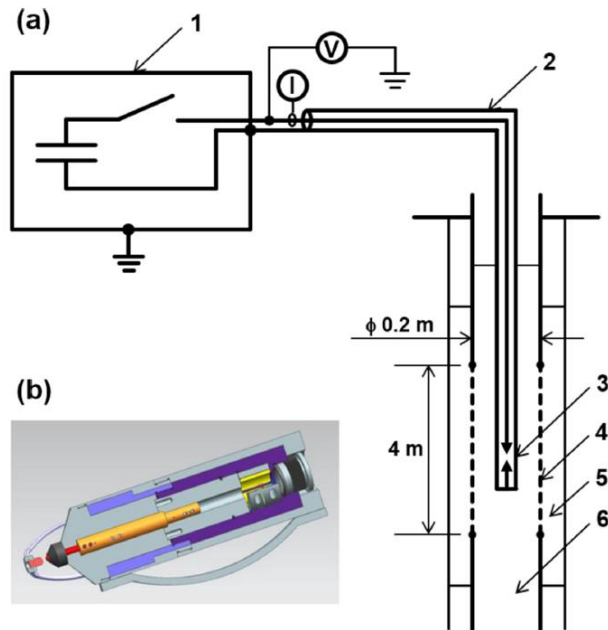


Figure 1.3. (a) Schematic diagram of experimental setup for the pilot-scale test: (1) pulsed power system, (2) coaxial cable, (3) spark generator, (4) well screen, (5) gravel pack, and (6) water. (b) Detailed cross-sectional view of the spark generator [16].

by mechanical and chemical processes that take place on the screen and its surroundings. In order to rebound the performance of deteriorated well, various rehabilitation methods have been suggested [34]. Mechanical ways of well cleaning, such as brushing, air surging and impulse treatments, are commonly aimed at removing incrustation from clogged parts.

Underwater PSD technique has been proposed to produce strong pressure waves for the cleaning of water wells [16, 33]. Compared to other impulse treatment

methods using explosives or pressurized fluid, the PSD technique appeals with its environment-friendly and cost-effective features. A typical configuration of PSD system for cleaning vertical wells can be depicted as Fig. 1.3. In this system, the spark plasma will be produced between a pair of electrodes installed at the end of spark generator, and the electrical energy required for entire discharge process can be supplied from the storage capacitors placed on the ground level. The electrical connection between the main power and the electrode assembly has been made using a coaxial cable in water, so the spark generator must be carefully designed to be waterproof.

The test well used for the pilot test reported by Chung *et al.* [16], which is

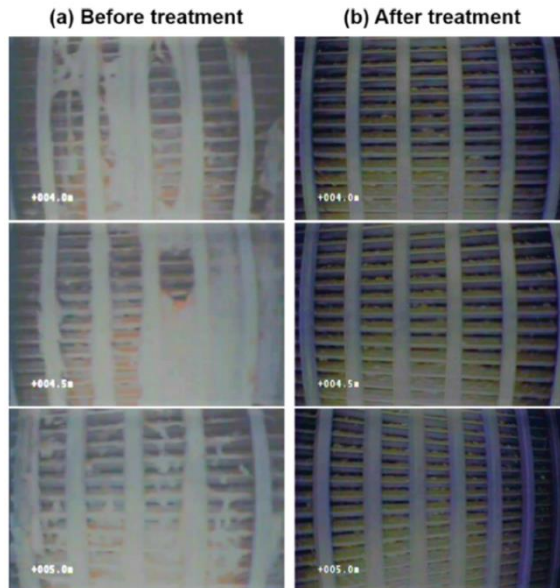


Figure 1.4. The camera images of well interior before and after the well cleaning are compared at three different well positions of 4.0, 4.5, and 5.0 m [16].

located near the Anseong-choen in Korea, has the well diameter and depth of 0.2 m and 20 m, respectively. The 4 m-long well screen was placed in the middle of the well, and most screen slots were originally clogged by biochemical process before the PSD treatment. After the pilot test with the operating parameters determined from the laboratory experiments, the effects of well cleaning with PSD technique are evaluated. As shown in Fig. 1.4., a visual inspection with an underwater camera clearly showed that most of the incrustations are successfully removed from the screen slots without any permanent damages on them. On the other hand, time-varying head ratios are measured from the slug tests performed before and after the well cleaning in order to quantify the enhancement of well performance. The characteristic decay time for head ratio reduced by the well cleaning indicate about 3 times enhancement of hydraulic conductivities, or well performance (Fig. 1.5). Clearly, the PSD treatment is a very

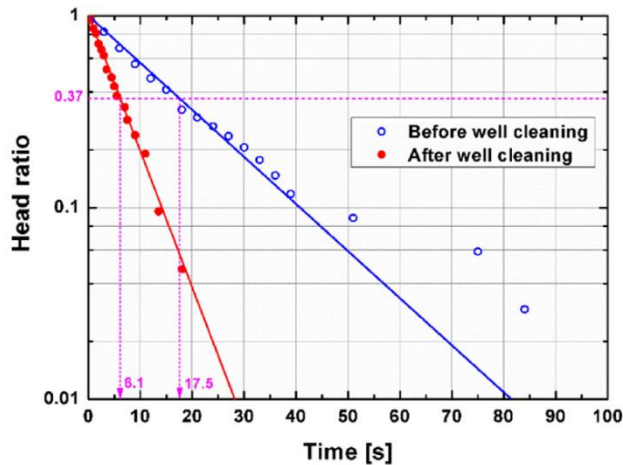


Figure 1.5. Plot of head ratio versus time obtained from the slug tests carried out before and after the well cleaning [16].

efficient way of rehabilitating the clogged well.

Various issues tend to arise when more extensive application of the present technique is pursued. One typical example is the PSD treatment on the horizontal wells. As depicted in Fig 1.6, the structure of horizontal well is quite different from that of a typical vertical well. A horizontal well tested in Ref [35] has a central collector well with the diameter and depth of 5 m and 45 m, respectively. Twelve $\phi 0.2$ m horizontal wells are distributed radially at about 25 m depth from the ground level. The horizontal length of well is 25 m, and the spark generator is inserted into the horizontal wells by a diver. In the PSD system for cleaning horizontal wells, a 110 m-long coaxial cable connecting the spark generator with the storage capacitor is the key element that mainly limits the pressure wave intensity. In other words, the pulse forming action which becomes pronounced at longer coaxial cables leads to the staircase-like current waveform variation, so the initial power transfer to the mechanical expansion of the spark channel is also strongly limited. Hence, the operating parameters optimized for the vertical wells cannot be retained to compensate the limiting effects emerging in horizontal wells. Although it is difficult to discuss whether the system is optimized to the environmental factors, the effects of PSD cleaning also can be clearly confirmed for the horizontal well. Similar to the test result on a vertical well, almost all incrustations are successfully removed by PSD cleaning (Fig 1.7). Besides, the result of step-drawn test showed that the well efficiency could be enhanced by 21.3% by PSD cleaning. More importantly, the head

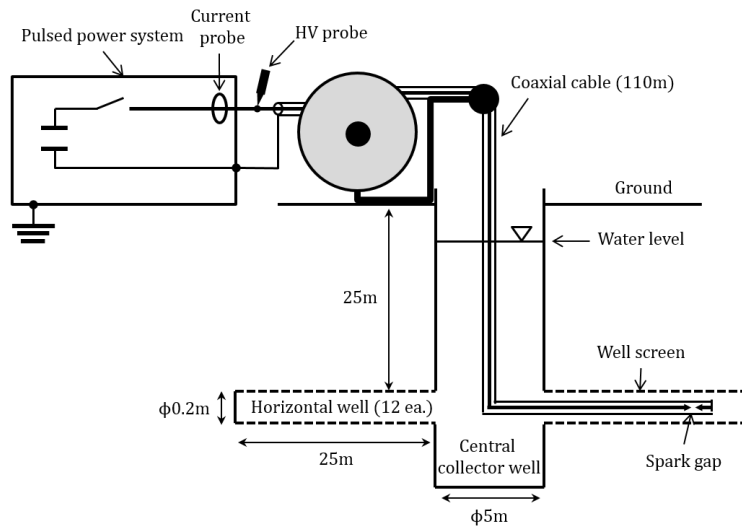


Figure 1.6. Schematic diagram of the horizontal well and PSD cleaning system [36].

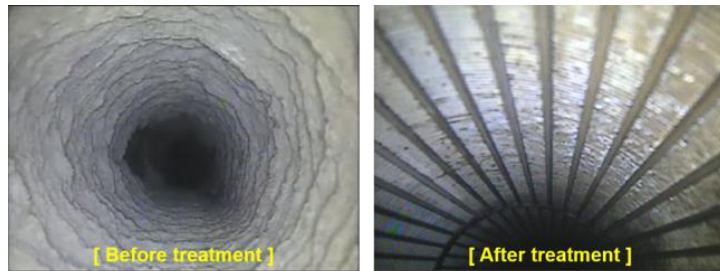


Figure 1.7. Comparison of camera images before and after the cleaning of horizontal well by underwater PSD [35].

loss at the well has been decreased by 80% whereas the head loss at aquifer layer is only reduced by 10%. This means that the well cleaning using PSD technique is truly useful for the rehabilitation of water well with minimized side effects on the aquifer layer [35].

Other critical issues associated with the pre-breakdown process are more complicated since they are usually related to various underlying physical processes. In fact, the energy initially stored in the main capacitor will be dissipated via RC decay during the pre-breakdown period, so this energy loss is the most prominent factor which determines the remaining voltage at the moment of breakdown. Sometimes, this energy loss becomes prohibitively large under harsher conditions where it is difficult to form a lower density region. In practice, the environmental factors such as high electrical conductivity of water, high flow-rate, and high hydrostatic pressure are usually belong to such conditions, and bring about high cost to cope with. Definitely, in order to apply the PSD technique to various types of water well existing in domestic or even in abroad, the issues tightly coupled with the pre-breakdown process should be understood more fundamentally.

Green algae treatment

PSD technique has recently been introduced for the treatment of green algae that cause variety of environmental problems floating on the river in summer season. This approach uses the shock waves produced by PSD to destroy the gas vesicles in the green algae and inhibit further growth. Installed on a sedimentation pond of the water purification plant, it aims to minimize the amount of chemicals used for precipitating the green algae in the plant by enhancing coagulation efficiency with the PSD treatment.

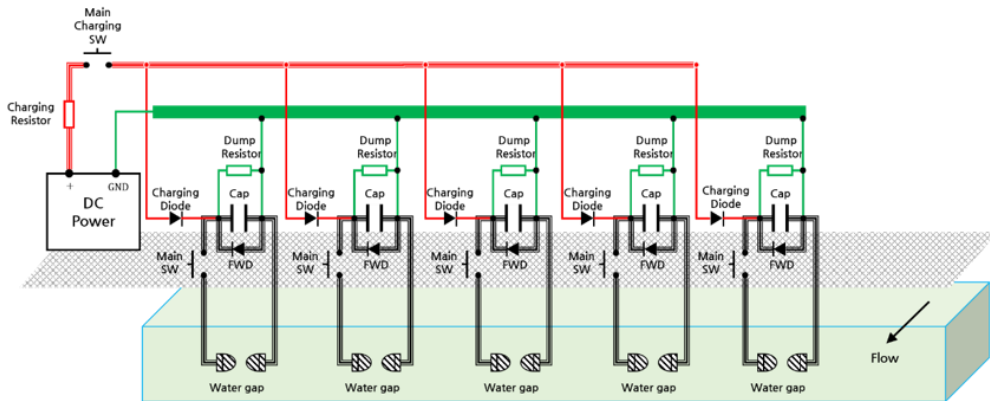


Figure 1.8. Schematic of a green algae treatment system installed on a sedimentation pond of the water purification plant.

The PSD system performs the primary function of directly destroying the gas vesicles in green algae at the first site of the water inflow into the purification plant. Although majority of green algae tend to be mixed with bulk water, spark generators are positioned at a shallow depth to treat the green algae floating on the surface which can be passed to the next station with the supernatant of sedimentation pond (Fig. 1.8). According to the preliminary experiments carried out in the laboratory (Fig. 1.9), it has been demonstrated that the shock wave produced by PSD smashed the gas pocket of green algae very effectively. Furthermore, it was confirmed that the amount of coagulant required for further treatment of green algae decreased almost by half for PSD processed samples. Also, the size of flocs was larger and the turbidity was lower for them. A plausible explanation for this effect is that the ζ -potential of green algae is lowered by interactions with shock waves. Hence, one can minimize the amount of

coagulant with the aid of PSD treatment on green algae.

In order to achieve certain level of treatment capability, the number of spark generators and repetition rate could be deduced based on the flow velocity at the site. Considering that the environmental factors are quite favorable to produce PSD, then the energy efficiency and robustness of entire system become the major issues in this application. In this context, efforts are being made to improve the processing volume of each spark generator or to enhance the energy efficiency by adding additional water gaps in series. However, these efforts should be based on thorough understanding of entire PSD process, especially of the pre-breakdown process which is responsible for the significant amount of energy loss. Also, influences of strong radiation emission and reactive species produced by plasma-water interactions on the mechanism of green algae treatment need to be examined more precisely.

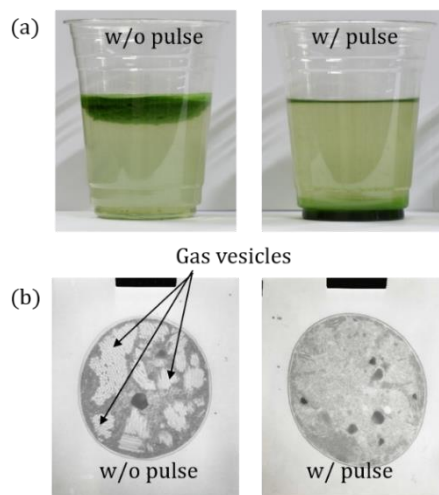


Figure 1.9. Comparison of (a) camera images and (b) TEM images for the specimens with and without PSD treatment.

1.2. Previous Work and Research Motivation

As described in Sec. 1.1, the underwater PSD technique has been used to generate the strong underwater shock wave for industrial applications. In many cases, rapidly expanding spark channel is a primary source of a shock wave where the surrounding water has a weakly compressible nature. Since the dynamic motion of spark channel is driven by the electrical power, the shock wave intensity can be understood as a result of close interplay between the pulsed power system and the plasma-liquid system. For the complete description of entire PSD process, basic researches on the underlying physics of the pre-breakdown and breakdown processes should be integrated. However, individual studies tend to be fragmented by each topic, and show quite different characteristics depending on the discharge conditions. For this reason, most studies have dealt with the pre-breakdown process and the breakdown process as a separate subject, and relatively much effort has been concentrated to the latter for rather practical purposes.

Many experimental studies have attempted to figure out the contributions of major experimental parameters such as main capacitance, remained energy (or voltage) at the breakdown time (W_{bd}), peak current, and gap distance or discharge shape, to the measured peak value of pressure wave at a fixed position. In the early works, Caufield found the linear relation between the peak pressure and the peak current [37], while Guman and Humprey suggested the different linear dependence of peak

pressure on the peak electrical power (\sim product of the voltage remained at the breakdown time and the peak current) [38]. In the following works of Touya [4] and Mackersie [39], the remaining energy in the capacitor bank at the time of breakdown (W_{bd}) was reported as the determining parameter of the peak pressure value, but their dependence were non-linear. However, later work of Timoshkin *et al.* insisted that operating with the high voltage is more beneficial than the large capacitance even for the same W_{bd} ($= \frac{1}{2}C_0V_{bd}^2$) values, and partly explained it using their phenomenological model [40]. More recently, similar trend has been observed by Lee *et al.*, and they revealed that only limited portion of energy deposited into the spark channel can contribute to the determination of peak pressure value, using the semi-empirical description with the Braginskii's shock approximation [41]. Meanwhile, practical efforts to establish an empirical formula for a given experimental condition by adjusting applied voltage and inter-electrode distance are still ongoing [17, 42, 43]. Most experimental works commonly recognize the practical importance of the electrical power transfer to the spark channel, especially in the early phase of breakdown. However, different parametric dependences found by individual works strongly indicate that the underlying physics of the shock formation process is too complicated to express in the simplified functional form of several operating parameters.

The numerical models describing the hydrodynamic effects of the PSD can be distinguished according to the spatial dimension of the governing equations. In the

approaches of zero-dimensional modeling, simple descriptions on the bubble growth and shock propagation have been made using various approximation methods, instead of directly solving the partial differential equations. In the earlier work of Ioffe [44], the electrical circuit equation is coupled to the energy balance equations of the cylindrical plasma channel. This model only calculated the transient feature of the spark channel under the assumption of ideal gas for the spark plasma. Cook *et al.* [45] developed a bubble growth model and the mass transport by considering the bubble wall in a semi-empirical way. The model presented by Lu *et al.* [46] described the dynamic motion of bubble using the well-known Kirkwood-Bethe model, and correction of the ionization potential and pressure caused by the charged particle interaction are additionally considered. In order to avoid solving the bubble equation, Kratel [47] and Lan [48] introduced the Rankine-Hugoniot relation, which couples a mass balance at the shock front with a modified Tait equation of state (EOS) for water. The resulting equation gave a simple relation between the bubble pressure and the expansion speed of bubble wall, and by solving this simplified equation with the energy and mass balance, the rate of thermal expansion was determined. Gidalevich *et al.* [49] took a slightly different technique called the arbitrary discontinuity propagation to derive the phase boundary velocity. In their later work [50], they derived an equation for the radial expansion of a cylindrical plasma column, in a similar form to the Rayleigh-Plesset equation, but there was no experimental validation. Meanwhile, as briefly described above, Timoshkin *et al.* [40] developed a

phenomenological model based on the Braginskii's equation for the energy balance on the spark plasma. This model could reasonably match the experimental results despite the model is based on the constant spark resistance for the entire discharge period. In most zero-dimensional models, the mass influx through the bubble wall by evaporation and condensation via thermal radiation and mass exchange is considered. Hence, these models are more suitable for describing the phenomena caused by large heat transport in a longer time scale, such as multiple shock generation by the bubble expansion and subsequent cavity collapse. However, all the zero-dimensional models assumed the uniform internal profiles of plasma temperature, density, and pressure at all times. This gives serious difficulty to initialize the spark channel properties which is expressed in a dimensionless form in their formulation [51].

Contrary to the zero-dimensional models, where various techniques were applied to simplify the governing equations, one-dimensional models directly solve a set of conservation equations as they are defined in the computational domain. Robinson [52] formulated a set of one-dimensional magneto-hydrodynamic (MHD) equations in cylindrical coordinates in Lagrangian form, for the exact tracing of the channel-water interface. However, in his experiments, the spark discharge was initiated from the thin metal wire, so the subsequent spark plasma has been treated as a hypothetical medium with a lot of arbitrary constants in its material properties. Sinkevich and Shevchenko [51] coupled a set of one-dimensional MHD equations to the electric circuit equation. However, their thermal and electrical conductivity

models adopted the analytic dependence of water in the liquid, vapor and super critical state obtained by semi-empirical way. In particular, the collision frequency in the calculation of the electrical conductivity value is determined by the electron-neutral and electron-ion collisions under the assumption of the same collision cross sections of electrons with hydrogen and oxygen atoms. More recently, Chung *et al.* [16] established a set of one-dimensional MHD equations coupled with the external circuit equation to solve them in a self-consistent manner. Their system of equations are closed by adopting the EOS and other thermophysical parameters calculated for the non-ideal water plasmas in LTE state [53]. It is worth noting that the self-consistent model of Chung *et al.* showed excellent agreement with the measured parameters from the experiments, and the parametric study has been carried out to deduce the optimized system components. The one-dimensional models are able to describe the detailed MHD behavior of the spark discharge plasma, but in return the computational cost became relatively high. Thus, one-dimensional model gives more accurate description on the dynamic evolutions of the spark channel and resulting shock wave for shorter time scale (< few tens of microseconds).

As a main reference of present work, Chung's self-consistent model deserves more detailed descriptions on its work flow with the constitutive models for water plasma and the external circuit. In their MHD solver, governing equations are formulated in Lagrangian form [16, 54], including the conservations of momentum, energy, and mass for the spark plasma. Additional equations for the magnetic field

and electric field construct a complete set of the single-fluid MHD equations. As shown in Fig. 1.10, the external circuit is simply modeled by a closed loop of the resistor, inductor, and capacitor (RLC) connected in series. Since the plasma channel is assumed to have a straight cylindrical shape, time-dependent values of lumped resistance and inductance are determined at each time-step from the radial distribution of electrical conductivity and the geometry of spark channel. In the respect that the electrical power deposition is the main driving source of the spark channel expansion, evaluating the radial profile of the electrical conductivity is one of the most important steps for the accurate systematic analysis. Figure 1.11 summarizes the flow of calculations for the self-consistent simulation of underwater PSD. It is noted that this model requires the initial parameters for the spark plasma such as the channel radius (r_0), mass density ratio (δ_0), and channel temperature (T_0). The initial plasma parameters are assumed to be uniformly distributed at the beginning, and the internal

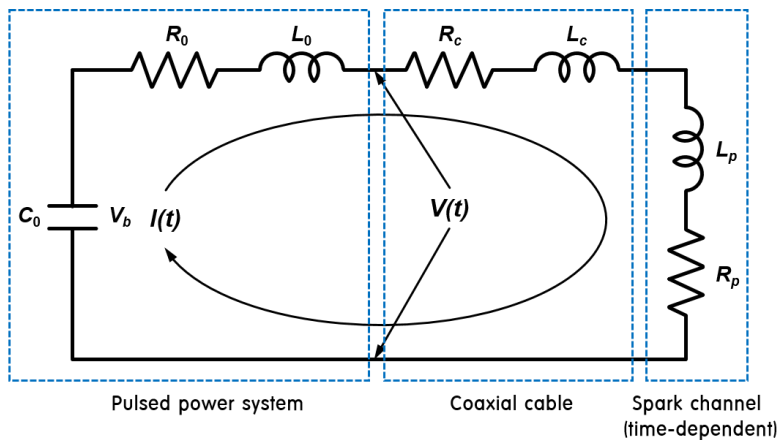


Figure 1.10. Schematic diagram of the equivalent circuit for the well cleaning system [16].

structure will be subsequently developed as a result of the complicated MHD action of spark channel surrounded by water. The time evolution of the radial shock wave profile presented in Fig. 1.12 addresses the only limited fraction of input energy contributes to the build-up of 1st shock wave. This means that the energy absorption of the spark channel during the very early phase of breakdown plays a dominant role in the determination of shock wave intensity. Hence, the Joule heating power during this early phase has been identified as the most important control parameter for generating strong shock wave, simply expressed as:

$$P_J = I^2 R_p \propto R_p \times \left(V_{bd}/L \right)^2, \quad (1.3)$$

where L is the system inductance, R_p is the initial plasma resistance, and V_{bd} is

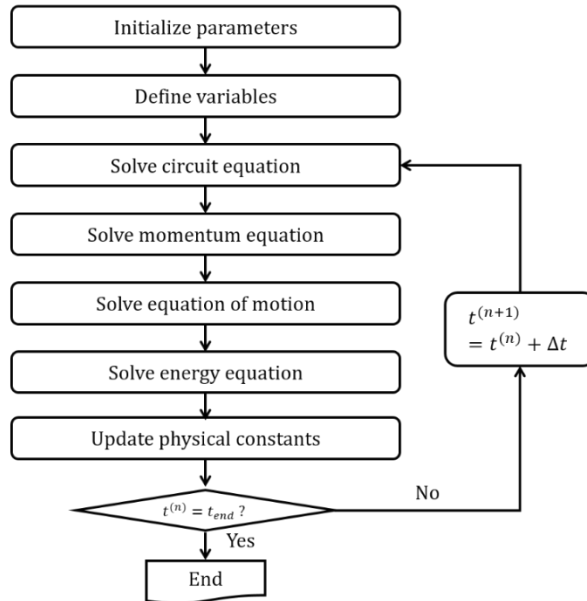


Figure 1.11. Flow of calculation for the self-consistent simulation of underwater PSD given in Ref. [16].

the remained voltage at the breakdown time. Similar description given by the semi-empirical analysis of Lee *et al.* [41] also advocates this feature.

This study is primarily motivated by Chung's description that proposing the importance of transient feature of the spark channel whose bulk resistance rapidly decreases in three orders of magnitudes within first few microseconds (from several hundreds of Ω to hundreds of $m\Omega$). During this short period, the spark plasma is almost instantaneously formed from the underwater streamers, and quickly transforms into the energetic arc plasma. This transition, called *streamer-to-arc transition*, has large temporal variations according to the power deposition into the spark channel, and thus it is closely related to the dynamic response of external circuit as well as the initial state of the spark plasma itself. Moreover, it can be reasonably assumed that the initial condition of the spark plasma depends on the characteristics of underwater streamers emerging in the pre-breakdown period.

In the present work, a novel experimental method is proposed to characterize the subsonic streamers and to observe their rapid transition to the arc state. In particular, the PSD has been generated by using negative subsonic discharge mode. Comparing with the conventional positive subsonic mode, the negative subsonic mode has a tree-like structure without large bubble clusters around its stalk and has a faster propagation speed, so that a more efficient shock formation could be expected when it causes the breakdown. The practical limitation of the negative discharge mode, the slow bubble formation process due to the screening effect [7], has been compensated

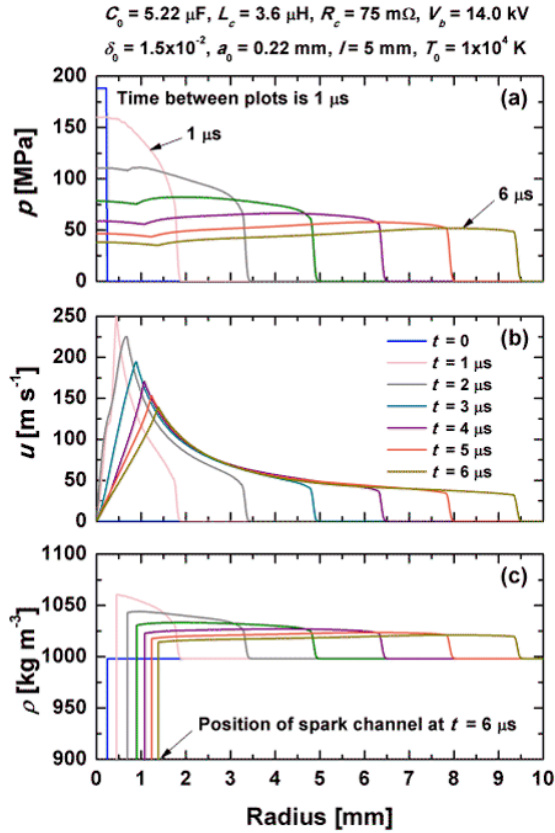


Figure 1.12. Spatial distribution of (a) pressure, (b) velocity, and (c) mass density at each time during the expansion of the spark channel calculated for the charging voltage of 14 kV [16].

by preconditioning a gap with water electrolysis. In the presence of initial hydrogen bubbles produced at the cathode surface, the overall pre-breakdown period could be remarkably reduced, and the uncertainty originated from stochastic nature of bubble formation has been minimized. The time-varying characteristics of negative subsonic

streamers are measured with time-resolved diagnostic techniques: shadowgraphy and optical emission spectroscopy. Considering that little efforts had been paid to characterize the plasma properties of subsonic streamers so far, these measurements provide not only the fundamental understanding on the time-varying characteristics of subsonic streamers but also the valuable information for initial parameters of the spark plasma. For the comprehensive understanding that relates the characteristics of negative subsonic streamers to the shock wave formation, the rate of streamer-to-arc transition has been decelerated by using a longer coaxial cable that efficiently limits the input power. Time-resolved shadowgraph images of the expanding spark channel and propagating shock front were also successfully obtained by refining the optical arrangement.

Regarding the several interesting features observed in the pre-breakdown period and streamer-to-arc transition phase, further improvements of Chung's model are strongly motivated. In the case of spark discharges at longer coaxial cable, the pulse shaping effect of the transmission line becomes pronounced, especially in the early phase of spark expansion. However, the circuit response simulated by the simple series-RLC circuit model that used in the previous model was not able to describe this complicated pulse forming action. In order to simulate the electrical power transmission through the coaxial cable in an efficient way, the cable is treated as the series connections of small segment which contains the resistor, inductor, and capacitor assembled in the shape of capital letter *T*. Since this model of T-sectioned

transmission line is capable of considering the energy storage of the cable itself, the electrical interplay between the spark plasma and the pulsed power system could be more reasonably described, particularly for the streamer-to-arc transition period. Another modification has been made on the load side of the circuit solver. Previous model assumed that all the discharge current flows through the spark channel, but this assumption is valid only if the water gap resistance is relatively large due to the low conductivity water or electrode structure. Thus, the current balancing between the spark channel and the rest of water gap has been taken into account to describe more realistic Joule heating rate. Therefore, the integrated analysis combining the improved self-consistent model with the experimentally obtained initial parameters has been carried out to describe the detailed shock wave formation process during the streamer-to-arc transition. All the improvements of simulation model motivated by Chung's work can be summarized as Table 1.2.

Table 1.2. Comparison of present model with previous work.

	<i>Previous model</i>	<i>Present model</i>
<i>Cable</i>	Lumped parameter model (R-L in series)	T-sectioned model
<i>Initial plasma properties</i>	Adopted from other literatures & assumed uniform	Measured from experiments & assumed non-uniform
<i>Current leakage in water gap</i>	Neglected	Considered

1.3. Author's Contribution and Scope of Study

At first glance, generating shock wave using the underwater PSD seems simple and easy to apply due to the relatively simple configuration. However, this impression is deceptive because serious difficulties will arise when trying to improve the performance of system or the applicable range. In particular, most of the serious issues are closely related to the pre-breakdown process, so it is difficult to figure out the actual problems by taking conventional approach that considers only the expansion motion of spark channel (or bubble) during the breakdown period. In addition, although the energy dissipated during the pre-breakdown period is the most prominent factor, the initial state of spark plasma produced by the subsonic streamer is also play an important role in the shock wave formation. In this respect, the experimental method newly introduced in this study can provide an alternative approach. Although the diagnostics on the subsonic streamers are mostly depending on the optical techniques such as the shadowgraphy and optical emission spectroscopy, their time-transient features could be characterized within each discharge event. Such time-resolved data can contribute to the more reasonable assumption on the initial plasma parameters for the spark channel as well as to the understanding on the propagation mechanism of subsonic streamers. Moreover, close observation on the streamer-to-arc transition, whose rate is decelerated by using a long transmission line, has been made by visualizing the structures of spark plasma and shock waves. In order to describe

the newly observed features such as the pulse forming action of transmission line and the spatially non-uniform initial plasma parameters using the simulation model, Chung's self-consistent model has been modified. The improved model could delicately simulate the process of shock wave formation influenced by the radial profile of the initial spark plasma parameters.

It should be noted that the PSD has been produced with negative subsonic streamers in the present work. The biggest drawback of negative subsonic mode, the slow initiation due to screening effect [7], could be overcome by preconditioning the reactor with water electrolysis. The hydrogen bubbles produced at the cathode surface remarkably reduced the time duration for the streamer initiation (up to ~90%), a significant amount energy could be saved during the overall pre-breakdown period consequently. In the experimental setup, only a pulse modulator (~400 V, ~300 ms) for the over-voltage water electrolysis is simply added to the existing device, so it is necessary to pay more attention to the practical advantages of this newly proposed experimental technique.

Experimental and numerical studies for the underwater PSD at longer coaxial cable are also meaningful in the application oriented view point. When the PSD needs to be produced at a remote site far from the pulsed power system (e.g., cleaning horizontal well), one can easily decide to extend the coaxial cable. However, as cable length increases, pulse forming action begins to take a dominant role in the early phase of breakdown. Hence, the improved simulation model can be utilized to predict more

realistic shock wave intensity for such cases. In addition, specific operating parameters can be optimized according to the expected shock wave intensity for a given environmental condition. Although more experimental studies are recommended to precisely define the initial plasma parameters under a wide range of environmental conditions, the integrated analysis using experimental and numerical methods proposed by present work will still be applicable.

In summary, there are two addressing points in present work. One is the experimental methodology proposed to elucidate the time-varying characteristics of the negative subsonic streamers and their rapid transition into the arc plasma state as the breakdown occurs. The other is the delicate numerical simulations on the shock wave formation in the case where the rate of streamer-to-arc transition is controlled by the length of transmission line. In this study, efforts of plasma diagnostics are concentrated on the pre-breakdown period while the hydrodynamic features of PSD during the breakdown period are interpreted using the simulation model because of the extreme difficulties in diagnostics on spark and arc plasmas.

This dissertation consists of six chapters. After describing the details of experimental methods and their principles in Chap. 2, experimental results and related discussions for time-varying characteristics of the negative subsonic streamers will be given in Chap. 3. Improvements of the self-consistent simulation model are presented in Chap. 4. Chapter 5 is devoted to the analysis on the streamer-to-arc transition process. Here, numerical and experimental results related to the shock wave formation

are mainly discussed. Concluding remarks on the present work and recommendations on future research topics are placed in Chap. 6.

Chapter 2. Experimental Setup and Diagnostics

In this chapter, overall experimental setup including the power system, discharge chamber, electrode assembly, and diagnostic devices is described. Some details on the designing procedure and working principle of the optical diagnostic methods such as shadowgraph imaging and optical emission spectroscopy are also presented.

2.1. Capacitive Discharge System

Figure 2.1 presents a schematic diagram for underwater PSD system at Seoul National University (SNU). In order to provide a main high-voltage pulse for both the pre-breakdown and the breakdown processes, a conventional capacitive discharge system has been utilized. A high-voltage (HV) capacitor (CSI capacitor, 35W619) is charged by a direct-current (DC) power supply (Converttech, SHV300R). Here, five of avalanche rectifier diodes (ABB, 5SSDA-06D5007) stacked in series to provide the free-wheeling path for the discharge current during the underdamping oscillation. A triggered spark-gap (Excellitas, GP-12B) is placed at a high-side of power system to transfer the HV pulse to the coaxial cable, and this cable is connected to the electrodes pair placed in the discharge chamber. The discharge chamber is filled either with tap water or sodium-chloride (NaCl) solution. The electrical conductivity of water is

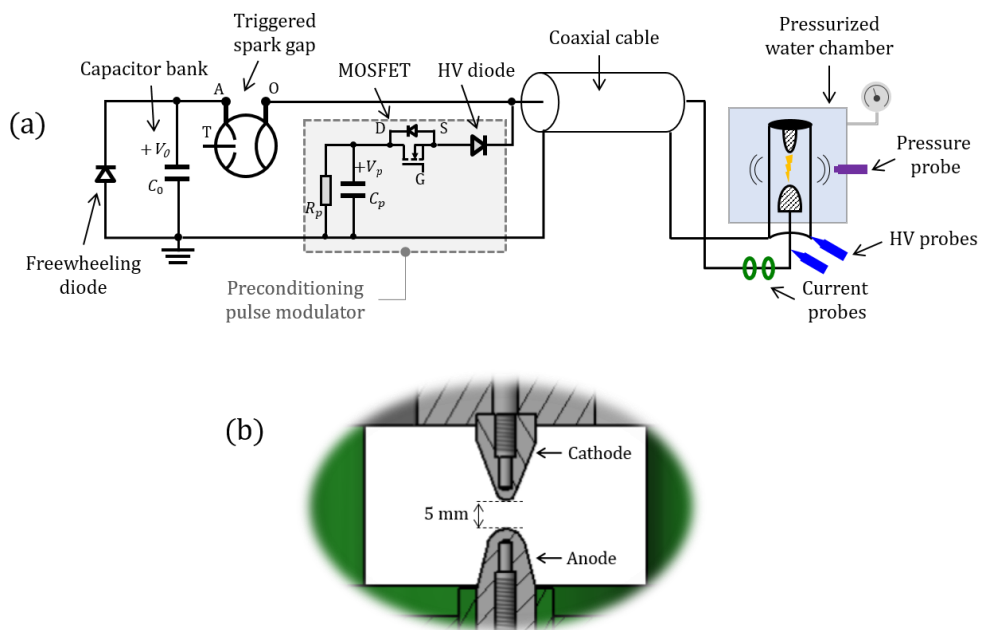


Figure 2.1. (a) A schematic diagram of the pulsed-spark discharge system and (b) a drawing of the electrode assembly.

adjusted within $250\text{-}750 \mu\text{S cm}^{-1}$ range, similar to that of ground water or tap water.

The discharge chamber can be pressurized up to 3 atm (in absolute pressure) by an external air compressor. The electrode assembly having a coaxial structure allows the current released to the spark plasma on its center to come back through the four return-posts at the asperity. In order to operate the PSD in negative subsonic mode, the electric field inside the water gap is negatively enhanced using the tip radii of 1.5 mm for a cathode and 3 mm for an anode. The inter-electrode distance is fixed to 5 mm, so the resulting field enhancement factor in the cathode tip vicinity (g_-) is approximately 2.3. The electrode tips are made from a copper-tungsten alloy (Cu20%-

W80%) and replaced every 20 discharges to manage the uncertainty due to erosion.

As marked with gray box in Fig. 2.1(a), a preconditioning pulse modulator is simply added to the existing capacitive discharge system. This pre-conditioning pulse modulator consists of a low-voltage (LV) electrolytic capacitor (< 600 V, 6.8 mF) and an N-channel enhancement-mode MOSFET (metal-oxide semiconductor field-effect-transistor). A HV diode (EDI, KHP35) is placed in front of the MOSFET (IXYS, IXTL 2N450) to protect the modulator from the main HV pulse. At the same time, the forward over-voltage failure can be prevented by the free-wheeling diode (FWD) during the underdamping response. The LV capacitor is charged by DC power supply (KSC, 400 V - 1 A), and the square pulse can be modulated by switching the MOSFET. This pre-conditioning pulse will be transferred to the water gap prior to the main HV pulse, so the hydrogen bubbles produced at the cathode surface can remarkably reduce the initiation delay of the underwater streamers. Since the preconditioning pulse does not require an additional current path other than the coaxial cable, this technique is easy to implement and cost-effective compared with other gas injection methods.

In the experiments, triggering delays for the main HV and preconditioning pulses are controlled by a delayed pulse generator (Berkeley Nucleonics, 577). Within the range of water conductivity used in our experiments ($250 - 750 \mu\text{S cm}^{-1}$), the typical duration of preconditioning pulse is set within $200 - 400$ ms when the water electrolysis is induced at over-voltage (~ 400 V) condition. Because the gate driving

circuit of MOSFET is optically isolated, the triggering signal generated from the pulse generator (+5 V TTL) can be directly fed to the optical transmitter for the preconditioning treatment. In order to avoid the cross-conduction failure, the TSG switch will be triggered after a time delay (fixed to 5 ms in this study) from the cease of preconditioning pulse. For the high-side operation of TSG switch, a driving circuit of trigger transformer (Excellitas, TR-1700) is designed as shown in Fig. 2.2. In this circuit, the output trigger pulse is induced at the secondary side of transformer when a primary-side capacitor (47 μF) is discharged. At charged voltage of 400 V, the induced voltage exceeds the threshold value for switching TSG (~ 15 kV) within ~ 3 μs . Thus, there is a triggering delay between the gate signal for switching primary-side IGBT (Insulated gate bipolar transistor) and the emergence of HV pulse at the opposite electrode which is denoted by O in Fig 2.2. This triggering delay tends to slightly vary with the charging voltage of main storage capacitor. In this respect, all

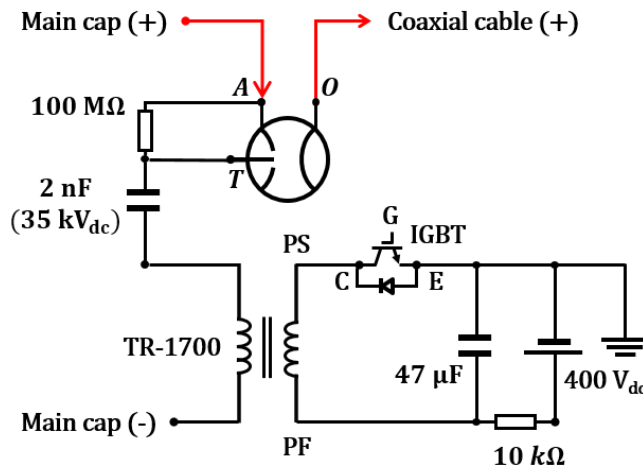


Figure 2.2. Circuit diagram of the triggered spark gap switch for high-side operation.

the delays of control signal for the switching and measurement devices are adjusted with respect to the gate signal of the primary-side IGBT. It is noted that all the coaxial cables used to transfer triggering signals to the switching devices have the same length, so the signal propagation delays are identical.

2.2. Electrical Measurements

Figure 2.1 also depicts the electrical measurement devices installed to the PSD system. The HV probes (North-star, PVM-4) measure the time-varying voltage at cathode and anode, respectively. Since the discharge current increases by two orders of magnitude at the onset of breakdown, the current waveforms for pre-breakdown and breakdown periods are separately measured. For measuring pre-breakdown current, a current transformers (Pearson, 4997) is coupled with a TVS (transient voltage suppressor) diode (Vishay, 1.5KE13A) for the circuit protection from over-voltage induced by large arc current during the breakdown period. In the case of breakdown current, a 10X attenuator (Pearson, A10) is added to the current transformer (Pearson, 4997) to adjust the output signal to an acceptable level. The current and voltage waveforms have been monitored at the output side of the coaxial cable, so the time-varying load (i.e., the spark plasma) resistance could be determined more precisely. The pressure wave produced by PSD at the center of discharge chamber has been measured by the piezoelectric sensor (PCB Piezotronics, 113B23).

This pressure probe is mounted on the side wall of chamber, which is located 10 cm away from the water gap. All analog signals are digitized by a multi-channel digital oscilloscope (Tektronix, MSO58: 5-BW-2000). Using coaxial cables with the same length, signals acquired at each channel have the identical propagation delay.

2.3. Shadowgraph Imaging

2.3.1. Principles

The shadowgraphy technique is one of the most popular visualization methods for observing physical phenomena of underwater discharges. For applying to underwater PSD, optical elements are aligned along the main observation port of the discharge chamber as illustrated in Fig. 2.3. Basic working principle of the shadowgraph technique is very simple. In the Cartesian coordinate system, when the z-axis is represented by the propagation direction of the light rays, the x and y pairs form a plane perpendicular to the z-axis. The components of angular ray deflection caused by an imaging object, so called schlieren object, can be expressed as:

$$\varepsilon_x = \frac{1}{n} \int \frac{\partial n}{\partial x} \partial z, \quad \varepsilon_y = \frac{1}{n} \int \frac{\partial n}{\partial y} \partial z, \quad (2.1)$$

where n is the refractive index of water [55]. By definition, a shadowgram appears as the form of light deficit in a detector plane. Clearly, the differential illuminance in

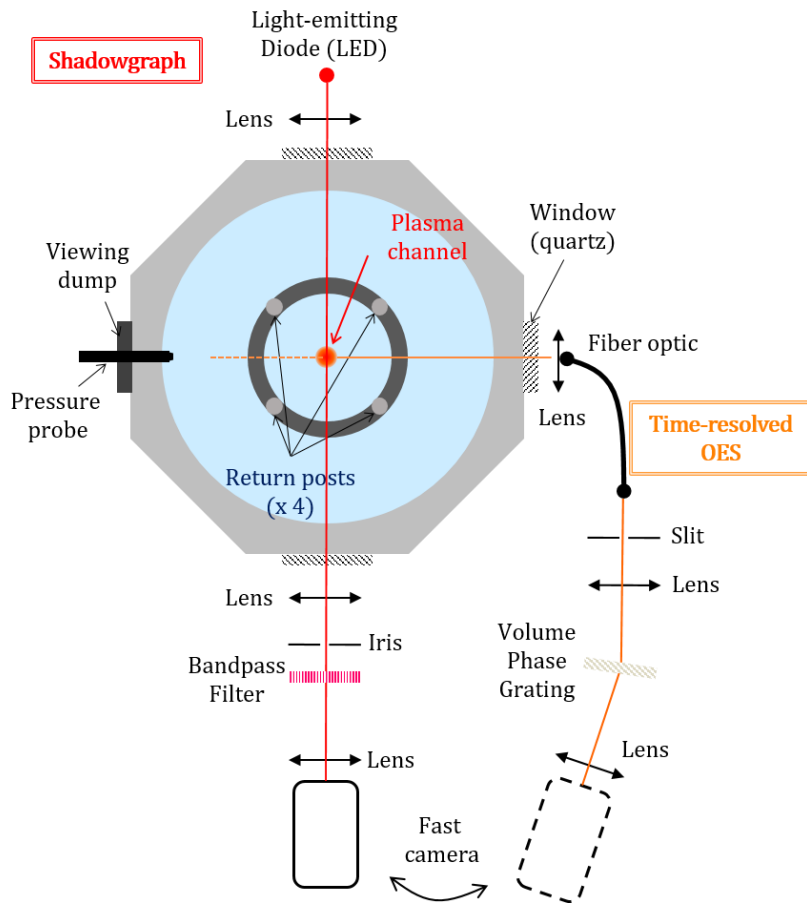


Figure 2.3. Plan view of schematic for the layout of the optical diagnostic system.

the shadowgram occurs only when there is a gradient of deflection angle ($\nabla\epsilon$). Hence, the illuminance of shadowgram becomes proportional to the Laplacian of refractive index ($\nabla^2 n$) in accordance with Eq. (2.1).

Although the extreme ease is the most obvious benefit of the shadowgraphy technique, we still encounter the technical difficulties due to small spatial dimension and strong self-emission of an imaging object. In this respect, a lens-based, focused

shadowgraphy configuration has been employed to our experiment. As shown in Fig. 2.3, the backlight is collimated by the first lens and the parallel beam passing through the schlieren object is focused by the second lens. In the end, the final shadowgram is obtained by using a fast-frame camera equipped with the third lens (focusing lens). The focused shadowgraphy can be distinguished from the basic parallel-light shadowgraphy by the presence of the additional optical elements that are interposed between the schlieren object and the shadowgram. When the fast-frame camera operates at high frame-rate, only a limited number of detector pixels can be activated, so the ability of de-magnifying the shadowgram to a small size is a great advantage of the focused shadowgraphy. Also, with a proper combination of second and third lenses, the sensitivity and magnification of shadowgram can be successfully decoupled. Here, we note that the iris is placed between the second lens and the optical band-pass filter to cut off the strong self-emission from spark plasma [56], because the strong emission will easily saturate the detector sensor particularly during the breakdown period. Strictly speaking, the layout of focused shadowgraph system with an additional cut off is identically the same with the “bright-field” schlieren optics [55]. It is noting that the iris is tighten only when trying to visualize the spark plasma appearing in the breakdown period, the Schlieren image may appear instead of the shadowgram since the circular cut off becomes operative in such condition. Hence, the iris requires subtle adjustments for the optimized imaging performance.

2.3.2. Optical Arrangement

There are two primary goals of the shadowgraph imaging in this study. One is the visualization of the underwater streamers appearing in the pre-breakdown period. The other is observing the evolution of the spark channel during the breakdown phase. In order to attain these goals with only minor modifications on the optical arrangement, the focused shadowgraphy system has been realized as shown in the Fig. 2.4(a). As a

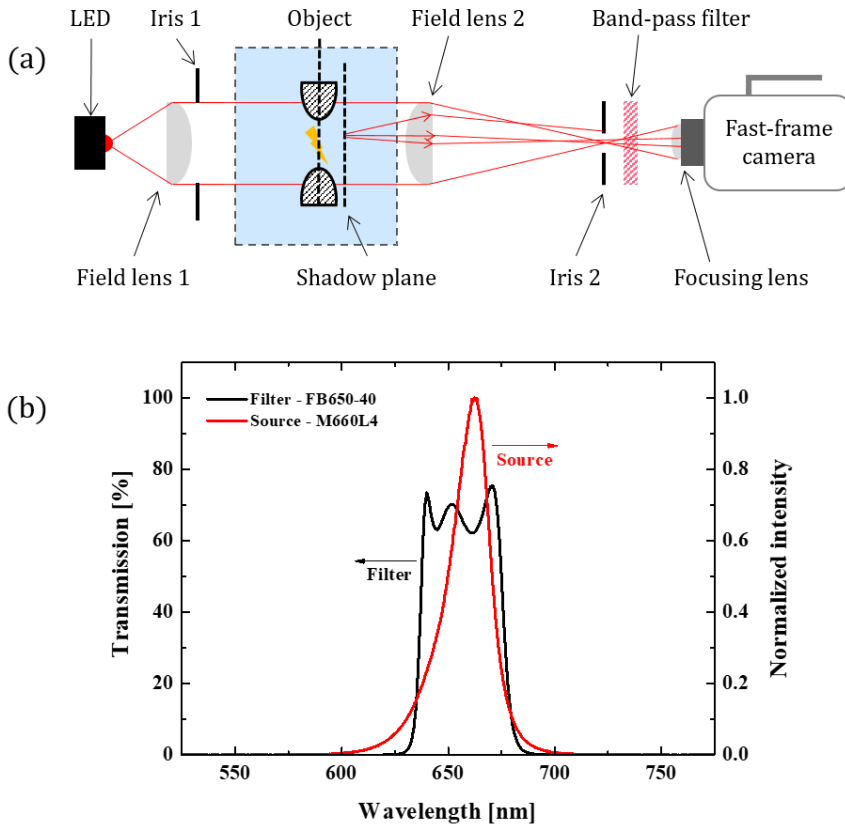


Figure 2.4. (a) Side view of schematic for the focused shadowgraphy and (b) emission, transmission curves of the light-emitting diode and the band-pass filter [57].

backlight source, a light emitting diode (LED; Thorlabs, M660L4) is utilized. The backlight is collimated by a plano-convex lens (Thorlabs, 60 mm), and its aperture is adjusted by the first iris (i.e., iris 1 in the figure). A 300 mm achromatic lens (Nikon, f/4) focuses the backlight deflected by the Schlieren object onto its focal plane where the second iris will be positioned. A 105 mm macro lens (Nikon, f/2.8) is mounted on the fast-frame camera (Vision Research Inc., Phantom V711) to obtain the final shadowgraph images. Here, an optical band-pass filter (Thorlabs, FB650-40) coupled with the LED has been inserted between the second iris and the focusing lens. Since the pass-band of this optical filter ($\lambda_c = 650 \text{ nm}$, $\Delta_{FWHM} \cong 40 \text{ nm}$) covers the hydrogen Balmer-alpha line (H_α , 656.28 nm), the image of H_α emission can be superimposed to the shadowgram that is produced by the hydrodynamic features of the discharge. In principle, the shadow plane must be located at a finite distance from the imaging object. In practice, however, our imaging system focuses directly on the water gap, rather than the shadow plane. Nonetheless, we still obtain the shadowgraph images because of the depth-of-focus (DOF) of the imaging system and the finite dimension of the imaging object (i.e., underwater streamer or spark channel) [56]. The image magnification can be simply adjusted by replacing the focusing lens to different one (Nikon, 24-120 mm, f/4) for the wide field-of-view (FOV) to visualize the evolution of the spark channel and resulting shock wave. It is noted that the maximum pixel resolution decreases at higher frame-rate: 128 x 64 pixels at 390,804 fps and 128 x 8 pixels at 1,511,111 fps, respectively. The minimum exposure time is 0.29 μs

irrespective to the frame-rate. The post processes and the analysis of recorded images have been carried out using MATLAB®. An example of a processed shadowgram is shown in Fig. 2.5. For displaying with the other experimental data, time mark on the shadowgraph images will be synchronized with the electrical measurement data, in the following parts of this paper.

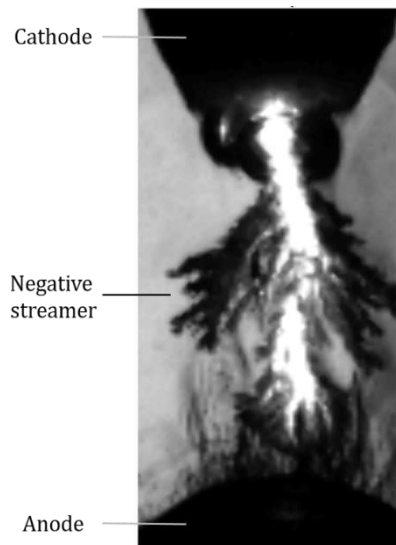


Figure 2.5. An example of a processed shadowgraph image.

2.4. Optical Emission Spectroscopy (OES)

Owing to the presence of surrounding water, it is impossible to directly access to the underwater plasmas on diagnostic purpose. From this reason, optical emission spectroscopy (OES) has been widely used to diagnose the plasmas in liquid based on its non-intrusive nature. In this section, we focus on the time-resolved measurement

of the electron density from the Stark-broadened profile of hydrogen Balmer-alpha (H_α) line, including the design and development of the high-speed spectrograph.

2.4.1. Methods of Electron Density Measurement

For investigating the plasmas in liquid, OES technique has been often regarded as an ideal method to characterize the physical phenomena associated with the discharge. Although there are no other alternative means, OES still provides valuable information for the electron density, rotational and vibrational temperatures, and content of reactive chemical species [58]. Of the various plasma parameters, the electron density (n_e) can be presumed as the most important one especially in the transition process to the spark plasma from the underwater streamer. This is because of the huge contribution of n_e in the determination of electrical conductivity within such plasma regime [59, 60].

There are several methods to determine the electron density based on the analysis of spectral line profile. In these diagnostic methods, the broadening or shift of the spectral lines are measured, in the presence of several broadening mechanisms such as the natural broadening, the pressure broadening, the Doppler broadening, and the Stark broadening. Among them, the Stark broadening is caused by the emitter - perturber collision where the micro-field produced by colliding perturber ions alters the atomic levels of emitters. This broadening mechanism deserves a special attention

since it overwhelms the rest of the broadening mechanisms in the high density condition [61]. Moreover, the hydrogen atom is noticeably sensitive to the Stark effect, so it is straight-forward to use the profile of the Balmer lines for determining n_e of the hydrogen abundant plasmas.

The spectral line to analyze must be carefully chosen on the basis of the emission characteristics of plasma. The Balmer-beta line (H_β) is believed to be the most accurate one in the wide range of electron density because of the immunity of its line shape to the ion dynamics effects or to the electron temperature [62, 63]. This is particularly true for low density plasmas of which requires a high precision measurement. However, its relatively low intensity compared to the Balmer-alpha (H_α) line causes an additional cost to collect the sufficient level of signal. Besides, there is a possibility of H_β line disappearing by nonideal effects. To explain such phenomenon, here we introduce the non-ideality parameter (Γ) that is expressed as

$$\Gamma = \frac{Z^2 e^2}{4\pi\epsilon_0 a k_B T} , \quad (2.2)$$

where Z is the ion charge number, and a is the average inter-particle distance. In the weakly non-ideal plasma whose coupling parameter is less than unity ($\Gamma \leq 1$), the ionization energy of principal quantum number i will be shifted by

$$\Delta U_i = \frac{Z^2 e^2}{4\pi\epsilon_0 \lambda_D} , \quad (2.3)$$

where λ_D is the Debye length of plasma [64]. Combining with this ionization potential lowering, the Stark effect becomes more pronounced due to the micro-field

enhanced by shorter inter-particle distance. Hence, the upper bound states of the hydrogen get closer to each other, and may overlap provided that those levels are sufficiently broadened. In this respect, Descoeudres *et al.* roughly estimated using the Inglis –Teller relation that the H_β line can be indistinguishable from the continuum when $n_e \geq 6 \times 10^{18} \text{ cm}^{-3}$, in the electrical discharge machining (EDM) plasmas [65]. That is, in such high density regime, only H_α line can be observed while there are neither H_β nor H_γ lines.

Meanwhile, determining n_e from the shape of H_α line must consider the ion dynamics because the line profile is very sensitive to the perturber's reduced mass (μ) and the degree of thermal equilibrium ($\theta = T_i/T_e$). Hence, ion dynamic effects are taken into account in the pioneering work of Gigosos *et al.* to obtain the full profiles of the Stark broadened hydrogen Balmer lines in the simulations [66]. They also derived simplified fitting equations from numerous simulation results performed with various combinations of input parameters (μ, T). Here, it is worth noting that they have recommended to use full width at half area (FWHA) as an alternative experimental parameter instead of conventional full width at half maximum (FWHM), to directly evaluate the n_e value. This description can be simply demonstrated by the Fig 2.6. In the figure, the strong dependence of FWHM on μ and T appears as the unclear relationship with the electron density, whereas FWHA shows much narrow dispersion. From this respect, Cardenoso *et al.* presented a useful formula for the evaluation of n_e [66] :

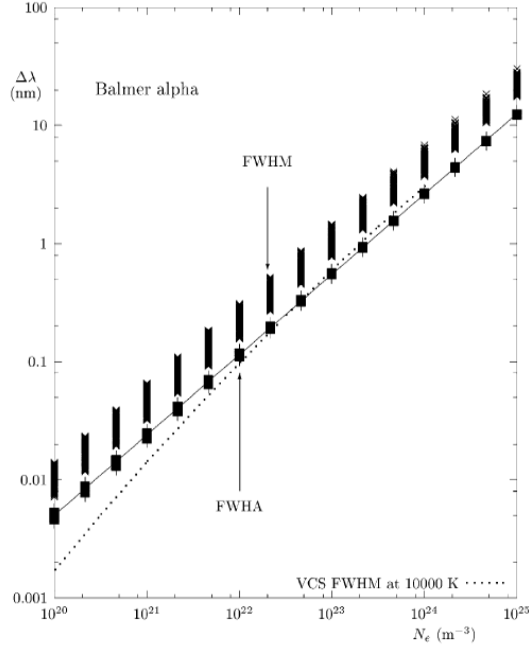


Figure 2.6. Dependence of the H_α FWHM and of the FWHA with the every combinations of T and μ considered in the simulations [66].

$$n_e = 10^{23} \text{ m}^{-3} \times (FWHA [\text{nm}]/0.549)^{1.4714}, \quad (2.4)$$

where $FWHA$ can be defined as

$$FWHA \equiv \Delta\omega_2 - \Delta\omega_1;$$

$$\Delta\omega_1: \frac{1}{4} = \frac{\int_{-\infty}^{\Delta\omega_1} I(\omega) d(\Delta\omega)}{\int_{-\infty}^{+\infty} I(\omega) d(\Delta\omega)}, \quad \Delta\omega_2: \frac{3}{4} = \frac{\int_{-\infty}^{\Delta\omega_2} I(\omega) d(\Delta\omega)}{\int_{-\infty}^{+\infty} I(\omega) d(\Delta\omega)}. \quad (2.5)$$

Hence, $FWHA$ has been treated as a main experimental parameter in the OES of present work. Also, an additional relation of $FWHM$ and n_e :

$$n_e = 8.8308 \times 10^{22} \text{ m}^{-3} \times (FWHM [\text{nm}])^{1.6005} \quad (2.6)$$

has been used to estimate the influence of the ion dynamic effects. Note that this

expression is deduced by fitting the other simulation results of Gigoso *et al.* [67] at a plasma temperature of 10^4 K with $\mu = 1$.

2.4.2. Design of Spectrograph for Time-resolved OES

A complete set of OES system consisting of collecting optics, diffraction optics, and a detector can be thoroughly constructed for the unique objective of each experiment. In the case of underwater PSD, as the time-resolved OES is attempted within a single discharge due to the significantly large shot-to-shot variation, the additional cost for the spectrograph rapidly increases with the required temporal resolution. In fact, when it comes to single-point measurement, a streak camera is an ideal choice as a detector for both the high temporal and spectral resolutions. Nevertheless, since it is too expensive to adopt such spectrograph system in our experiment, a new spectrograph system has been developed that is using the fast-frame camera as a detector.

As already shown in Fig 2.3, the spectrograph is designed in an unfolded layout by replacing the reflective elements of conventional Czerny-Turner configuration such as concave mirrors and a reflection grating with achromatic lenses and a volume phase holographic grating (VPHG). This type of spectrograph, called VPHG spectrograph, has clear advantage in terms of the high diffraction efficiency in visible range and can be assembled very easily with commercial optical elements in the laboratory. In designing the entire set of VPHG spectrograph, the physical

dimension of CMOS (complementary metal-oxide-semiconductor) sensor of the fast-frame camera (Vision Research Inc., Phantom V711), which is also used for the shadowgraphy, became the biggest limiting factor. Considering that only 128×8 pixels ($w_{pixel} = 20 \mu\text{m}$) can be activated when the frame-rate is higher than 10^6 fps, the magnification of spectrum image must be optimized.

In order to specify the performance requirements of the VPHG spectrograph, preliminary experiments were carried out. The underwater PSD was produced in the tap water for the spectral survey using the wide-range VPHG spectrograph, and an example of the emission spectra can be shown as Fig. 2.7. In fact, this VPHG spectrograph is originally developed as an optical pyrometer, so its spectral coverage is widened at the expense of the spectral resolution. Nonetheless, the intense H_α emission could be observed in the strongly broadened form. Considering that the spectral resolution of this wide-range spectrograph is ~ 2.3 nm/pixel, FWHM of H_α line can be estimated to larger than 3 nm for the underwater streamers near the breakdown moment. Hence, this value is used to establish a major requirement of spectral resolution of 0.3 nm/pixel. It should be noted that both the quantum efficiency of CMOS sensor of the fast-frame camera and the diffraction efficiency of VPH grating are lower at shorter wavelength, the H_β line is barely detected. Meanwhile, sodium-D line at 590 nm which is known to be the strongest line from the plasma discharge in highly conductive NaCl solutions [23] is not detected either. This is attributed to very low sodium concentration contained in a tap water. Also, low

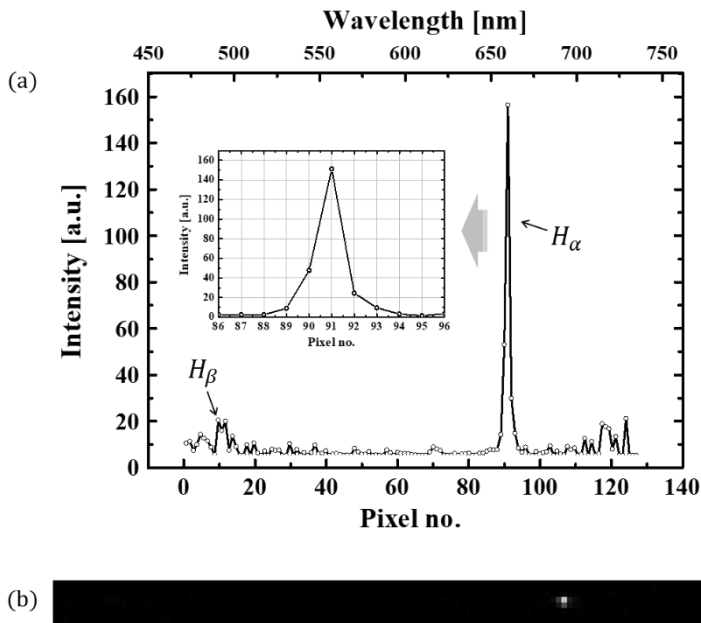


Figure 2.7. (a) Overview of the emission spectra of underwater PSD produced in tap water ($\sim 230 \mu\text{S cm}^{-1}$) with an initial voltage of 16 kV, and (b) the raw spectrum image. This spectrum is acquired at $\sim 2 \mu\text{s}$ before the breakdown using the wide-range VPHG spectrograph.

mobility of sodium ion is $6.42\text{-}6.88 \times 10^{-8} \text{ m}^2 \text{ s}^{-1} \text{ V}^{-1}$ (in water at 25°C) [68] allows only short drift distance less than $18 \mu\text{m}$ under the maximum field strength near the cathode tip ($\sim 90 \text{ kV cm}^{-1}$) during the typical exposure time (i.e., $\tau_{bd} \sim 30 \mu\text{s}$). Thus, it is difficult to expect that sodium ions play any essential role throughout the entire PSD process.

Most of design principles for the VPHG spectrograph are the same as for the conventional Czerny-Turner configuration. Thus, without recalling basic theories of

the geometrical optics, only essential steps for designing VPHG spectrograph will be concisely described here. One can look through the Ref. [69] for further details, if necessary. An achromatic lens (Nikon, 35 mm & f/2.8) is coupled with a fiber patch cable (Thorlabs, M96L02) to collect the light emitted from the underwater streamer or the spark plasma. The fiber core ($\phi 105 \mu\text{m}$) is focused on the middle of water gap by this collecting lens (35 mm). The aperture diameter of light-converging area on the water gap plane is about 0.85 mm, and it is confirmed by an inverse image of the light illuminated from the opposite side of optical fiber. Once the collected light enters the spectrograph, it passes sequentially through the collecting lens – optical fiber - entrance slit (ES) - collimating lens (L_A) - VPHG (G) - focusing lens (L_B) and finally reaches the detector (D) plane. Owing to the numerical aperture of the optical fiber ($NA_{fib} = 0.1$), the diameter of fiber core is magnified in vertical direction by the coupling distance between the fiber and the entrance slit (ES) plane ($\Delta z_{fib-ES} \cong 1.7 \text{ mm}$).

Combining this vertical magnification factor (M_{fib-ES}) of 3.25 at the ES plane with the height of the activated detector pixels ($h_D = 160 \mu\text{m}$), the maximum allowable magnification defined by the collimating (L_A) and focusing (L_B) lenses will be limited as:

$$M_{AB} = F_B/F_A \leq h_D/h_{fib}M_{fib-ES} = 0.47, \quad (2.7)$$

where F_A and F_B are the focal lengths of collimating lens and focusing lens, respectively. This criterion can be satisfied by choosing the collimating lens (Nikon,

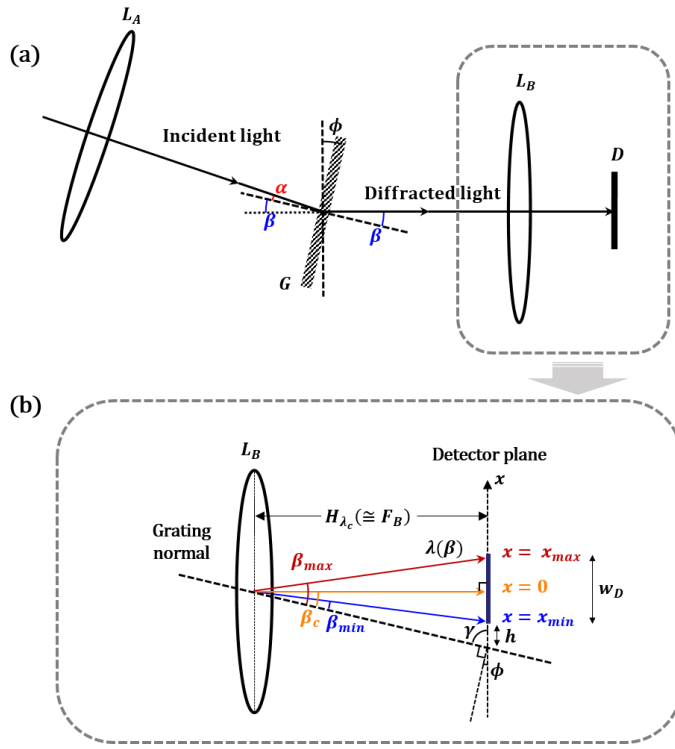


Figure 2.8. Schematic drawing for the trajectories of (a) the chief-ray of central wavelength (λ_c) around the grating and (b) the chief-rays of diffracted wavelength near the imaging plane.

300 mm & f/4.0) and focusing lens (Nikon, 135 mm & f/2) among the commercial achromatic lenses, and this combination allows the M_{AB} value of 0.45. In order to fully utilize the limited detector width in horizontal direction, the wavelength corresponding to the H_α line (i.e., 656 nm) is taken as the central wavelength (λ_c). It is noted that both the quantum efficiency of CMOS sensor of the fast-frame camera and the diffraction efficiency of VPHG (Wasatch Photonics, 600 l/mm) are optimal near the wavelength of 600 nm. In the transmissive configuration with the positive

diffraction mode number ($m = +1$), the typical trajectory of the chief-ray of central wavelength can be illustrated as shown in Fig. 2.8(a). Here, α and β are the angles of incidence and diffraction, respectively, defined in counter-clockwise from the grating normal (i.e. $\alpha < 0, \beta > 0$). Accordingly, the well-known grating equation can be given as

$$Gm\lambda = \sin \beta(\lambda) - \sin \alpha, \quad (2.8)$$

where G is the groove density [1/mm] and m is the diffraction mode number. Note that the condition $\beta \geq -\alpha$ holds for the negative incidence angle ($\alpha < 0$) at the positive diffraction mode of $m = +1$. In addition, the data sheet of VPHG gives the diffraction angle (β_c) of $\sim 12.5^\circ$ at the central wavelength. Also, an incident angle for the chief-ray can be calculated by Eq. (2.8) to 10.2° in clockwise direction from the grating normal (i.e., its sign is negative). By applying Littrow condition, the scan angle (ϕ) can be set equals to the central diffraction angle (β_c), then the angle between the grating normal and the detector normal (γ) will be determined subsequently. As a result, the horizontal width of detector plane ($w_D = 2.56$ mm) gives the range of diffraction angle from 11.91° to 13.09° . This is equivalent to the wavelength coverage of $639.2 - 672.5$ nm. Also, the spectral bandpass (B_p) is defined as

$$B_p \cong \frac{w_{pixel}}{F_B} \times \frac{d\lambda}{d\beta} = \frac{w_{pixel} \cos \beta}{F_B mG}. \quad (2.9)$$

Here, w_{pixel} is the width of a detector pixel ($20 \mu\text{m}/\text{pixel}$) and $d\lambda/d\beta$ is the reciprocal angular dispersion which is derived by differentiating Eq. (2.8). It should be noted that the central value of spectral bandpass ($B_p(\lambda_c)$) is 0.24 nm/pixel, so it

clearly satisfies the major requirement of the spectral resolution (~ 0.3 nm/pixel). Since the width of the entrance slit ($50\ \mu\text{m}$) is small enough, its horizontally magnified image on the detector plane has only a width of $22.7\ \mu\text{m}$. This value is very close to the width of a single detector pixel, so the instrumental broadening is assumed to be negligible when the Stark broadening dominates the overall spectral profile in high density condition.

2.4.3. Calibration and Data Process

Because the VPHG spectrograph has been assembled using commercial optical elements in the laboratory, its resolving performance needs to be examined by standard calibration sources. First, the instrumental broadening of VPHG spectrograph is checked using a hydrogen lamp, as shown in Fig. 2.9. Recalling that the expected width of the illuminated entrance slit was $\sim 22.7\ \mu\text{m}$ that is equivalent to ~ 1.1 pixels, the resolved light intensity is concentrated within 2 detector pixels in the spectrum image. The Gaussian fit of this spectrum profile gives the FWHM of ~ 0.239 nm, this is quite close to the design value of spectral resolution ~ 0.24 nm/pixel, assuming that the Doppler broadening of the hydrogen lamp is negligibly small in this wavelength scale.

The relation between the pixel number of detector and the actual wavelength is obtained using a standard calibration source: Ne lamp (Ocean Optics, NE-1), as

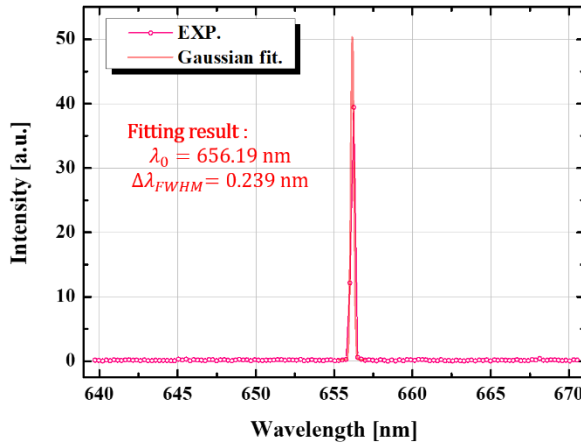


Figure 2.9. Spectrum profile of the hydrogen lamp measured with VPHG spectrograph.

shown in Fig. 2.10. The reference emission spectra of the neon lamp is acquired with commercial high-resolution spectrograph (Princeton Instrument, Acton 2500i). Conventional cubic polynomial fitting method is used to derive the pixel-wavelength relation, and the resulting spectral coverage is measured as 30.83 nm that is also very close to the designed value of 30.72 nm.

The relative efficiency calibration is also carried out, but more attention has to be paid here. The absorption coefficient of water in visible range greatly increase at a longer wavelength, so the efficiency calibration requires the similar conditions to the actual experiment as much as possible. From this respect, an auxiliary water cylinder is introduced to consider the large attenuation caused by the water surrounding the light emitting discharge channel. This cylinder is filled with distilled water, and is closed by quartz windows at both ends. The optical path length is set

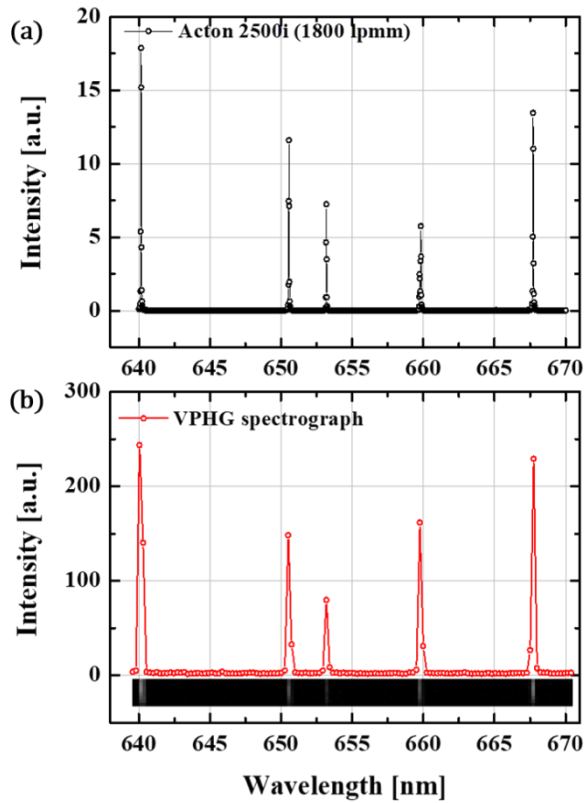


Figure 2.10. Spectrum profile of the neon lamp (NE-1) measured with (a) commercial high-resolution spectrograph (Princeton Instrument, Acton 2500i) and (b) VPHG spectrograph.

to 14.1 cm, that is equivalent to the distance from the center of water gap to the quartz window of the discharge chamber. A tungsten lamp mounted on an integrating sphere is used as a light source and another set of collecting optics is duplicated. After placing the water cylinder between the integrating sphere and the collecting lens (Nikon, 35 mm & f/2.8), the spectral irradiance curve that is partly attenuated by the water

cylinder and the collecting optics can be measured by an absolute-calibrated commercial spectrometer (Ocean Optics, HR4000CG-UV-NIR). Using this curve as a reference intensity data, the array of efficiency coefficients can be obtained from the following relation:

$$I_{ref}(\lambda_n) = A_{eff}(\lambda_n) \times I_{meas}(\lambda_n), \text{ for } 1 \leq n \leq 128, \quad (2.10)$$

where λ_n is the central wavelength, $I_{ref}(\lambda_n)$ is the reference intensity that is averaged over the spectral band-pass of the VPHG spectrograph, A_{eff} is the efficiency coefficient, $I_{meas}(\lambda_n)$ is measured intensity, and subscript n is the pixel number. The resulting efficiency coefficients can be shown as Fig. 2.11. The wavelength dependence of A_{eff} is incorporating all of the following characteristics: the spectral attenuation in transmissive media, the diffraction efficiency of VPH grating, and the quantum efficiency of CMOS sensor, however the oscillatory feature along wavelength is mainly attributed to the last factor.

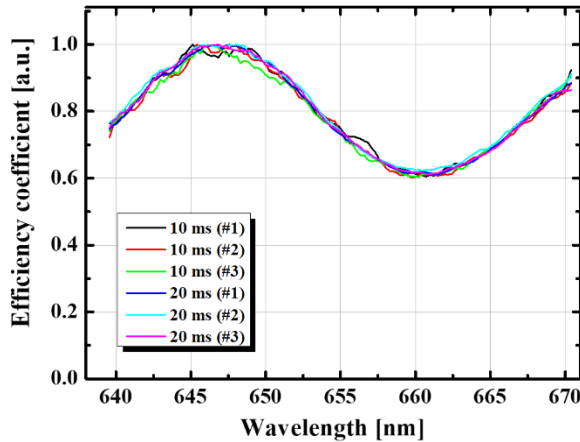


Figure 2.11. The efficiency coefficient curve of the VPHG spectrograph.

The typical procedure of n_e measurement is as follows: The light emitted from the underwater plasma is received by collecting optics mounted outside the chamber. This light will be transferred to the collimating lens of the spectrograph via optical fiber, and be expanded to a parallel beam. When the input rays enter the transmission grating they are diffracted with respect to wavelength, and thus the rays having different diffraction angles will be imaged at different position of the detector pixel by focusing lens. In this manner, the final intensity profile measured with VPHG spectrograph has the format of digital image, so this spectrum data could be processed using MATLAB®. Once the raw intensity profile ($I_0(\lambda_n)$) is extracted from the spectrum image, one can reconstruct the undistorted emission spectra ($I_1(\lambda_k)$) of

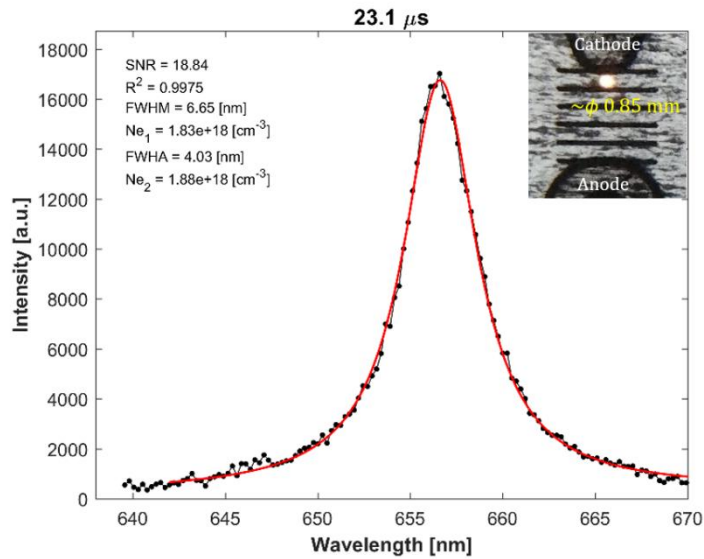


Figure 2.12. Example fit of the H_α line of the underwater streamer. Emission spectra is measured with VPHG spectrograph and the picture on the upper-right corner shows a light collecting area focused on the cathode tip vicinity.

underwater plasmas by multiplying $A_{eff}(\lambda_n)$ to $I_0(\lambda_n)$. As the broadening of line shape caused by the Stark effect is able to approximate by the Lorentzian, this efficiency corrected intensity profile (I_1) can be fed to a curve fitting routine. Considering that the Lorentzian fitting is very sensitive to the intensity profile at its wings, the fitting result tends to strongly depend on the fitting range. Thus, the optimal fitting range has to be found based on the adjusted R-square and the SNR (signal-to-noise ratio) calculated for a number of fitting ranges. The fitting sequence begins with the subtraction of baseline that is defined by the data lie outside the fitting range, then the non-linear curve fit is carried out using levenberg-marquardt algorithm. The processed fitting result will be displayed with the intensity profile (I_1) as Fig. 2.12, and the calculated values of SNR, adj-R², FWHM, and FWHA are also given together. Finally, the electron densities evaluated from both FWHM and FWHA could be presented as Ne_1 and Ne_2 , respectively. As described earlier, we believe that the n_e value calculated from Eq. (2.4) is more precise, thus this value has been treated as a measured electron density unless there is any comment in the rest of this manuscript. It should be noted here that FWHA is deduced from the fitting curve rather than the raw intensity profile because of the narrow spectral coverage of the VPHG spectrograph.

2.5. Limitations of Experiment

In the experimental characterization of the underwater plasmas appearing in PSD, several difficulties arise due to both the discharge features and the measurement device. Recalling that only the shadowgraph images and the spectrum profile of H_α line are available in our experiment, many important plasma parameters will remain unknown. For instance, the shadowgram only shows the hydrodynamic features caused by the discharge rather than the internal discharge features. That is, when trying to explain the physical mechanisms of the streamer initiation and propagation, the direct evidences such as the electronic properties of the discharge channel cannot be extracted from the shadowgraph images. Instead, only indirect information such as the distribution of self-emission intensity are available to estimate the internal structure of the discharge plasma. Moreover, the stochastic nature of the underwater PSD raises serious issues both in the spatial and the temporal dimensions. Since the OES system collects light at a fixed position of the water gap, the measured data must be dispersed by the discharge being formed along a slightly different path in each shot. In this respect, the size of the light collecting area seems too large to measure the localized parameter of the discharge plasma, however the limited sensitivity of detector may not allow to reduce the collecting area, for the sufficient level of SNR. This sensitivity issue of the detector is also combined with the limited dynamic range (12 bit-depth), so make it difficult to observe both the streamer phase and the

transition phase under the identical acquisition setup. Furthermore, the intensity of continuum radiation emitted by free-free or free-bound transitions rapidly increases as the breakdown occurs, so the Stark broadening of H_α line becomes no more discernible from the continuum. This means that only a small number of OES data can participate to describe the properties of the spark plasma at the initial phase of breakdown period. Hence, during this phase, we need an additional way of analyzing the dynamic evolution of the spark plasmas and resulting shock waves. From this context, the detailed plasma dynamics beyond the macroscopic variation of the electrical parameters will be given by the self-consistent simulation model.

Chapter 3. Advanced Self-consistent Circuit Model of Spark Discharge

This chapter is dedicated to describe the working principle of self-consistent simulation model of spark discharge. The major improvement in simulation model is the advanced circuit model developed to simulate the pulse forming action of long transmission line which is introduced to control the rate of streamer-to-arc transition. Descriptions on other minor modifications are also given in this chapter.

3.1. Advanced Circuit Model Coupled with Magneto-hydrodynamics (MHD) Code

3.1.1. MHD Equations and Material Model

As a main reference of this study, the simulation model reported in our previous work [16] has given the systematic description on underwater PSD process and the generation of underwater shock wave. This model works in a self-consistent manner for solving the one-dimensional MHD equations [54] constructed for the cylindrical spark plasma with the circuit equation for capacitive discharge. As described in Sec 1.2, the external circuit is represented by a series RLC (resistor, inductor, and capacitor)

loop treating the spark plasma as a time-varying load. Since the dynamic evolution of the spark plasma can be calculated from the MHD solver, the resulting lumped parameters such as the plasma resistance and inductance can be derived at each time-step as

$$R_p = \frac{l}{\int_0^{r_p} \sigma(r) 2\pi r dr} \quad (3.1)$$

and

$$L_p = \frac{\mu_0 l}{2\pi} \left[\ln \left(\frac{2l}{r_p(t)} \right) - \frac{3}{4} \right]. \quad (3.2)$$

Here, the plasma shape is assumed to preserve a straight cylindrical shape with the outer radius of $r_p(t)$ and length of l during entire discharge period.

For describing the dynamic behavior of spark plasma, a set of MHD equations have been formulated with the assumptions of single-fluid and resistive plasma in one-dimensional cylindrical coordinate system [16, 54] as summarized below:

$$\text{(Momentum conservation)} \quad \rho \frac{du}{dt} = -\frac{\partial p}{\partial r} - \sigma E_z B_\theta; \quad (3.3)$$

$$\text{(Equation of motion)} \quad \frac{dr}{dt} = u; \quad (3.4)$$

$$\begin{aligned} \text{(Energy conservation)} \quad & \left(\frac{\partial \varepsilon}{\partial T} \right)_\rho \frac{dT}{dt} + \left[p + \left(\frac{\partial \varepsilon}{\partial \rho^{-1}} \right)_T \right] \frac{d\rho^{-1}}{dt} \\ & = \rho^{-1} \left[Q_J + \frac{1}{r} \frac{\partial}{\partial r} \left(r \kappa_C \frac{\partial T}{\partial r} \right) - Q_R \right]; \end{aligned} \quad (3.5)$$

$$\text{(Ampere's law)} \quad \frac{1}{r} \frac{\partial}{\partial r} (r B_\theta) = \mu_0 \sigma E_z; \quad (3.6)$$

(Ohm's law)
$$E_z = \frac{I}{\int_0^{r_p} \sigma(r) \cdot 2\pi r dr}; \quad (3.7)$$

(Equation of state)
$$p = p(\rho, T), \quad \varepsilon = \varepsilon(\rho, T); \quad (3.8)$$

(Joule heating)
$$Q_J = \sigma E_z^2; \quad (3.9)$$

(Radiation loss)
$$Q_R = \sigma_S \frac{T^4}{l_p}; \quad (3.10)$$

(Planck-averaged absorption length)

$$l_p = 2.3 \times 10^{11} \frac{T^2}{n_a Z_{eff}^2} \left(\frac{k_B T}{E_i} \right) \exp\left(\frac{E_i}{k_B T} \right); \quad (3.11)$$

where t is the elapsed time from the onset of breakdown [s], r is the radial position from the central axis [m], ρ is the mass density [kg m^{-3}], u is the radial velocity [m s^{-1}], p is the pressure [Pa], E_z is the electric field [V m^{-1}] in vertical direction of the spark channel, B_θ is the azimuthal magnetic flux density [T], ε is the specific internal energy [J kg^{-1}], T is the thermal temperature [K], κ_C is the thermal conductivity [$\text{W m}^{-1} \text{K}^{-1}$], Q_R and Q_J denote the volumetric power density of radiation loss and Joule heating [W m^{-3}], respectively. The interface between discharge channel and surrounding water could be exactly traced as the governing equations are solved in Lagrangian frame. This means that the mixing of materials within the transition layer is not allowed in this description.

The system of MHD equations is closed by introducing the physical properties of plasma and liquid water. For the high density water plasma formed by PSD, the equation of state (EOS) and electrical conductivity have been adopted from Chung's earlier work [53]. The EOS model assumes the local thermodynamic

equilibrium (LTE) state for water plasma, and the non-ideal effect, which can be described as earlier in Sec.2.4.1, has been taken into account. The system of equations for solving plasma composition can be summarized as below.

■ Equations of chemical equilibrium:

$$(2\text{H}_2\text{O} \rightarrow 2\text{H}_2 + \text{O}_2) \quad n_{\text{H}_2}^2 n_{\text{O}_2} = U_1 n_{\text{H}_2\text{O}}^2; \quad (3.12)$$

$$(\text{O}_2 \rightarrow 2\text{O}) \quad n_{\text{O}}^2 = U_2 n_{\text{O}_2}; \quad (3.13)$$

$$(\text{H}_2 \rightarrow 2\text{H}) \quad n_{\text{H}}^2 = U_3 n_{\text{H}_2}; \quad (3.14)$$

$$(\text{O} + \text{H} \rightarrow \text{OH}) \quad n_{\text{OH}} = U_4 n_{\text{O}} n_{\text{H}}; \quad (3.15)$$

$$(\text{H} \rightarrow \text{H}^+ + e) \quad n_{\text{H}^+} n_e = U_5 n_{\text{H}}; \quad (3.16)$$

$$(\text{O} \rightarrow \text{O}^+ + e) \quad n_{\text{O}^+} n_e = U_6 n_{\text{O}}. \quad (3.17)$$

Here, n_j is the number density of each species denoted by j and U_k is the chemical equilibrium constant for reaction k .

■ Saha equation with Debye-Hückel correction on ionization potentials:

$$\frac{n_{k+1} n_e}{n_k} = 2 \left(\frac{4\pi m_e k_B T}{h^2} \right)^{3/2} \frac{Z_{k+1}}{Z_k} \exp\left(-\frac{I_k - \Delta I_k}{k_B T}\right), \quad (3.18)$$

where k_B is the Boltzmann constant, m_e is the electron mass, h is the Planck constant, n_e is the electron density, n_k, Z_k , and I_k are the number density, partition function, and ionization potential of the k -fold oxygen ions, respectively. The correction for the ionization potentials can be expressed as [70]

$$\Delta I_k = \frac{(z_k + 1)e^2}{4\pi\epsilon_0\lambda_D}, \quad (3.19)$$

where z_k is the ion charge number, e is the electronic charge, ϵ_0 is the permittivity

of vacuum, and $\lambda_D \left(= \sqrt{\frac{\epsilon_0 k_B T}{e^2 \sum n_k z_k^2}} \right)$ is the Debye length.

■ Additional balance equations:

$$\text{(Charge neutrality)} \quad n_{H^+} + \sum_{j=1}^8 n_{Oj^+} - n_e = 0, \quad (3.20)$$

$$\text{(Mass density)} \quad \rho = \sum_{j \neq e} n_j m_j, \quad (3.21)$$

(Atomic balance)

$$2n_{H_2} + n_H + n_{H^+} + n_{OH} = 2(2n_{O_2} + n_O + \sum_{j=1}^8 n_{Oj^+} + n_{OH}), \quad (3.22)$$

where ρ is the mass density and m_j is the mass of species j .

By iteratively solving Eqs. (1.12) - (1.22) together, the plasma composition will be determined to obtain all the EOS parameters appearing in the MHD equations. The electrical conductivity of partially ionized plasma also can be derived by the linear mixture rule (LMR) [71] as

$$\frac{1}{\sigma} = \frac{1}{\sigma_{e-n}} + \frac{1}{\sigma_{e-i}} \quad (3.23)$$

where σ_{e-n} and σ_{e-i} are the electrical conductivities arisen from collisions of electron-neutral and electron-ion, respectively. Each term on the right hand side of Eq. (3.23) can be expressed as

$$\sigma_{e-n} = \frac{n_e e^2}{m_e \bar{v}_m} = \frac{n_e e^2}{m_e v_e \sum_s n_s \sigma_{m,s}}, \quad (3.24)$$

$$\sigma_{e-i} = \frac{1}{38} \frac{\gamma_E T^{3/2}}{Z_{eff} \ln(1+1.4\Lambda_m^2)^{1/2}}, \quad (3.25)$$

where \bar{v}_m is the mean electron-neutral momentum transfer collision frequency, \bar{v}_e is the electron mean thermal speed ($=\sqrt{8k_B T/\pi m_e}$), n_s is the number density of

neutral species s , $\sigma_{m,s}$ is the momentum transfer collision cross section between electrons and neutral species s , γ_E is the correction factor for the electron-electron collision, Z_{eff} is the effective charge number of plasma ions, and $\Lambda_m = \Lambda[1 + (a_i/\lambda_D)^2]^{1/2}$ is the ratio of the modified cutoff shielding length to the impact parameter with the classical definition of Λ . Note that the contribution of the electron-ion collision used in this model is the modified Spitzer-Härm formula derived by Zollweg and Liebermann [72].

All values of EOS parameters and electrical conductivity are fed to the simulation code in tabular form structured with two independent variables: mass density ratio ($\delta = \rho/\rho_0$) and temperature (T). In contrast, the well-known Tait EOS is utilized for surrounding water in an explicit form [44]:

$$p - p_0 = A[(\rho/\rho_0)^n - 1], \quad (3.26)$$

where A and n are 300.1 MPa and 7.0, respectively. Clearly, Eq. (2.36) does not contain any temperature related terms, this means that the model ignores the thermal effect on the surrounding water that can be possibly caused by the thermal conduction or the radiative heat transfer. Tabulated electron density and conductivity data can be graphically presented as Fig. 3.1. These plots are drawn around the region of initial spark plasma, so measured electron density at the onset of breakdown that is depicted as Fig. 2.12 can give an initial region of mass density ratio (δ) and thermal temperature (T). Although the discharge is not produced in a pure water, our EOS and conductivity models are still applicable due to the very low NaCl concentration, e.g., ~0.04 wt% at

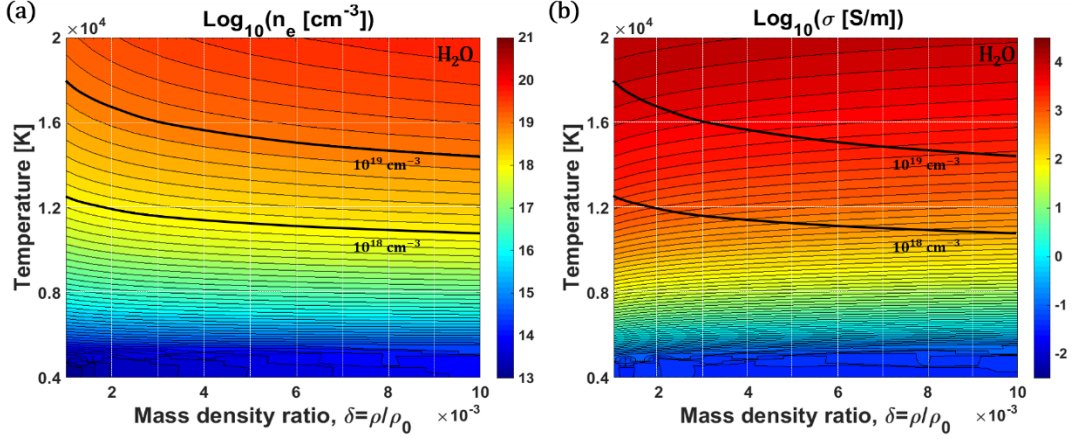


Figure 3.1. Maps for (a) the electron density and (b) electrical conductivity of water plasma calculated by Chung’s LTE model [53]. The plot range is adjusted near the initial plasma condition of PSD.

the conductivity of $500 \mu\text{S cm}^{-1}$.

Associated with the EOS and electrical conductivity models in higher density range ($\delta > 0.01$), it is necessary to confirm the validity regime of the Debye-Hückel correction on the ionization potentials. In fact, it is widely believed that the Debye-Hückel (DH) theory can seriously over-correct the ionization potentials for high density plasmas. Accordingly, large error is expected from the calculation result of plasma composition at higher density. Considering that the lowering of ionization potentials can be expressed in a generalized form [73]:

$$\Delta I_k = \frac{(z_k+1)e^2}{4\pi\epsilon_0 R_k^*}, \quad (3.27)$$

where R_k^* is the characteristic radius. Apparently, R_k^* should be defined close to λ_D

for low density and weakly non-ideal plasmas, while it approaches to some finite value for high density and highly non-ideal plasmas. For the comparison with respect to the mass density ratio, we adopted the formulae for R_k^* from the literatures as

$$\text{(Ion-sphere model [73]):} \quad R_k^* = \sqrt{\lambda_D^2 + \left(\frac{2}{3}a_k\right)^2}, \quad (3.28)$$

$$\text{(Lambda approximation [74, 75]):} \quad R_k^* = \lambda_D + \frac{1}{8}\Lambda_B, \quad (3.29)$$

where a_k is the ion-sphere radius and Λ_B is the thermal de Broglie wavelength given as

$$a_k = \left(\frac{3(z_k+1)}{4\pi m_H(1+Z_{eff})}\right)^{1/3}, \quad (3.30)$$

$$\Lambda_B = \frac{h}{\sqrt{2\pi m_e k_B T}}, \quad (3.31)$$

respectively. Here, m_H is the number density of heavy particles. In order to discuss the difference among the models for the ionization potential correction, non-ideality parameter (I_i), electrical conductivity (σ), pressure (p), and internal energy (ε) are calculated using three different models: Debye-Hückel (DH), Ion-sphere (IS), and lambda approximation (Λ), and results are compared as shown in Fig 3.2~5.

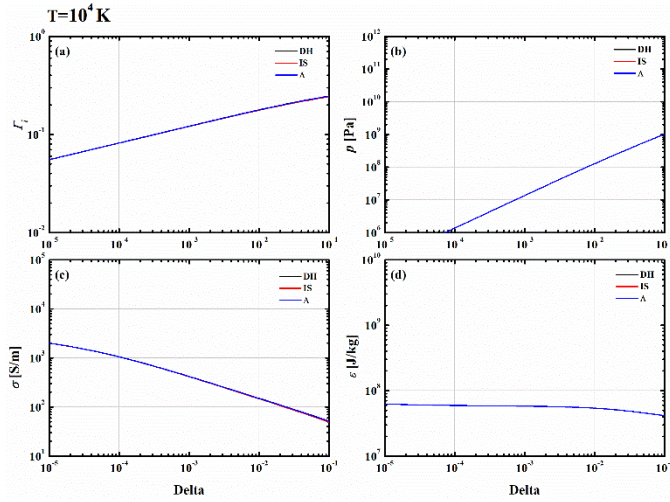


Figure 3.2. Comparison of (a) non-ideality parameter, (b) pressure, (c) electrical conductivity, and (d) internal energy calculated with different ionization potential models for water plasma at 10^4 K.

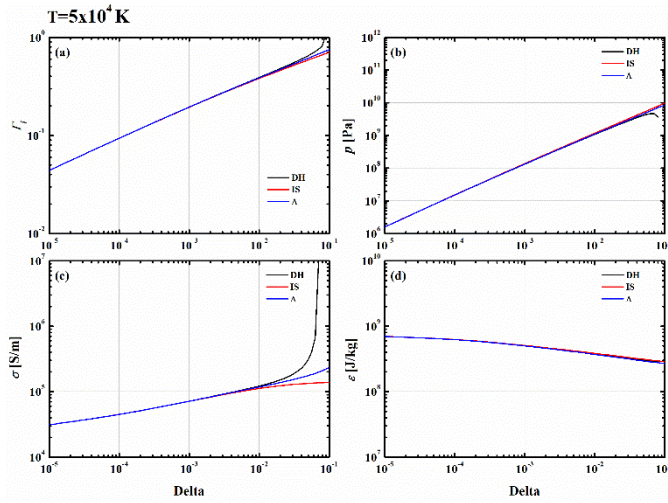


Figure 3.3. Comparison of (a) non-ideality parameter, (b) pressure, (c) electrical conductivity, and (d) internal energy calculated with different ionization potential models for water plasma at 5×10^4 K.

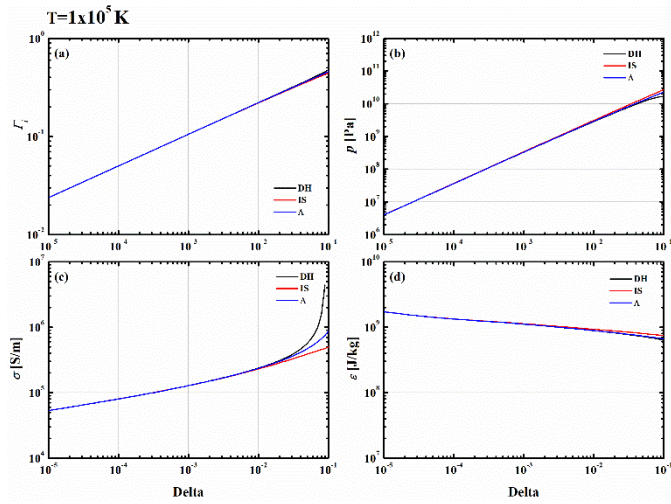


Figure 3.4. Comparison of (a) non-ideality parameter, (b) pressure, (c) electrical conductivity, and (d) internal energy calculated with different ionization potential models for water plasma at 10^5 K.

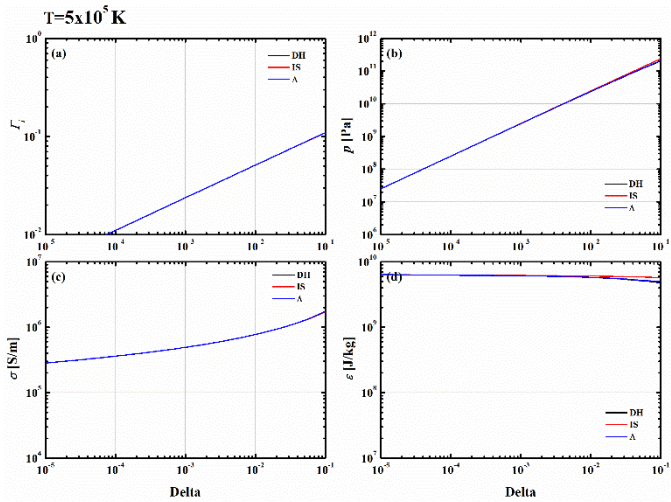


Figure 3.5. Comparison of (a) non-ideality parameter, (b) pressure, (c) electrical conductivity, and (d) internal energy calculated with different ionization potential models for water plasma at 5×10^5 K.

At low temperature of 10^4 K, all parameters are well matched to each other over a wide range of density. However, when the temperature is increased to 5×10^4 K, results given by DH model rapidly diverges at higher density ($\delta > 10^{-2}$) range, while rather moderate variations are expected by IS and Λ models. The deviation is much greater in the electrical conductivity than other thermodynamic parameters, and over a wide range of temperature, IS model gives the lowest conductivity value. Deviations among models gradually disappear as the non-ideality parameter (Γ_i) decreases with increasing temperature. Thus, IS and Λ models make clear differences only for the non-ideal plasmas of $\Gamma_i > 0.3$. It should be noted that the spark plasma discussing in the study typically have Γ_i less than 0.3 during the expansion, the differences among the ionization potential correction models do not significantly affect the numerical results. Nevertheless, the EOS and conductivity table for the water plasma has been replaced with the one using IS model to avoid the unphysical response of numerical model by the unpredictable access to such a non-ideal plasma region.

3.1.2. Initial Profile of Spark Plasma Parameters

As mentioned above, the experimental results can give the initial parameters of spark plasma. Unlike (δ_0, T_0) values, the initial channel radius (r_0) can be directly measured from the shadowgraph image. In particular, the shadowgraph images taken from the

PSD produced with the longer coaxial cable indicate the presence of layered structure in the initial spark channel: the highly conductive core and less conductive shell. If it is called as the core-shell structure, the shell region having lower electrical conductivity could be modeled as a lower temperature region. This treatment works quite reasonable because the electrical conductivity value tends to strongly depend on the electron density as well as the degree of dissociation when the temperature is lower than 10^4 K [59, 60]. Initializing the radial temperature profile in a Gaussian-like form,

$$T(r) = T_0 \exp(-r^2/\alpha_T^2), \quad (3.32)$$

with a functional parameter

$$\alpha_T = \frac{r_0}{\sqrt{\ln(T_0/T_e)}}, \quad (3.33)$$

where r_0 is the outer radius of initial plasma channel, T_0 is the core temperature, and T_e is the edge temperature. The radial profiles of conductivity and electron density calculated with the central temperature (T_0) of 1.5×10^4 K, edge temperature (T_e) of 3×10^3 K, uniform mass density ratio (δ_0) of 2×10^{-3} , outer channel radius (r_0) of 350 μm , and conductivity correction factor (k_σ) of 0.1 can be given as Fig. 3.6. Note that the electrical conductivity profile tends to be peaked more than the temperature profile, ~85% of initial current will flow through the core region. Here, the tabulated conductivity values are loaded to the simulation code and are multiplied by conductivity correction factor (k_σ) to match the experimental results more precisely. Further discussions on this issue will be given in chapter 5.

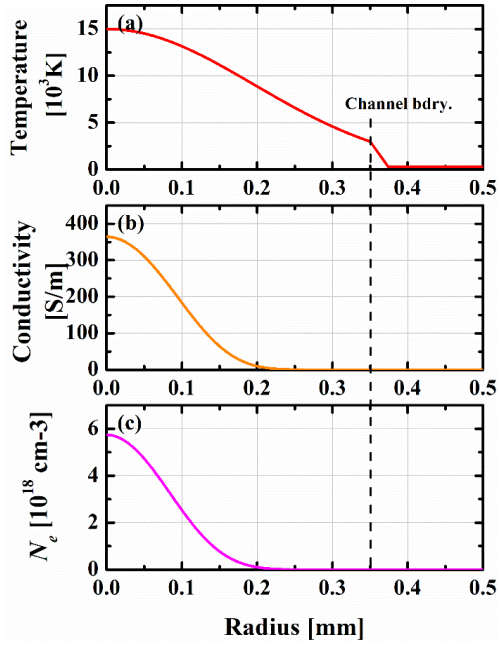


Figure 3.6. Example of the radial profiles of (a) temperature, (b) electrical conductivity, (c) electron density for initial spark plasma having a Gaussian-like temperature distribution.

As a minor modification, the blunt shape of electrode tips are fitted to the quadratic polynomials defined as

$$\text{(Cathode)} \quad f_c(r) = c (r - x_c) \cdot (r + x_c) + y_c, \quad c = r_c/x_c^2, \quad (3.34)$$

$$\text{(Anode)} \quad f_a(r) = a (r - x_a) \cdot (r + x_a) + y_a, \quad a = -r_a/x_a^2, \quad (3.35)$$

with following fitting parameters:

$$x_c = 2.02, \quad y_c = 6.5, \quad r_c = 1.5, \quad x_a = 4.04, \quad y_a = -3, \quad r_a = 3 \text{ [mm]}.$$

This treatment on the electrode's outline can be used to consider the vertical field strength which is weakened as the radial position is further away from the central axis.

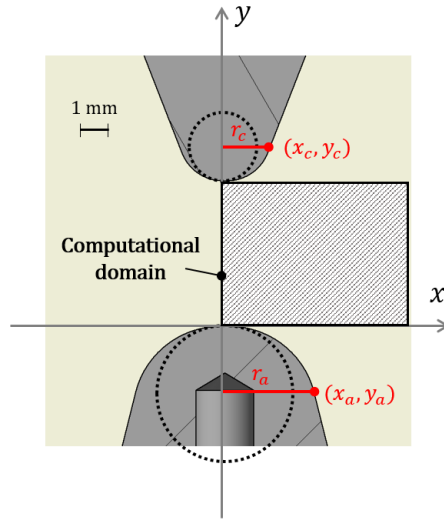


Figure 3.7. Schematic for fitting the electrode outline to correct the axial field strength.

The correction of electric field due to the increased gap distance remains less than 5% during entire simulation time (fixed to $10 \mu\text{s}$ in this work), so it does not significantly alter the numerical results. It should be noted that this treatment on the vertical electric field is based on the assumption of negligibly small radial electric field component. Hence, if we draw the equipotential lines on the computational domain, they will be aligned in horizontal direction due to this assumption.

3.1.3. Advanced Circuit Model

When trying to control the rate of streamer-to-arc transition by using a long coaxial cable, the pulse shaping effect clearly appears. In fact, the simple RLC circuit model adopted in the previous model is unable to describe the complicated electrical power

transmission in the presence of pulse forming action. In this regard, the streamer-to-arc transition process described by previous model can be criticized for the cases beyond its validity regime.

In order to deal with this issue, a standard technique using the lumped element model of coaxial cable has been introduced [76]. Instead of solving Maxwell's equations, this technique works efficiently especially where the line has a uniform cross-sectional configuration. The underlying principle of the lumped element model was established by the pioneering work of Heaviside during the 1880s [77]. The model considers parameters such as resistance, inductance, and capacitance

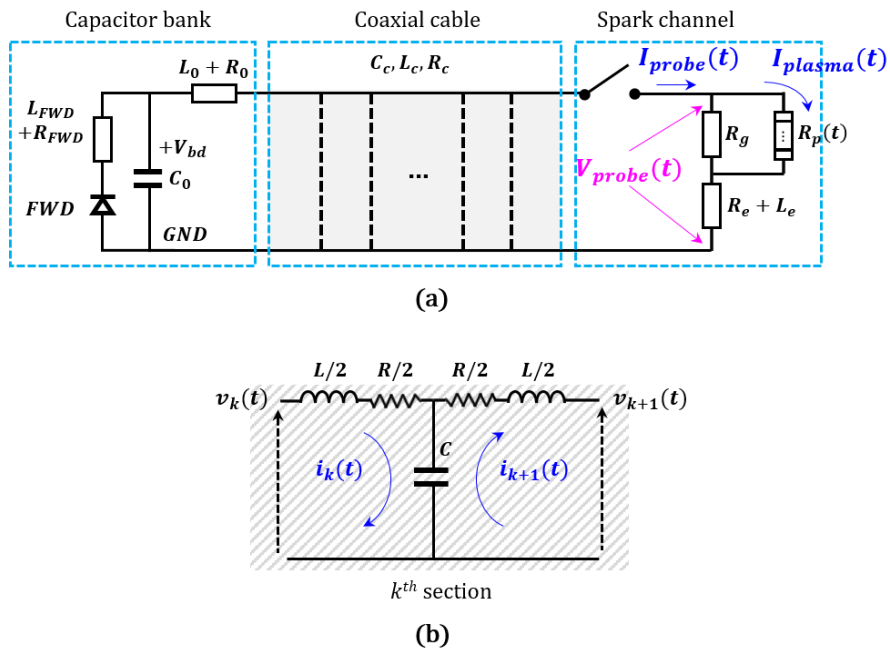


Figure 3.8. Circuit representations of (a) capacitive discharge system and (b) T-section model for transmission line.

distribution along the line. Based on this principle, a small segment of the line can be simplified to the assembly of such parameters arranged in a symmetric T-shape [78] as shown in Fig. 3.8(b). If we assume that the macroscopic properties of the line are distributed uniformly, then the line can be treated as a serial connection of a number of identical T-sections. Therefore, the capacitive discharge system in Fig. 2.1(a) can be represented as the equivalent circuit given in Fig. 3.8(a). The capacitor bank contains an internal inductance L_0 and an internal resistance R_0 in addition to the storage capacitance C_0 . An imaginary switch that is positioned at the load end of the coaxial cable implies that discharge initiation occurs with a fully charged transmission line, which is similar to the action of a basic pulse-forming line (PFL). The spark channel can be treated as the time-varying load ($R_p(t)$) connected with water gap resistance (R_g) in parallel, and there are the inductance (L_e) and resistance (R_e) of electrode assembly in series with them. If we divide the coaxial cable into N segments to construct a system of equations using a T-section model, then an equivalent circuit for an arbitrary k^{th} section can be drawn as shown in Fig. 3.8(b). The inductance, resistance, and capacitance of each segment are simply denoted by L , R , and C , respectively. The electrical parameters for each segment are defined as the macroscopic cable parameters divided by the number of the segments N . If the voltages and currents for a k^{th} section are defined as depicted in Fig. 3.8(b), we can establish the following system of linear ordinary differential equations (ODEs) by applying Kirchhoff's voltage law:

Table 3.1. Simulation parameters of PSD system.

Main power system	
Initial charging voltage (V_0)	14-22 kV
Capacitance (C_0)	0.97 μ F
Inductance (L_0)	2.5 μ H
Resistance (R_0)	70 m Ω
Coaxial cable	
Length (l_c)	1.3, 16, 93 m
Characteristic capacitance (C'_c)	0.17 nF/m
Characteristic inductance (L'_c)	0.20 μ H/m
Characteristic resistance (R'_c)	2.45 m Ω /m
Electrode assembly	
Resistance (R_e)	7 m Ω
Inductance (L_e)	80 nH
Gap distance (l_0)	5 mm
Free-wheeling diode	
Resistance (R_{FWD})	30 m Ω
Inductance (L_{FWD})	0.2 μ H

$$\left. \begin{aligned}
 & -\frac{1}{C_0} i_1 - R_0 i_1' - L_0 i_1'' = \frac{L}{2} i_1'' + \frac{R}{2} i_1' + \frac{1}{C} (i_1 - i_2), \text{ for } k = 1 \\
 & -\frac{L}{2} i_k'' - \frac{R}{2} i_k' + \frac{1}{C} (i_{k-1} - i_k) = \frac{L}{2} i_k'' + \frac{R}{2} i_k' + \frac{1}{C} (i_k - i_{k+1}), \text{ for } 2 \leq k \leq N \\
 & \quad -\frac{L}{2} i_{N+1}'' - \frac{R}{2} i_{N+1}' + \frac{1}{C} (i_N - i_{N+1}) \\
 & = (R_{p||g} + R_e) \cdot i_{N+1}' + R'_{p||g} \cdot i_{N+1} + L_e \cdot i_{N+1}'', \text{ for } k = N + 1
 \end{aligned} \right\}, (3.36)$$

where i_k' and i_k'' are the first- and second-order time derivatives of the current at the input mesh of the k^{th} section, respectively. Note that the exceptions that appear at the first and last section should be handled properly. The above equations can be

broken down into a first-order system of ODEs as the solution vector $y = [i; u]$ is introduced, where u stands for the time derivative of the current vector di/dt . The fourth-order Runge-Kutta (RK4) algorithm is used to discretize the system of ODEs, so the time marching proceeds in a fully-explicit way. Because we have $2(N+1)$ equations with an equal number of unknowns, the resulting system of difference equations is determined completely. The solution vector is initialized with

$$i^{(0)} = V_{bd} / (R_{p||g} + R_0 + R_c + R_e) \quad (3.37)$$

and

$$\mathbf{u}^{(0)} = \left(0; \dots; V_{bd} - \left(\frac{R}{2} + R_e + R_{p||g} \right) i_0 / \left(\frac{L}{2} + L_e \right) \right) \quad (3.38)$$

where V_{bd} is the breakdown voltage, R_c is the total resistance of the coaxial cable, and $R_{p||g}$ is the effective resistance of the initial plasma load and the water gap connected in parallel. Here, the initial current value corresponds to the total leakage current through $R_{p||g}$ at the moment of breakdown. The free-wheeling diode (FWD) decouples the storage capacitor when the polarity of the capacitor voltage is reversed as a result of the underdamping response of the capacitive discharge circuit. This voltage reversal corresponds to the current maximum at the cable inlet, so the terms containing C_0 are corrected after this moment. The measured electrical parameters of the pulsed power system, the coaxial cable, and the electrode assembly are summarized in Table 3.1.

Figure 3.9 illustrates the work flow of the refined simulation model.

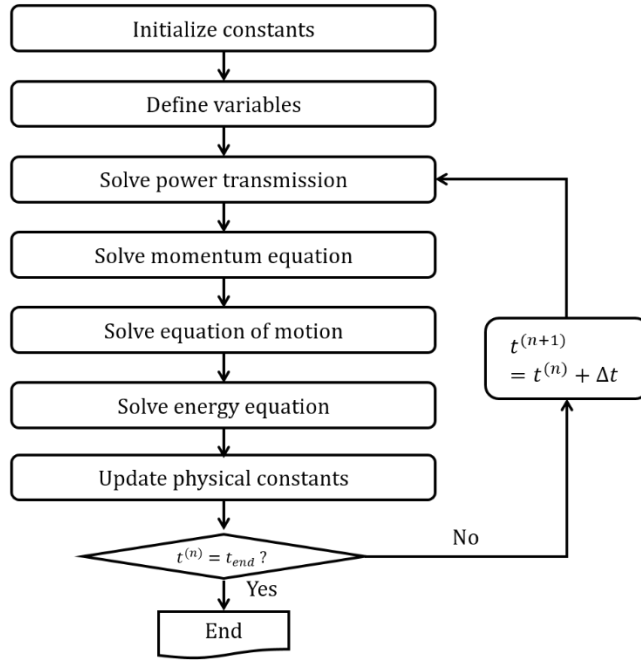


Figure 3.9. Flow of calculation in the improved simulation model.

Simulation begins as the user defines the initial parameters such as the channel radius (r_0), mass density ratio (δ_0), the temperature profile, and the breakdown voltage. The onset of discharge excites the pulse-forming action of the transmission line with a staircase-like temporal variation in current. The current and voltage values at the load-end of the coaxial cable as calculated from the transmission model provide the updated electric field strength and the total plasma current for the MHD solver. Because the current is distributed with respect to the radial profile of the electrical conductivity, the Lorentz force and the Joule heating power can be determined for each computational cell. The dynamics of the spark channel and the development of the

pressure wave in water are calculated from the MHD solver based on these updated electrical variables. The number of cells assigned to the plasma and water region is equal to 400. Because the MHD equations are solved in the Lagrangian frame, the maximum step size can be determined by the Courant-Friedrichs-Lewy (CFL) condition at each time step. The Courant number, which is set to 0.1 for all the cases, ensures that the maximum step size remains less than 10 ps during the entire simulation. The power transmission solver has a separate time-step limit because of the rise time (t_r) of the current pulse at the load end. According to the parameters given in Table 3.1, the rise time can be estimated as $t_r \cong 2.2 \times L/2R_{load} \cong 0.15$ ns. Hence, both solvers for the MHD equations and the power transmission could share the same time step as defined by the CFL condition. The outer boundary of the computational domain is defined as a rigid wall and represents the face of the imaginary pressure probe installed at 1 cm. Typical simulation time fixed to 10 μ s because it is sufficiently long duration to record the pressure wave intensity at the position of simulation boundary (i.e., 1 cm). The cylindrical pressure wave calculated at the radial position of 1 cm can be converted to the spherical pressure wave at the radial position of 10 cm using the similarity law [16, 79-81].

The common four-terminal model can be understood as an extreme case where the number of segments (N) is equal to unity in our model. In this case, the transmission line acts as a low-pass filter, so a high-frequency response cannot be exhibited. This uncertainty greatly increases for longer cable cases. Hence, 10 sections

per meter were assigned to model the coaxial cable. The convergence test has been carried out to verify the frequency response of the power transmission model in the integrated simulation.

The current and voltage values as calculated from the transmission model can be distinguished by defining each variable. That is, the measured waveforms of the current and voltage from the experiment can be compared directly as:

$$i_{probe} = i_{N+1} \quad (3.39)$$

and

$$v_{probe} = (R_e + R_{p||g})i_{N+1} + L_e u_{N+1}. \quad (3.40)$$

The current flow into the spark channel and the resistive voltage applied across the water gap can be expressed as:

$$i_{plasma} = i_{N+1} \times \frac{R_g}{(R_p + R_g)} \quad (3.41)$$

and

$$v_{plasma} = R_{p||g} i_{N+1}. \quad (3.42)$$

Thus, the effective electrical power delivered to the spark channel can be deduced from a product of the plasma current and plasma voltage. Although the advanced experimental technique narrows down the region of initial plasma parameters, the exact values of ρ_0 and T_0 are still difficult to determine. However, from the fact that the streamer-to-arc transition feature simulated by numerical model is quite insensitive to the initial plasma temperature of core region, the plausible estimation

on (δ_0, T_0) pair can be made by comparing other macroscopic parameters with experimental results, e.g., pressure wave intensity, channel radius, current-voltage waveforms, and plasma resistance.

3.2. Improvements of Numerical Results

As the most important improvement of the simulation model, the pulse forming action caused by the transmission line can be described in numerical results. In order to figure out the pulse shaping effect, numerical results calculated from the improved model are compared with those from previous model as shown in Fig. 3.10. In the case of short cable (1.3 m), there is no clear difference between numerical results from both models, except for the action of FWD which is turned on at the current maximum ($\sim 2.5 \mu\text{s}$). On the contrary, the staircase-like variation of current waveform in the case of long cable (93 m) clearly appears in the numerical results of advanced model. The duration of each current step is twice the signal propagation time through the coaxial cable, which is defined by

$$t_p = 2l_c \sqrt{L'_c C'_c}, \quad (3.43)$$

where l_c is the cable length (m), L'_c and C'_c are the distributed inductance (H/m) and capacitance (F/m) per unit length of cable, respectively. The voltage loading coefficient α_v can be defined as

$$\alpha_v = \frac{R_{p||g}(t_0)}{R_{p||g}(t_0) + Z_0}, \quad (3.44)$$

where Z_0 is the characteristic impedance of coaxial cable ($= \sqrt{L/C} \cong 35 \Omega$). Then, the magnitude of the first current step will be limited to $\alpha_v \times V_{bd}/Z_0 \sim 500 \text{ A}$ at the breakdown voltage of $\sim 18 \text{ kV}$. In fact, this initial current step is provided from the energy stored in the transmission line itself, and the main stored energy in the capacitor bank can affect the load characteristics after a time delay of t_p via

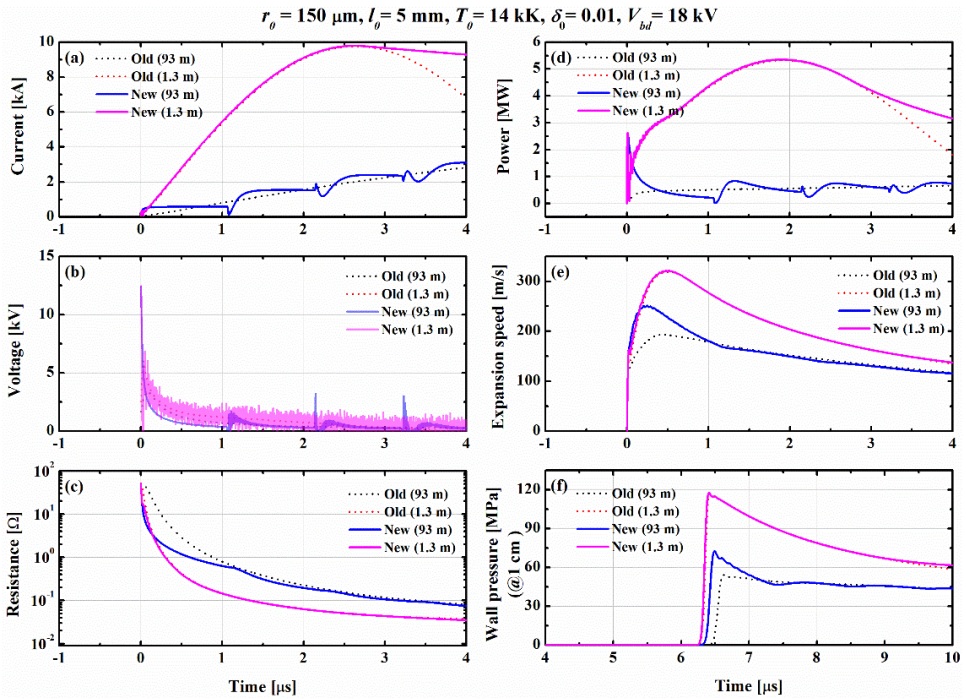


Figure 3.10. Comparison of numerical results by different power transmission models in the early stage of spark discharges with short (1.3 m) and long (93 m) cables: (a) probe current, (b) probe voltage, (c) plasma resistance, (d) delivered power, (e) radial expansion speed, and (f) wall pressure at 1 cm.

subsequent current pulses. Thus, the importance of the pulse forming action is can be emphasized at the very early phase of streamer-to-arc transition. Compared to the results from old model, the initial current released from the transmission line certainly heats up the spark channel, so the resistance of spark channel more rapidly decreases in new model. This features are also accompanied by the faster channel expansion and higher shock wave intensity.

The experimental validation of improved circuit model has been carried out by comparing the numerical results with measured current and voltage waveforms as shown in Fig. 3.11. Note that the data used in this figure are measured at the position of the cable inlet. Also, the FWD is deactivated to allow the underdamping oscillation. The simulated waveforms agree well with the measured ones not only in the overall oscillatory behavior but also in the detailed step-wise variations. Here, it should be noted that the waveforms probed at the cable inlet are insensitive to the detailed time-varying characteristics of spark plasma, thus it is relative easy to match the numerical results to measured ones. In other words, if we intend more rigorous experimental validation for the model associated with the evolution of plasma parameters, measuring parameters suggested in Fig. 3.8(a) are much preferred due to their sensitivity to the plasma load. Nevertheless, this result is sufficient to show that the advanced circuit model describes the pulse forming action caused by long transmission line very precisely.

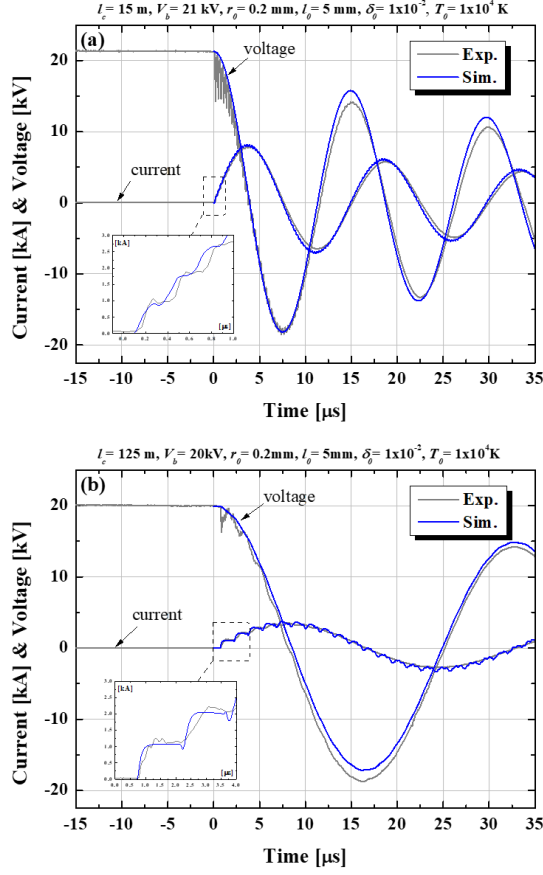


Figure 3.11. Comparison of current and voltage waveforms measured at inlet side of cable, with numerical results for different cable lengths: (a) 15 m and (b) 125 m.

If we introduce the acceleration time t^* as the elapsed time until the radial expansion rate of the spark channel reaches its maximum, the delivered energy to this moment is given by [41]

$$E^* = \int_0^{t^*} i_{plasma}(t) \cdot v_{plasma}(t) dt. \quad (3.40)$$

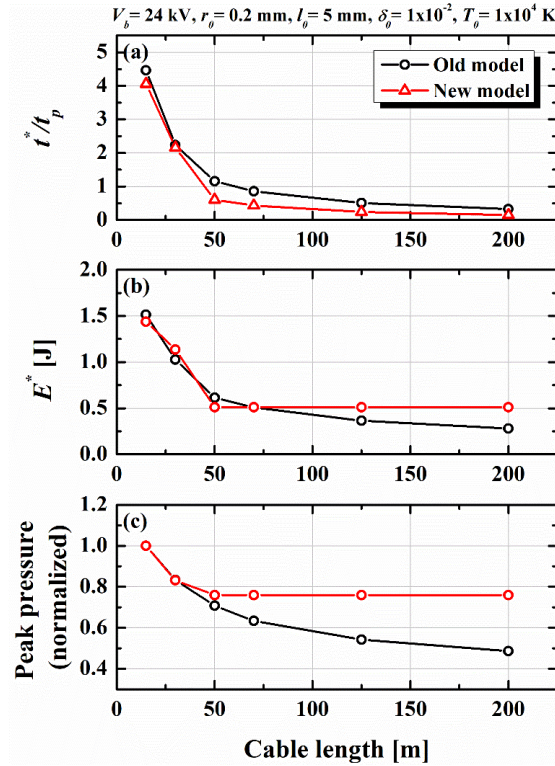


Figure 3.12. Variation of parameters that contribute to the development of shock waves with cable lengths: (a) ratio between t^* and t_p , (b) energy delivered to the spark channel until t^* , and (c) peak pressure normalized by result of 15 m-long cable. Comparison of numerical results from new and old models.

The analogy between the development of the dynamic shock wave by an expanding spark channel that pushes surrounding water and the motion of the accelerating piston indicates that only a small amount of energy E^* can contribute to creating the shock wave. Because the values of t^* and E^* depend on how the electrical power transmission is interpreted, the resulting strength of the pressure wave can be expected

to vary by a certain amount depending on the transmission model. Trying to establish a simple correlation between t^* and E^* , these parameters are extracted from the numerical results of the new model and are compared with those from the old model, as shown in Fig. 3.12. When we assume the uniform initial plasma profile, the acceleration time t^* does not exceed $1\ \mu\text{s}$ in most cases, so the ratio t^*/t_p decreases in inverse proportion to the cable length. Large t^*/t_p ratio means that the signal propagation time is sufficiently short so that the oscillatory circuit response can be exhibited. Thus, for shorter cables, there is no significant difference in the results even if the pulse forming action is not considered. However, if the cable gets longer and the t^*/t_p ratio becomes less than 1, the situation will change. The E^* value saturates as the cable length (l_c) increases because only the energy delivered by the first current step can be involved in the initial expansion of the spark channel. For the specific cable that was used, this saturation occurs when $l_c \geq 50\ \text{m}$. On the contrary, E^* decreases gradually as l_c increases in the old model. This is because the time derivative of current (di/dt) released from the capacitor is limited by the inductance of the coaxial cable. Such a limited initial heating slows down the initial spark channel expansion. For the cases where l_c is 50 and 70 m, E^* is similar to the values of the new model, but the resulting peak pressures are predicted to be weaker. This means that E^* is not the only parameter that determines the shock strength and that power deposition during the initial expansion of the spark channel is also important. The new model addresses the problem of the old model that underestimates the peak pressure

significantly, especially for longer cables. If we assume that the same initial conditions exist on the spark channel, the reduction in peak pressure is expected to be only ~20% as l_c increases to 125 m. Here, it should be emphasized that above quantitative analysis becomes valid only if the assumption on the initial plasma property is correct. Therefore, further discussions beyond these general features of advanced model will be followed by the actual experimental results presented in chapter 5.

3.3. Limitations of Model

Although some weak points of previous work are covered by present work, there are still several limitations in the simulation model. Here, we are addressing the issues associated with the surrounding water layer, the radiation transport and the multi-dimensional phenomena.

Present model is completely ignoring the heat transfer to the surrounding water. Accordingly, the vaporization and condensation of the surrounding water layer which can be caused by the thermal conduction or the radiative heat transfer are neglected. In fact, if there is significant radiation loss from the plasma volume, photons with the energies of 13.6 – 50 eV will be absorbed by liquid water owing to their short path length ($\sim 0.01 \mu\text{m}$) [82]. Hence, the additional ionization may occur and subsequently the certain fraction of discharge current can flows through such a thin layer. That is, in the absence of considerations on the additional vaporization and

ionization within the surrounding water layer, the expansion rate of spark channel can be possibly underestimated. This presumption is particularly plausible in the cases of large discharge current and long discharge duration where the heat transfer effect is no longer negligible.

The issue of the radiation transport inside the spark plasma is even more critical. The assumption of optically thin body allows the maximum radiation heat flux escaping out of plasma volume, this leads to the significant error in the analysis of the longer time evolutions of spark plasma. By definition, the Planck mean free path (l_p) adopted in present model can be used to describe the volumetric emission of thermal radiation from an optically thin body. However, the l_p value becomes comparable or even less than the radial dimension of spark channel (r_p). Clearly, the basic criterion for assuming the optically thin plasma ($r_p \ll l_p$) will be violated in the middle of discharge simulation. Consequently, the volumetric loss of radiation power under the assumption of an optically thin plasma ($\sigma_S T^4/l_p$) becomes prohibitively large for some cases. Moreover, the heat conduction process can be promoted by the active radiation transport particularly when the local thermodynamic equilibrium between the radiation field and the plasma fluid has been reached [83]. As a result, the temperature profile inside the plasma channel can be flattened, leading to the lower effective resistance and the faster expansion rate of the spark channel. Hence, this issue is also expected to contribute to the underestimation of the channel expansion rate.

The last issue is coupled to finite computational dimension of the present model. Obviously, the shape of discharge channel is not symmetric in cylindrical geometry, and physical phenomena appearing in vertical direction are also present at the same time. In particular, the influence of vertical hydrodynamic phenomena such as the reflected waves from the electrode surfaces is still recognized as unsolved problem. Hence, this issue requires the improvement of simulation code to a multi-dimensional one. However, the basic structure of MHD solver utilizing the Lagrangian description is inappropriate for the multi-dimensional analysis due to the critical issue of mesh tangling. In this respect, the extension of simulation model should be carefully pursued in a long-term view.

The above-mentioned issues can influence on the overall dynamics of spark plasma significantly. Nevertheless, the thermophysical phenomena described by the electrical power deposition and the single-fluid MHD equations in the present model still allow the valuable discussions on the streamer-to-arc transition features and resulting shock wave formation process. Thus, we insist that the essence of this study can be conserved. Further discussions on these issues will be given in chapter 5 in a qualitative manner.

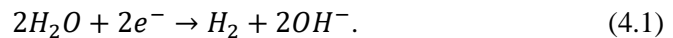
Chapter 4. Characterization of Negative Subsonic Streamer

4.1. Preliminary Experiments

As mentioned before, the electrolysis treatment has been introduced to minimize the uncertainties arising from the bubble formation process during the pre-breakdown period. In this section, results from the preliminary experiments performed mainly with the tap water are presented for the general description of PSD process assisted by electrolysis treatment.

4.1.1. Over-voltage Electrolysis

Refer to Fig. 2.1, a preconditioning pulse modulator is attached in parallel with the main power system to electrolyze the water before injecting the HV pulse. During the preconditioning period, hydrogen bubbles can be produced on the cathode surface via following reaction:



Ideally, the rate of above reaction is proportional to the current density driven in the reactor. This means that one can control the speed of hydrogen production at certain

discharge condition by adjusting the applied voltage. Within the electrical conductivity range of interest (i.e., 200-500 $\mu\text{S cm}^{-1}$), the minimum potential of 1.229 V for the reaction is too low to produce the sufficient amount of hydrogen bubbles during the typical off-period between successive discharges (1-2 s range). Hence, the amplitude of preconditioning pulse is raised to 400 V in this work. Note that the detailed analysis on the over-voltage electrolysis reaction as well as the kinetics of reaction products are out of scope. Instead, macroscopic information such as the current-voltage waveforms and the shadowgraph images of microbubbles are observed to catch the qualitative features of the electrolysis reaction.

Figure 4.1 shows the electrolysis reaction in tap water (230 $\mu\text{S cm}^{-1}$) and the hydrogen is actively created at the cathode surface in the form of microbubble. The first set of microbubbles emerges at ~ 50 ms and then the number of bubbles steadily increases. This initial delay is necessary for the reduction of solubility from super-saturated state to quasi-equilibrium state [84]. As the electrolysis reaction continues, the water and bubbles begin convective motion (~ 7 cm s^{-1}) toward the anode. This may result from the drift of negative ions or the mass transfer by the reaction products. Additionally, because the bubble-liquid interface prefers to be charged negatively [85], the field-driven motion continues against buoyancy. The gradual variation of the current-voltage waveforms indicate that the effective electrical conductivity of the water gap ($\bar{\sigma}_{water}$) slightly increases during the preconditioning treatment. As mentioned earlier, the reaction products can be formed

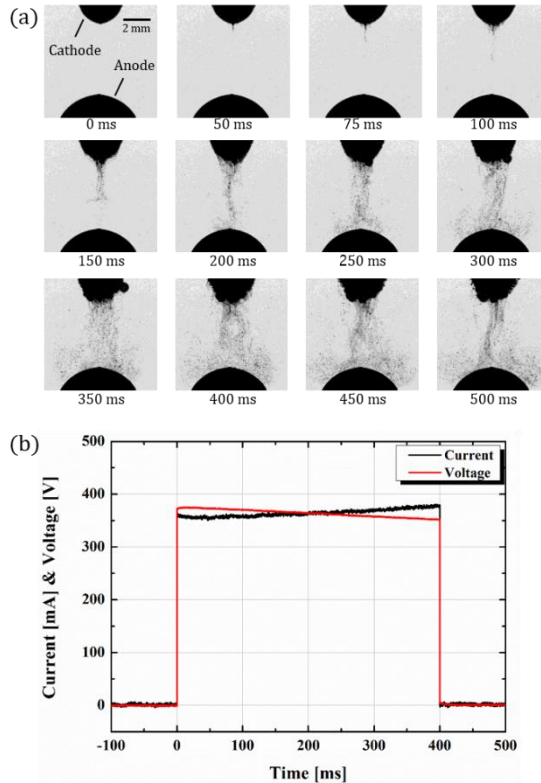


Figure 4.1. Electrolysis of tap water ($230 \mu\text{s cm}^{-1}$) via preconditioning pulse:

- (a) shadowgraph images of the water gap with an exposure time of $0.3 \mu\text{s}$ and**
- (b) synchronized gap voltage and discharge current waveforms.**

more actively in higher $\bar{\sigma}_{water}$ cases due to higher current density. Thus, it can be expected that the widely spread hydrogen microbubbles and mobile ions (e.g., OH^-) may affect not only the streamer initiation process but also its morphology.

The electrolysis treatment is performed in NaCl solutions with higher conductivities ($500, 750 \mu\text{S cm}^{-1}$). From the shadowgram shown as Fig 4.2, we found different preconditioning durations for creating hydrogen bubbles in a merged form.

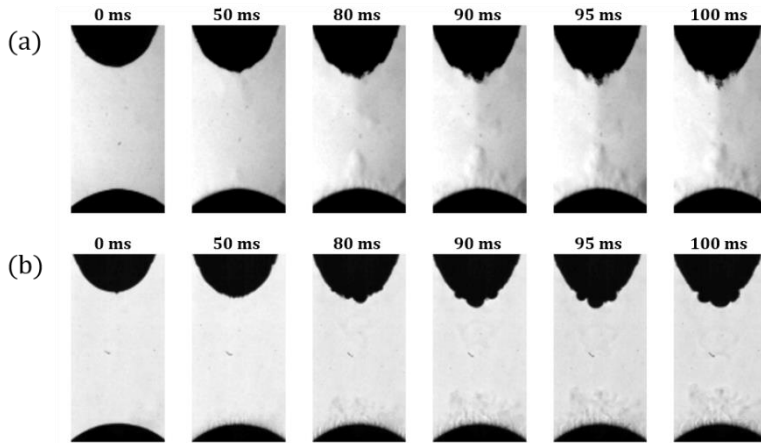


Figure 4.2. Shadowgraph images obtained from electrolysis of NaCl solution at different conductivity: (a) $500 \mu\text{S cm}^{-1}$ and (b) $750 \mu\text{S cm}^{-1}$.

The time required to reduce the solubility did not change so much. However, the higher the conductivity of water, the faster the production of merged hydrogen bubbles. Once the hydrogen bubble appears in a merged form, the number of merged bubbles rapidly increases at higher conductivity. They no longer able to drift toward the anode against buoyancy due to their large size. The floating motion of merged bubbles are quite slow in several tens of ms, so the optimal preconditioning duration to minimize the uncertainty associated with the pre-breakdown process can be determined by stochastic feature of the electrolysis reaction. The stochastic nature of the electrolysis tends to be strengthened where the reaction is difficult to take place. In particular, a passivation layer can be easily formed on the anode surface in the case of low $\bar{\sigma}_{water}$. Accordingly, one can hardly expect the merit of electrolysis treatment in this case. In

a similar context, the arc discharge developed in the previous discharge affect the next discharge because it can remove the passivation layer of the anode surface very effectively. Meanwhile, it is possible to produce oxygen bubbles on the anode surface only if the water conductivity is sufficiently high. In this case, positive streamers participate into the electrical breakdown process occasionally. Such discharge conditions are intentionally avoided in order to focus on the negative subsonic discharge mode in this study.

When the hydrostatic pressure is increased, the electrolysis reaction proceeds in a somewhat different manner. As shown in Fig. 4.3, the convective motion of microbubbles gets reduced because the buoyancy force is increased at higher pressure. Also, it is observed that the microbubbles seldom associate with each other at higher pressure. This feature is important because the hydrogen bubbles in a merged form

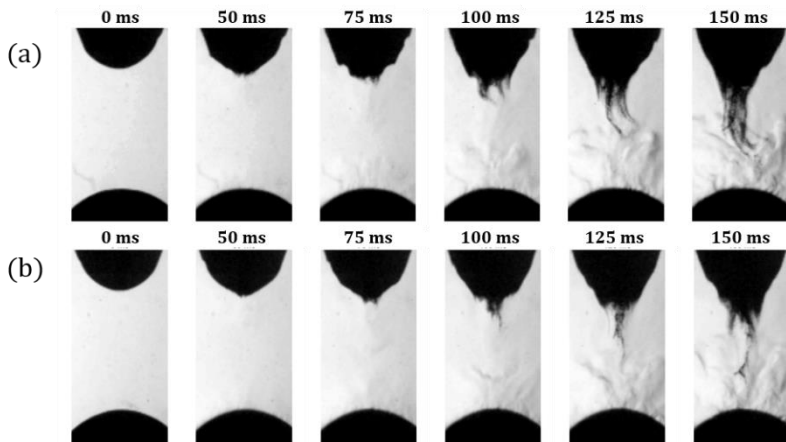


Figure 4.3. Shadowgraph images obtained from electrolysis of NaCl solution ($500 \mu\text{S cm}^{-1}$) at different pressure: (a) 2 atm, (b) 3 atm.

are extremely helpful to accelerate the initiation of underwater streamers. The solubility of hydrogen must be increased at higher pressure, but there is no significant difference in the time at which the first set of microbubbles emerges. This indicates that the solubility reduction process to the quasi-equilibrium state is insensitive to the hydrostatic pressure that is changed within 1-3 atm range in the experiments. Hence, the low probability of bubble merging at high pressure condition needs to be explained in a different way.

When the total gas concentration is much greater than that of dissolved gas in the liquid, there are two mechanisms of bubble growth [86]. In the initial phase, free molecules are pushed out from the liquid and are attached to each other. As the attachment process continues, the rate of attachment (v_{at}) will increase due to increasing surface area. If the attachment rate is sufficiently large compared to the characteristic floating time (τ_{fl}), i.e., $v_{at}\tau_{fl} \gg 1$, then bubbles can grow further by coagulation. The association process of two bubbles in a liquid can be understood by an analogy to the association of two clusters in a gas. For our water gap structure, hydrogen bubbles tend to stagnate near the cathode surface, the bubbles will grow mainly by coagulation mechanism. Unlike the rate of coagulation process, the floating time and size of bubbles depend on the initial conditions, particularly the initial concentration of gas molecules in the liquid [86]. Accordingly, both the size and spatial distribution of hydrogen microbubbles are the main factors that make bubbles difficult to develop into merged form at high pressure condition.

4.1.2. Role of Initial Bubbles

In the absence of impurities, Ohmic heating on the liquid can continue beyond the normal boiling temperature. This is called the explosive boiling or the burst-like boiling [87], and the massive nucleation process is usually followed. In the case of pure water, the threshold heat flux value for the massive nucleation is given as $\sim 4 \times 10^4 \text{ W cm}^{-2}$ [88]. On the other hand, the water begins boiling at its normal boiling point when it contains impurities. Impurities usually act as nucleation cores [20, 87] by attracting the free molecules from the heated water. Obviously, the latter case is very common unless the experimental condition is managed with an extreme care. In this study, hydrogen microbubbles produced by electrolysis are assumed a sort of impurity, so our experimental conditions also correspond to this case.

The preliminary experiments are carried out in the conditions slightly different from the main experiment [89]. Here, we used the tap water ($\sim 230 \text{ }\mu\text{S cm}^{-1}$) and the larger storage capacitor ($2.6 \text{ }\mu\text{F}$). During the pre-breakdown period, the current-voltage waveforms for different preconditioning durations are as shown in Fig. 4.4. When the main HV pulse is applied, the water gap allows continuous current flow. The current varies smoothly throughout the pre-breakdown period but steeply rises at the transition to the breakdown period. Figure 4.5 indicates that this transition point is caused by streamer inception. The gap voltage is reduced continuously by RC decay (half peak width: $\sim 1.8 \text{ ms}$) of the main discharge circuit. The effective gap resistance

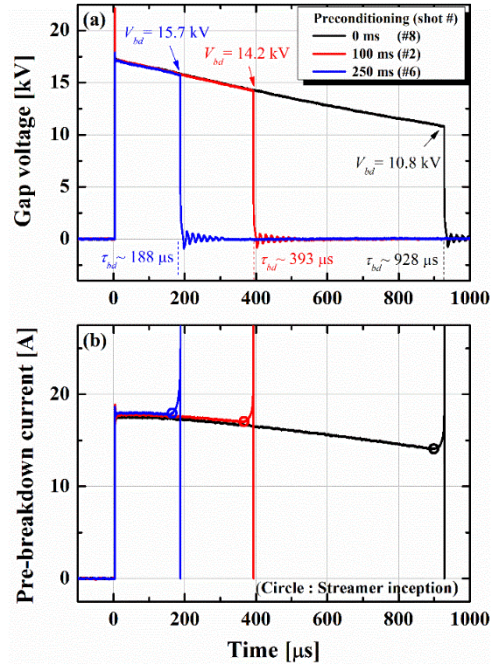


Figure 4.4. Influence of the preconditioning pulse on the pre-breakdown process: measured waveforms of (a) gap voltage and (b) pre-breakdown current. The data closest to the average of 10 repeated shots were selected for display. Both the breakdown delay (τ_{bd}) and breakdown voltage (V_{bd}) values are from the waveforms shown in the figure.

$R_{gap}(t)$ is slightly reduced by longer preconditioning pulses, which is consistent with the observations from Fig. 4.1. However, based on the data acquired from 10 repeated shots, it is interesting to note that the breakdown delay (τ_{bd}) is reduced dramatically from $931 (\pm 74) \mu\text{s}$ to $122 (\pm 82) \mu\text{s}$ without any significant differences in the overall current-voltage waveform trend. Here, the breakdown delay τ_{bd} is defined as the time interval between application of the main high-voltage pulse and the sudden

drop in the gap voltage. Note that a reduced τ_{bd} definitely leads to a reduction in energy consumption during the pre-breakdown period. The residual voltage of the capacitor at the onset of breakdown (V_{bd}) therefore also increases from 10.8 (± 0.4) kV to 16.2 (± 0.6) kV.

A typical pre-breakdown process without the initial microbubbles is shown in Fig. 4.5(a). This discharge mode is accompanied by formation of very large vapor bubbles (radius ~ 0.66 mm), which takes approximately 90% of the total pre-breakdown period. Given that the vapor bubbles are primarily formed by Joule heating [23], considerable time consumption can be attributed to the low field strength at the cathode tip. After sufficient expansion time, the surface instability that occurs in the merged bubble evolves into the form of protrusions. Negative streamers are initiated at the tips of these protrusions and propagate towards the anode at subsonic speeds (~ 144 m s⁻¹). These streamers have tree-like structures with thick stalks and short branches, as reported by Li *et al.* [6].

The pre-breakdown process acceleration mechanism can be illustrated using Fig. 4.5(b). As a main product of electrolysis, the hydrogen microbubbles are distributed near the cathode at the moment of high-voltage application. These microbubbles then become a nucleation site for the vapor bubble [15] and its formative time is greatly reduced. Consequently, both the protrusion and the streamer are initiated from smaller vapor bubbles at much earlier times. The field structure that appears as a haze indirectly shows that the aqua ions are distributed throughout the

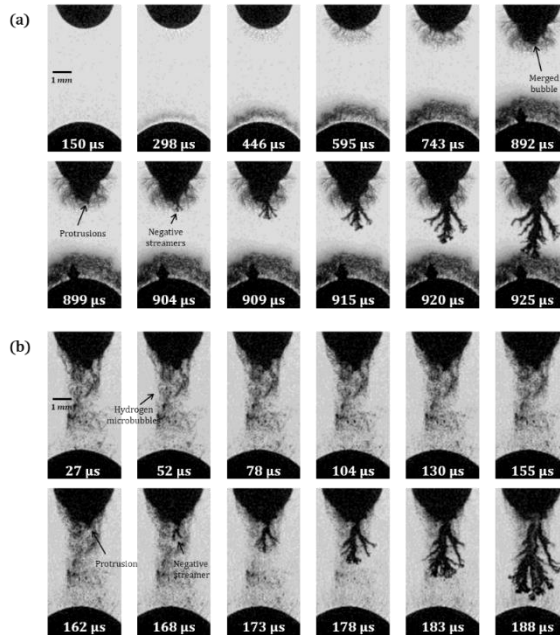


Figure 4.5. Initiation of bubbles and streamers at a charging voltage of 17 kV: (a) without and (b) with a preconditioning pulse (400 V, 250 ms) before the HV pulse application. The shadowgraph images shown in (a) and (b) are synchronized with the waveforms indicated by the black and blue lines, respectively, in Fig. 4.4.

water gap. This is consistent with the change in $R_{gap}(t)$, which is reduced by the electrolysis process. The slightly faster propagation speed ($\sim 172 \text{ m s}^{-1}$), thicker stalk and broader branches of the streamer can also be understood similarly.

The breakdown parameters affected by the initial microbubbles can be summarized as shown in Fig. 4.6. The breakdown delay τ_{bd} decreases almost linearly as the preconditioning pulse increases to 250 ms. The total energy, i.e., the

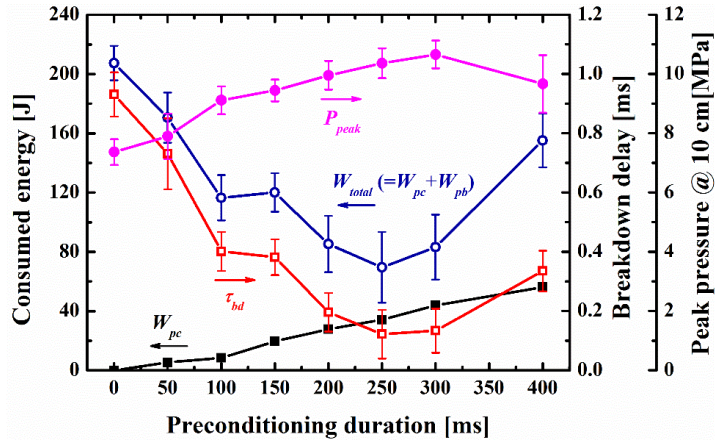


Figure 4.6. Influence of electrolysis pulse duration on breakdown parameters: energies required for preconditioning treatment (W_{pc}) and the entire discharge ($W_{tot} = W_{pc} + W_{pb}$), the pre-breakdown delay (τ_{bd}), and the measured peak pressure (P_{pk}).

sum of energies consumed during the preconditioning period (W_{pc}) and the pre-breakdown period (W_{pb}), also decreases gradually. Note that W_{pc} and W_{pb} are determined by integrating the products of the measured current-voltage waveforms. Interestingly, the total energy required to cause final breakdown (W_{total}) can be minimized by optimizing the electrolysis treatment duration. The optimal time is 250 ms under our experimental conditions. At this point, the energy required during the pre-breakdown period (W_{pb}) was significantly reduced by ~84%. However, it should be noted that the effectiveness of the preconditioning decreases when too many microbubbles are produced. This is presumably because of the non-uniform microbubble distribution near the cathode tip. Simultaneously, as the mass of

microbubbles floats away, the effective number of the initial bubbles residing on the cathode tip decreases to that of the shorter preconditioning duration. However, it is also interesting that the temporal jitter in τ_{bd} is quite similar for a wide range of preconditioning durations.

When breakdown occurs, the spark channel formed by the streamers expands rapidly and develops a pressure wave in the surrounding water. Figure 4.7 shows that this pressure wave can be effectively enhanced by providing initial hydrogen microbubbles. We observed that the measured peak pressure is enhanced remarkably by ~ 3 MPa, equivalent to $\sim 40\%$, when the preconditioning duration is extended to 250

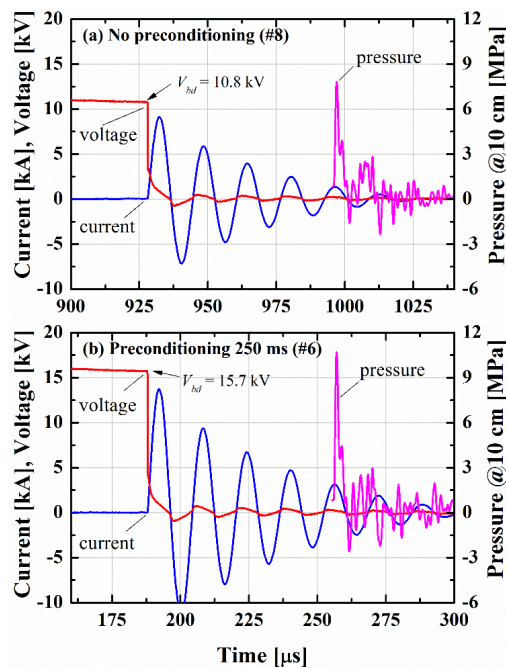


Figure 4.7. Voltage, current, and pressure waveforms for an initial charging voltage of 17 kV: (a) without and (b) with a preconditioning pulse (400 V, 250 ms).

ms. Note that when it is determined by the shock strength, the optimal preconditioning duration changes to 300 ms, and there are two possible explanations for this subtle change. The first is that as $\bar{\sigma}_{water}$ increases because of the longer preconditioning treatment, the streamer stalk thickens and the radius of the initial spark channel may also increase. The second is that when the mass of hydrogen microbubbles is floated away from the cathode tip by buoyancy, the effective length of the initial spark channel could increase slightly in cases where the streamer is initiated immediately from this mass. It is thus expected that the orientation of electrode assembly will affect the optimal preconditioning parameters.

Figure 4.7 shows the waveforms measured during the breakdown period for two different cases to enable discussion of the shock wave enhancement mechanism. In our experiments, the peak pressure is enhanced (~ 3 MPa) where V_{bd} increases by only ~ 5.4 kV on average as a result of reduced τ_{bd} . However, this increment could be achieved by an additional charging voltage of 8 kV in the standard positive discharge mode [36]. This implies that another factor other than increased V_{bd} contributes to the pressure buildup. The development of the pressure wave involves a number of factors, including the initial spark channel properties (e.g., length, radius, density) and the circuit parameters (e.g., capacitance, line inductance, charging voltage) [16, 41]. Given that the measured peak pressure in the positive discharges (typically, $V_{bd} \sim 14$ kV at $\tau_{bd} \sim 538$ μ s) when using the reversed electrode pair ($g_+ \sim 2.3$) was only ~ 7 MPa [16, 36], there appears to be a clear contribution for higher

peak pressures (~ 10 MPa) from the negative streamer morphology, i.e., from their thicker and longer stalks.

4.2. Streamer Initiation

From this section, results obtained from the main experimental setup introduced in chapter 2 will be presented to understand the evolution of negative subsonic streamers.

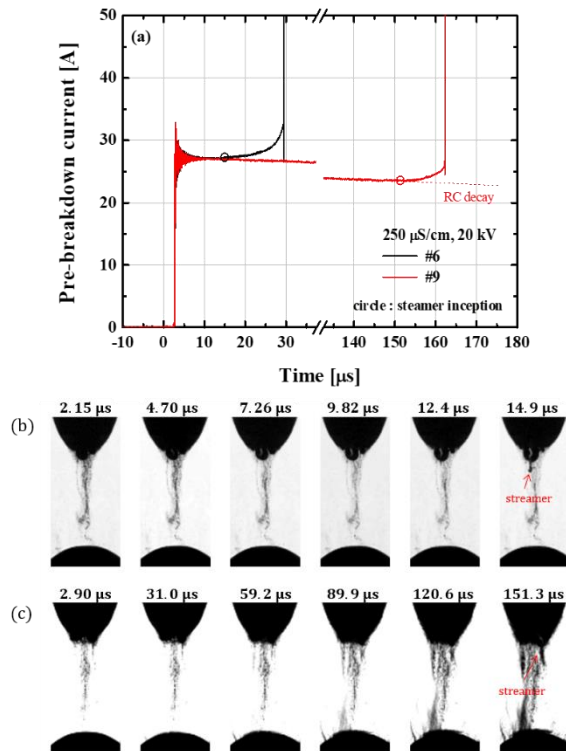


Figure 4.8. Two different mode of streamer initiation: (a) pre-breakdown current waveform, shadowgraph images of (b) fast and (c) slow ignition mode.

As mentioned in the previous section, hydrogen microbubbles produced by electrolysis treatment can promote the additional bubble formation by providing nucleation site. Moreover, if the electrolysis is sustained sufficiently long (in Fig 4.8, 200 ms), hydrogen bubbles with large radius can be formed on the cathode surface. In this case, the initial hydrogen bubble can ignite the underwater streamer in a quite different manner. Provided the proper position, size, and contact condition of initial bubble, much faster discharge mode can be realized without additional bubble formation as shown in Fig. 4.8. This discharge mode, called *fast ignition mode*, is characterized by the initial quasi-stationary discharge inside the initial bubble that can be observed by H_{α} emission in the shadowgraph images.

The impact ionization coefficient can be simply estimated using the following relation:

$$\frac{\alpha}{p} = A \exp\left(-\frac{B}{E/p}\right) \quad [\text{cm}^{-1} \text{Torr}^{-1}], \quad (4.2)$$

where $A = 5 \text{ cm}^{-1} \text{Torr}^{-1}$, $B = 130 \text{ V cm}^{-1} \text{Torr}^{-1}$ within the range of reduced field strength (E/p) 30-500 $\text{V cm}^{-1} \text{Torr}^{-1}$ for hydrogen [90]. Using the measured bubble diameter (d_b) $\sim 7.4 \times 10^{-2} \text{ cm}$ and the electric field strength near the cathode tip calculated from the multi-physics software (Maxwell 3D) $\sim 90 \text{ kV cm}^{-1}$, the electron multiplication factor (αd_b) can be estimated as ~ 90 . Since this value is much larger than the threshold given by Meek's criterion [18], the discharge sustained inside the initial hydrogen bubble can be regarded as the gaseous streamer discharge. This feature partly explains why the additional bubble formation by Joule heating of bulk

water is no longer required. Since a significant amount of energy can be saved by using the fast ignition mode, the preconditioning duration is adjusted for each experimental condition to minimize the pre-breakdown delay as well as the energy loss during this period.

Until the surface protrusion emerges, the bubble discharge lasts for a period of time. Assuming that the lumped resistance of bulk water does not change during this short period of time ($\sim 10\text{-}15\ \mu\text{s}$), the effective channel resistance can be deduced from the measured current-voltage signal. As depicted in Fig. 4.9, the channel resistance defined by additional current path through the bubble discharge is

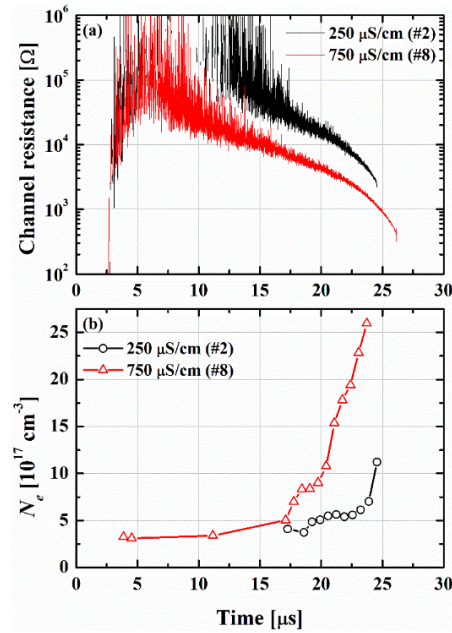


Figure 4.9. Evolutions of (a) the channel resistance and (b) the electron density measured at the channel base. Data are compared for different water conductivity at the same initial charging voltage (V_0) of 20kV.

maintained several orders in magnitudes higher than that of bulk water ($\sim 200\text{-}600\ \Omega$) during the bubble discharge. It indicates that the electrical conductivity of the hydrogen plasma produced by bubble discharge is low, and the leakage current through the bubble surface is negligibly small compared to the current leakage through the rest of bulk water. The time evolution of electron density (n_e) measured near the cathode tip also coincides with this description, since the n_e values do not increase so much until the streamer gets close to the anode. Note that the preconditioning duration (t_{pre}) is set to 200 ms at $250\ \mu\text{S cm}^{-1}$ and 100 ms at $750\ \mu\text{S cm}^{-1}$ condition, respectively.

In fact, bubble discharge can be sustained more stably at higher water conductivity. Figure 4.10 shows an example of the emission spectra and the

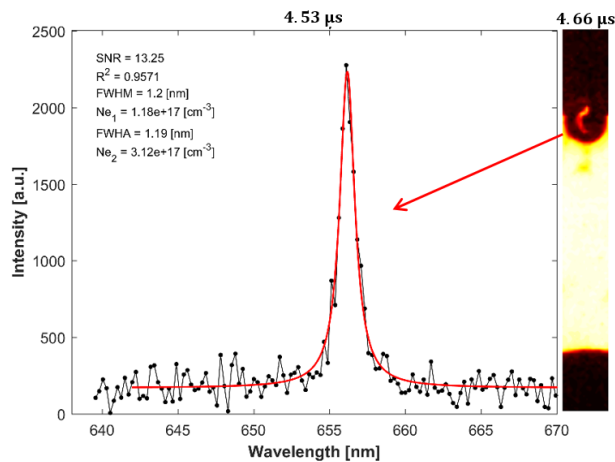


Figure 4.10. An example of emission spectrum acquired from the initial bubble discharge. The discharge is produced at initial voltage (V_0) of 20 kV and water conductivity of $750\ \mu\text{S cm}^{-1}$. A shadowgram is placed on the right-face.

shadowgraph image for the initial bubble discharge. The intensity of H_{α} emission at higher water conductivity is strong enough to determine the electron density even in the very early phase of discharge. That is, the bubble discharge is not only very stable but also has the high n_e values due to the continuous charge removal from the bubble surface at higher conductivity condition. Similarly, according to a series of shadow images, discharge path inside the bubble rapidly moves around because of the local field distortion caused by the charge accumulation. It is interesting that there was no abrupt change in both n_e and the channel resistance at the moment of streamer

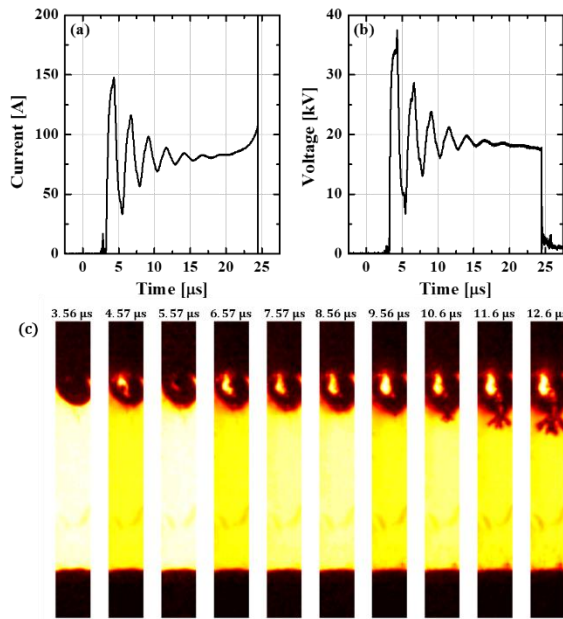


Figure 4.11. Initial bubble discharge under the current-voltage fluctuation induced by a long coaxial cable (93 m): (a) pre-breakdown current, (b) gap voltage, and (c) shadowgraph images. The initial voltage (V_0) is 20 kV and the water conductivity is $750 \mu\text{S cm}^{-1}$.

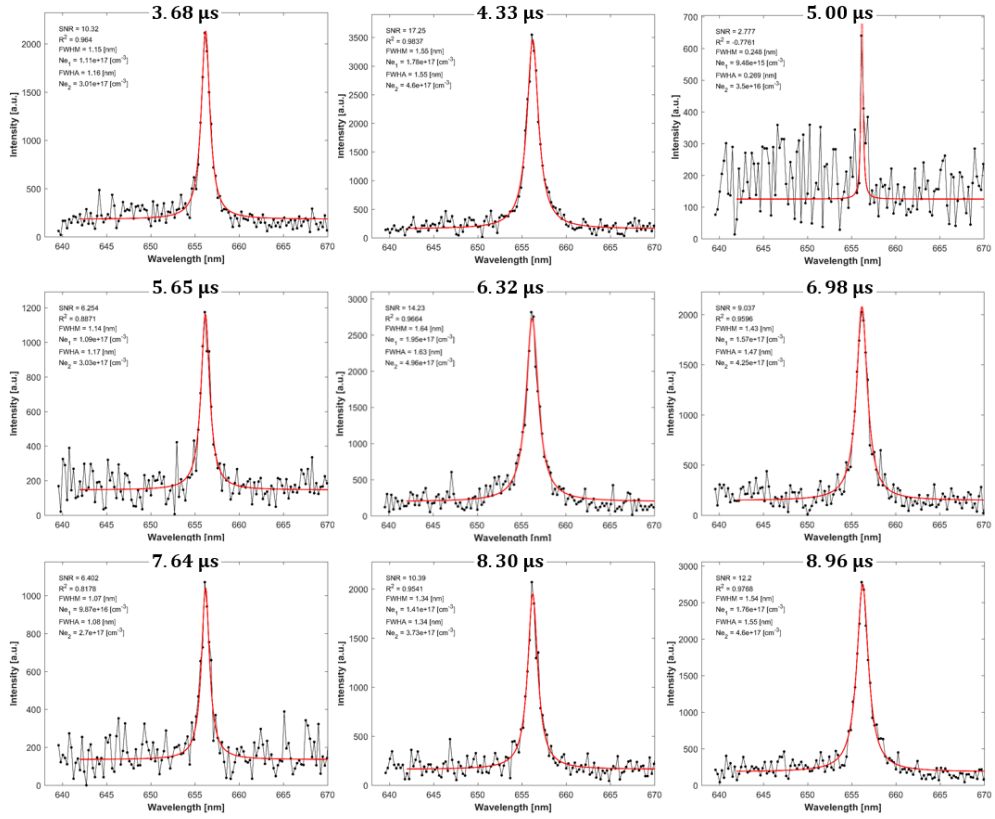


Figure 4.12. A series of emission spectra acquired from the initial bubble discharge under the current-voltage fluctuation. The initial voltage (V_0) is 20 kV and the water conductivity is $750 \mu\text{S cm}^{-1}$.

inception. Hence, it is difficult to say that the initial streamer from the bubble discharge has the high degree of ionization or the high electrical conductivity.

More interesting observation can be made from the initial bubble discharge perturbed by current-voltage fluctuations induced by a long coaxial cable (93 m). The fluctuation of the current and voltage at the load-end is originated from the line

charging effect of the coaxial cable. Since the capacitance of transmission line is proportional to its length, the fluctuation becomes clear when the longer cable is used as shown in Fig. 4.11. Using the 93-long cable, the fluctuation level is high as 100% at first, and is gradually attenuated with time. The fluctuation lasts for about 10 μs , and the bubble discharge flickers as the fluctuation level varies. Here, the interesting point is that the surface protrusion emerged at the end of the fluctuation, so the streamer initiation can be influenced in some way by the fluctuation. Also, with the aid of the OES data presented in Fig. 4.12, it is clearly seen that the blinking of bubble discharge simply indicates the variation of electron density. That is, the higher the fluctuation level, the higher the overall electron density. However, such a high electron density produced by the large fluctuation phase cannot last longer than the fluctuation period ($\sim 5 \mu\text{s}$).

When comparing the pre-breakdown periods with the different cable length as shown in Fig. 4.13, one can identify the influences of the current-voltage fluctuation. The measured n_e values are higher at longer cable case in the early phase, but interestingly, the effective gap resistance remains almost constant during this period. This means that the higher plasma density is achieved by the fluctuating voltage or electric field equivalently rather than the current, since the current released through the bubble discharge is negligibly small. Meanwhile, overall characteristic features for both conditions are very similar to each other including the variations of the channel resistance, pre-breakdown current, and electron density particularly near the

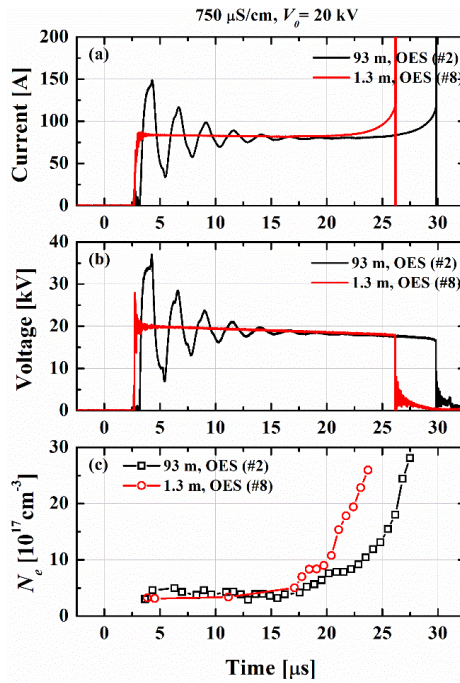


Figure 4.13. Comparison of pre-breakdown processes with different cable length (1.3 and 93 m): (a) pre-breakdown current, (b) gap voltage, and (c) electron density of channel base.

moment of breakdown. That is, the high n_e values in the early phase of bubble discharge guarantee neither the faster streamer propagation nor the different streamer properties at the onset of breakdown. The later stage of streamer propagation is fairly independent of the initial bubble discharge.

As the hydrostatic pressure is increased, a more significant change in the discharge characteristics are exhibited. As shown in Fig. 4.14, it is difficult to visualize the discharge initiation process, because the refractive index of water becomes non-

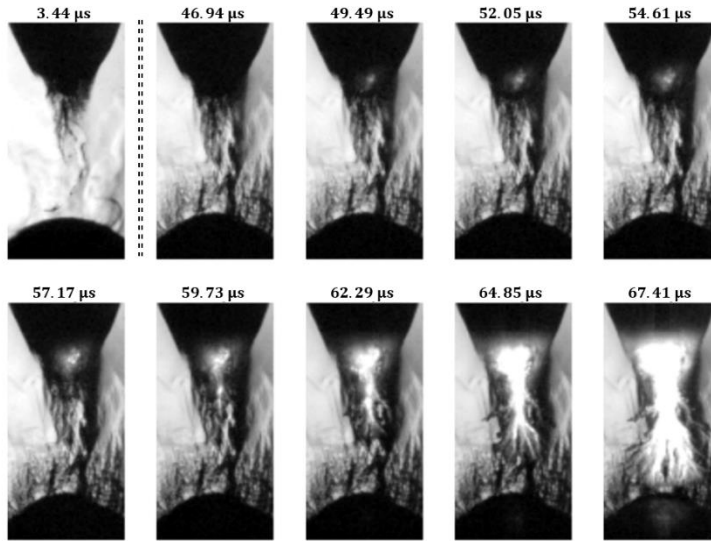


Figure 4.14. Shadowgraph images of PSD with slow ignition mode. The discharge is produced at initial voltage (V_0) of 21 kV, preconditioning duration of 170 ms, water conductivity of $500 \mu\text{S cm}^{-1}$, and hydrostatic pressure of 3 atm.

uniform by Joule heating. Instead, we can expect that the acceleration of the pre-breakdown process in higher pressure condition is similar to that of slow discharge ignition mode. That is, since the size of hydrogen bubbles is not large enough, additional Joule heating will be required to allow the electron multiplication inside the merged vapor bubble. Although still unclear on the images, the bubble discharge is followed by the streamer inception. However, it is evident that the fast discharge ignition mode becomes more difficult to access because of the large diameter bubbles needed to initiate the streamers as the ionization mean free path is reduced at higher hydrostatic pressure.

4.3. Streamer Propagation

Under the same experimental condition including the preconditioning duration, more than one hydrogen bubbles can be formed on the cathode surface. This situation leads to the inception of multiple streamers originated from each individual hydrogen bubble as depicted by Fig. 4.15. The simultaneous initiation of multiple streamer is very rare, but it shows interesting feature about the propagation process of underwater streamer through comparison with the general case (i.e., the single streamer). As mentioned in the previous section, the channel resistance during the pre-breakdown

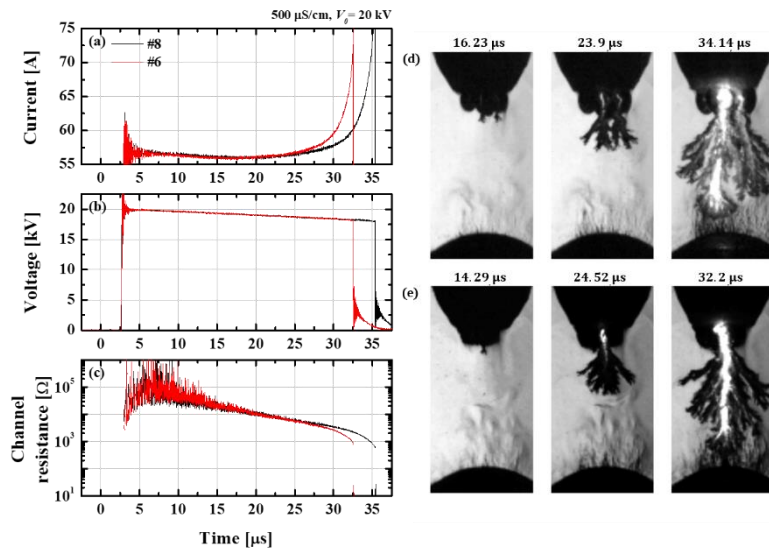


Figure 4.15. Comparison of pre-breakdown processes with the different number of main streamer channel: (a) pre-breakdown current, (b) gap voltage, and (c) channel resistance. Shadowgraph images are correspond to (d) dual (#8) and (e) single (#6) streamer cases, respectively.

period remains very high particularly in the early phase. In the process of streamer inception transformed from the surface protrusion, the early phase of propagation can be understood by a principle of electro-hydrodynamic (EHD) instability [91]. Indeed, since this kind of electrostatic instability is characterized by the charged interface between the gas cavity and the surrounding water, the instability can easily grow by the radial component of electric field [92]. According to the pioneering work of Watson *et al.* [91], the initial phase of streamer propagation can be assumed to be in the inertial limit of EHD instability. In this limit, the growth rate of electrostatic instability is expressed as

$$s_i = k \left[\frac{\epsilon \epsilon_0 E^2}{2\rho} \right]^{1/2}, \quad (4.3)$$

where k is the wavenumber of the instability ($k = 2\pi/\lambda$) and ρ is the density of surrounding liquid. Hence, the electrical conductivity, which is a major factor in determining the electric field strength acting on the charge accumulated on the interface, also plays an essential role in determining the streamer morphology.

From this qualitative picture, initial propagation of streamers for the cases shown in Fig. 4.15 can be described. The current-voltage waveforms are overlapped with each other up to $\sim 25 \mu\text{s}$, so this indicates that the streamer propagation mode is maintained for a while irrespective to the number of streamer channel. In the case of single streamer, the electrical conductivity became sufficiently high due to the concentrated heating on the channel, so more current could flow than in the case of double streamers at the later stage of propagation. Therefore, there is a transition point

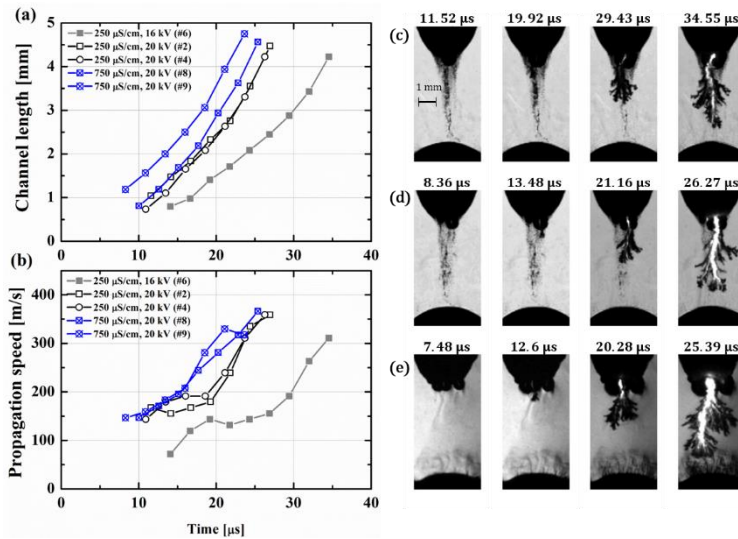


Figure 4.16. Comparison of streamer propagation for different water conductivity (250 and 750 $\mu\text{S cm}^{-1}$): (a) effective channel length and (b) propagation speed. Shadowgraph images are obtained from conditions: (c) 250 $\mu\text{S cm}^{-1}$, 16 kV, (d) 250 $\mu\text{S cm}^{-1}$, 20 kV, and (e) 750 $\mu\text{S cm}^{-1}$, 20 kV, respectively.

that the propagation mode changes from the EHD regime to the Ohmic regime. Here, the Ohmic regime stands for the streamer propagation mode that governed by the current driven through the streamer channel, so the rapid vaporization of water in front of the streamer head takes place. Regarding that the electric field structure around the streamer channel will be determined not only by the channel conductivity but also by its filamentary structure, dynamic evolution of the streamer channel becomes extremely difficult to predict, especially in the subsonic regime.

Despite the complexity of this problem, the propagation characteristics were studied by changing the water conductivity. As the average displacement of streamer

head has been measured from successive shadowgraph images as shown by Fig. 4.16, analysis on the streamer propagation could be simplified. It is expected that the Ohmic current running through the streamer channel is more active at higher water conductivity condition, so less time delay is necessary to raise the channel conductivity. However, lateral expansion due to the radial component of electric field allows more branching, so resulting local field strength get reduced due to the increased effective head radius. On the contrary, the streamers produced at lower water conductivity propagate in EHD regime for a longer period of time due to inactive Ohmic heating in the early phase. This leads to the lower channel conductivity and less lateral expansion and branching. Accordingly, large field enhancement at the streamer head is achieved and the sudden acceleration of streamer channel could be followed.

Figure 4.17 is showing the streamer propagation feature and electron density at the channel base simultaneously, by shifting the recording time with respect to the breakdown delay. In this figure, the sudden increase of the propagation speed can be more easily identified. Indeed, the propagation speed in the earlier phase doesn't change so much, while it rapidly increases as the streamer cross almost half of the gap. If we speculate the potential transfer to the leading part of the streamer using the n_e measured at the channel base, the threshold value for the propagation mode transition can be given as $5-8 \times 10^{17} \text{ cm}^{-3}$. Undoubtedly, for higher water conductivity case, the transition takes place at much earlier time. However, the effect of higher channel

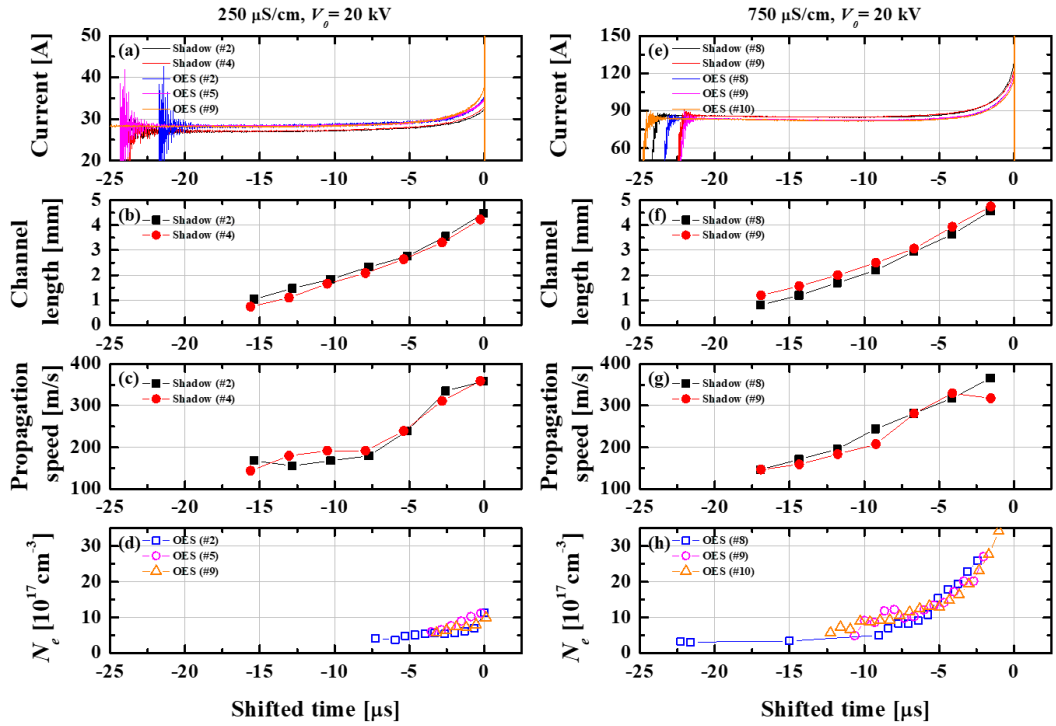


Figure 4.17. Measured parameters during the pre-breakdown period: (a) pre-breakdown current, (b) effective channel length, (c) propagation speed, and (d) electron density at channel base for water conductivity of $250 \mu\text{S cm}^{-1}$, and (e)-(f) for water conductivity of $750 \mu\text{S cm}^{-1}$.

conductivity is compensated by large head radius, so the propagation speed at the final stage becomes almost the same level with the lower water conductivity case. Attempts can be made to capture the propagation mode transition in the current-voltage waveform, but disappointingly, the channel resistance curve does not give such a valuable information (Fig. 4.18).

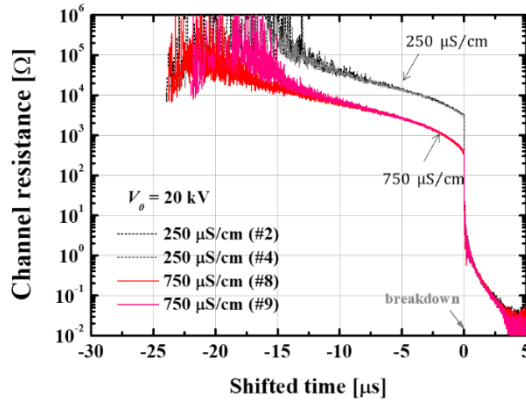


Figure 4.18. Evolution of channel resistance during the streamer propagation for different water conductivity (250 and 750 $\mu\text{S cm}^{-1}$).

The EHD mechanism in the early phase of streamer propagation has been confirmed by exposing the streamer to the voltage fluctuation induced by the long coaxial cable (93 m). Since the level of voltage fluctuation increases as the load impedance is raised, discharge has been produced with $500 \mu\text{S cm}^{-1}$ water. The half-period of voltage fluctuation was about $2 \mu\text{s}$, so the inter-frame interval for the shadowgraph imaging has been adjusted to $1 \mu\text{s}$ by reducing the activated pixels. In the presence of voltage fluctuations, it sometimes happens that the streamers are initiated from the bubble surface in the middle of fluctuation, as presented in Fig. 4.19. Sampling those interesting cases to compare with the usual case (Fig. 4.20(c)), it has been revealed that the early phase propagation of streamers is perturbed by the large voltage fluctuation. In fact, the voltage fluctuation level plays an essential role to accelerate the streamers in the cathode vicinity because the EHD mechanism must be driven by

the base electric field formed in the water gap. That is, in the early phase, the electrical conductivity of streamer channel is too low to distort the base electric field. Accordingly, once pushed out of the bubble surface near the cathode region, the propagation speed recovers to the original level. It should be noted that the initial perturbation in the propagation speed is not synchronized with the voltage fluctuations as the EHD mechanism works in the inertial limit. This perturbation can be observed

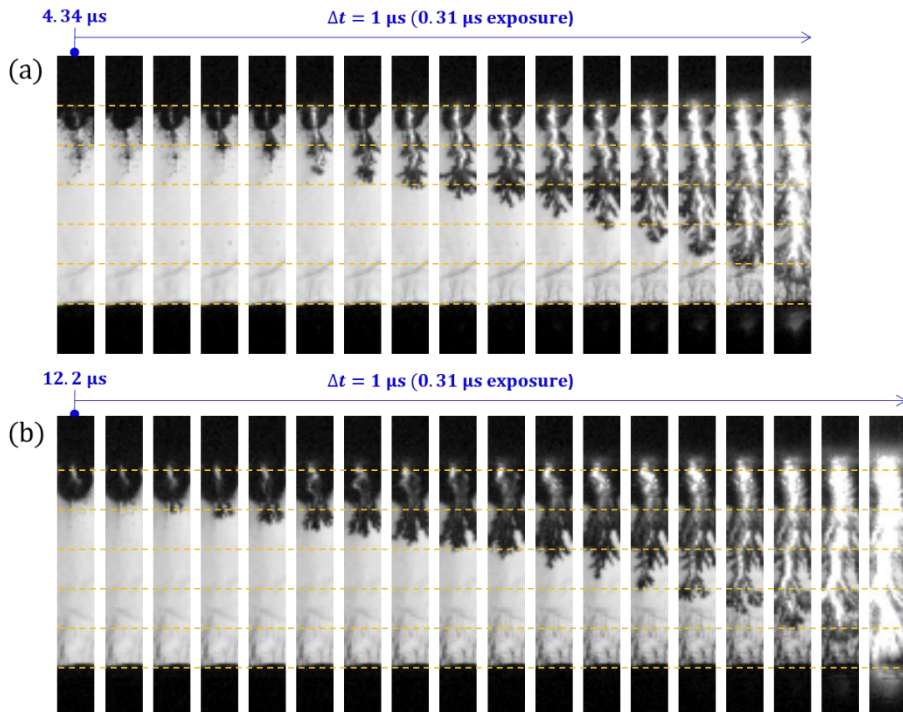


Figure 4.19. Shadowgraph images of streamer propagation in the presence of fluctuating current-voltage induced by long coaxial cable (93 m). The images are acquired from different shot: (a) #1, (b) #8, where the water conductivity is $500 \mu\text{S cm}^{-1}$ and initial charging voltage is 20 kV.

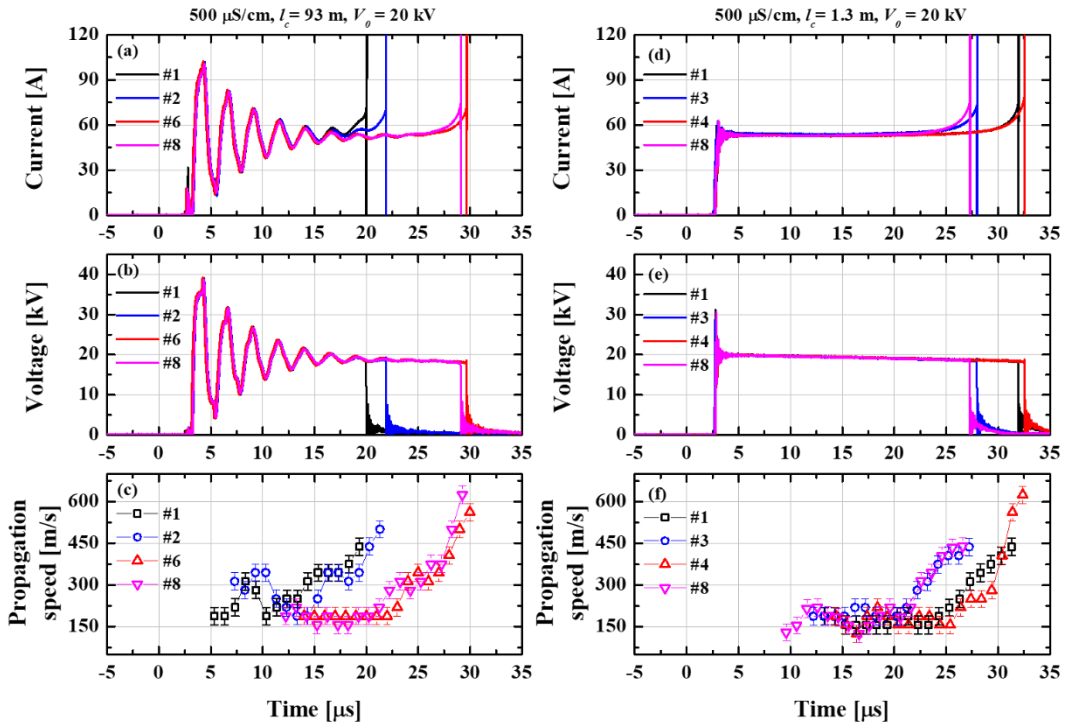


Figure 4.20. Comparison of streamer propagation at different cable length: (a) pre-breakdown current, (b) gap voltage, and (c) propagation speed for 93 m-long cable, and (d)-(f) for 1.3 m-long cable.

only in the presence of high level of voltage fluctuation, so the propagation characteristics for the case where the streamer is initiated slightly later are very similar to those in the absence of fluctuation. Hence, regarding the pre-breakdown process, the line charging effect induced by the long coaxial cable is negligible in most cases.

Streamer propagation in higher hydrostatic pressure needs to be discussed more cautiously. As already mentioned in the previous section, both the bubble

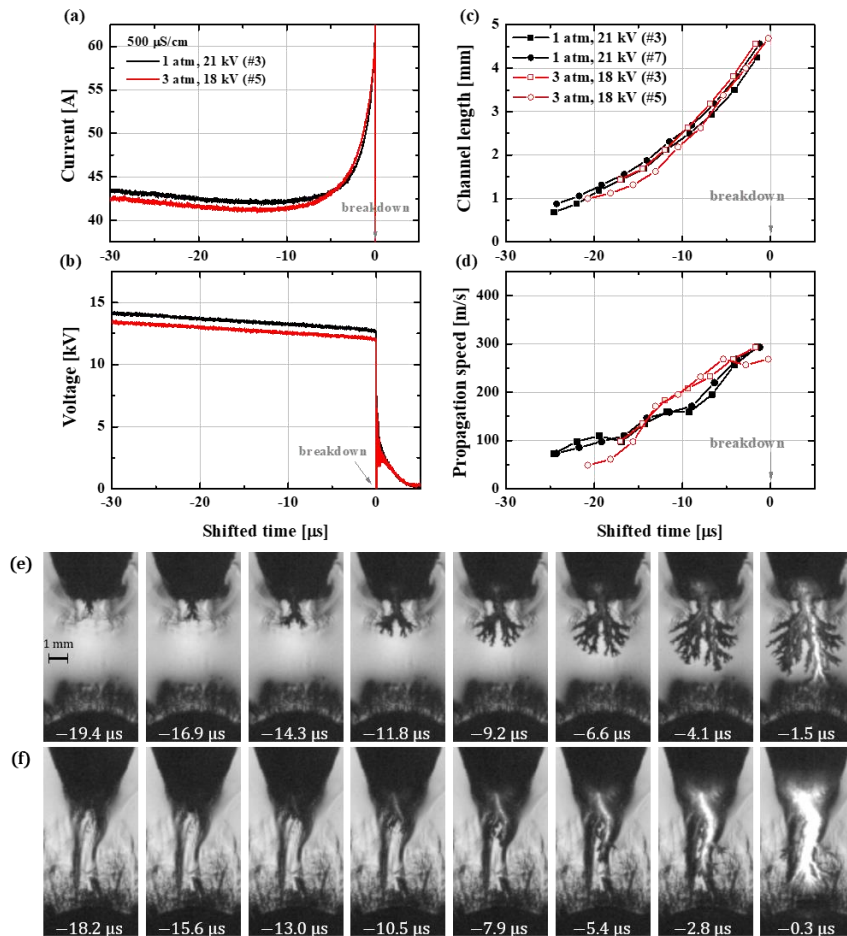


Figure 4.21. Streamer propagation at 1 and 3 atm condition: (a) pre-breakdown current, (b) gap voltage, (c) effective channel length, and (d) propagation speed. Shadowgraph images of discharge in slow ignition mode under conditions (e) preconditioning duration of 70 ms at 1 atm and initial voltage of 21 kV and (f) preconditioning duration of 170 ms at 3 atm and initial voltage of 18 kV.

discharge and the streamer inception process are unclear in this case because the refractive index of water becomes non-uniform due to the Joule heating on the bulk

water. For the same reason, the streamer propagation is also difficult to clearly visualize, as shown in Fig. 4.21. Here, the discharges have been produced in the slow ignition mode due to limited access to the fast mode at higher pressure condition. Both the preconditioning durations and the initial charging voltage have been adjusted to obtain data having the similar level of breakdown voltage (V_{bd}) for the comparison. If we focus on the breakdown moment, only slight difference can be identified in the current-voltage waveforms. At higher pressure condition, the current released through the streamer channel increases more rapidly in virtue of its thicker stalk. In fact, the n_e measured at the channel base (Fig. 4.22(a)) also indicates that the streamer channel produced at higher pressure condition has higher channel conductivity in the later phase of streamer propagation. The time evolution of channel resistance is supporting this description. However, considering that the measured displacement of streamer head from the shadowgraph images is not precise enough, it is difficult to discuss the

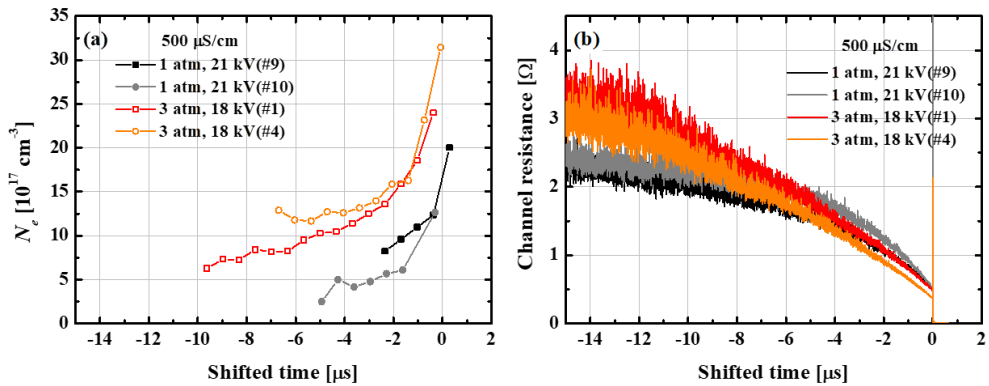


Figure 4.22. Evolution of (a) electron density measured at channel base and (b) channel resistance. Discharge conditions are the same as data presented in Fig. 4.21.

propagation characteristics where the discharge has been produced in the slow ignition mode. Hence, it cannot be determined whether the same threshold n_e value can be applied to these cases either. From these reasons, further investigations are necessary on the complicated mechanisms of initiation and propagation process of negative streamers in the case of slow ignition mode for more thorough understanding.

4.4. Streamer-to-arc Transition

Once the negative streamers crosses the water gap, the spark channel is instantaneously formed from the streamers. According to the data presented in Fig. 4.23 and 4.24, the channel impedance rapidly changes by two orders in magnitude within a few nanoseconds, and the subsequent transition to the arc state is a slower process taking longer than 2 μ s. Since the formative process of spark channel from the negative streamers could not be resolved with the experimental devices using in the present work, we have focused on the streamer-to-arc transition period instead. That is, the noticeable difference in the streamer-to-arc transition process under the same breakdown voltage (V_{bd}) can be estimated as a consequence of the initial spark channel properties. From this respect, one can discuss the influences of the water conductivity and hydrostatic pressure with the data presented in Fig. 4.23. It is interesting to note that the streamer-to-arc transition process is almost identical given the structure and electron density of the streamer properties are significantly affected

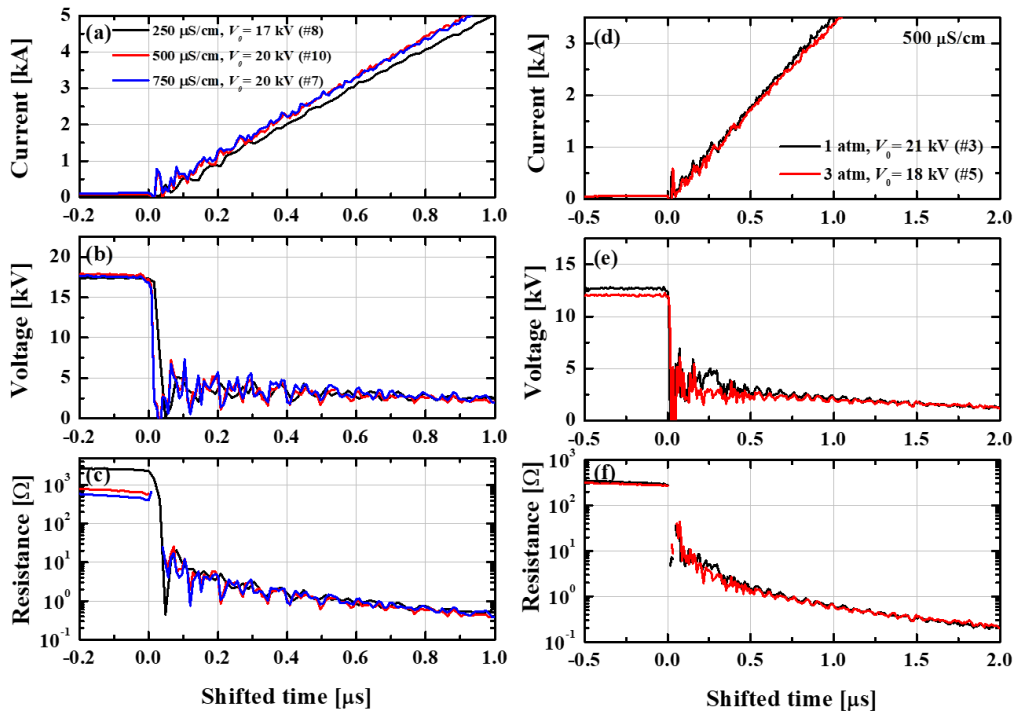


Figure 4.23. Electrical measurements on the streamer-to-arc transition: (a) current, (b) gap voltage, and (c) channel resistance for different water conductivities, and (d)-(f) for different hydrostatic pressures.

by the water conductivity. This feature was observed very similarly in the case of different hydrostatic pressure. From these experimental results, it has been revealed that at least the level of experimental conditions changed in the present work cannot cause a noticeable variation in the streamer-to-arc transition process. On the other hand, unlike the case where only the characteristics of the initial streamer were changed, a significant difference has been observed in the experiment in which the Joule heating was controlled during the transition period, as depicted in Fig. 4.24. It

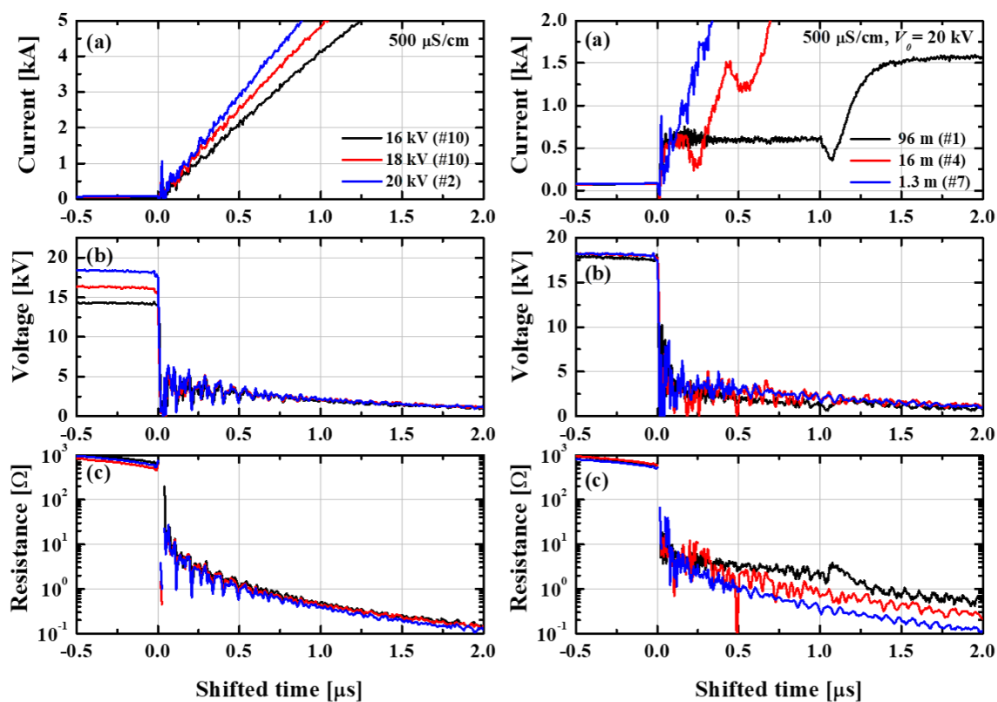


Figure 4.24. Electrical measurements on the streamer-to-arc transition: (a) current, (b) gap voltage, and (c) channel resistance for different breakdown voltages, and (d)-(f) for different cable lengths.

is difficult to clearly distinguish the effect in the case of different breakdown voltage (Fig.4.24 (a)-(c)) because the differences among the channel resistances is not so larger than the noise level, but the effect is very clear in the case where the Joule heating is controlled by the length of the coaxial cable (Fig.4.24 (d)-(f)). Apparently, the pulse forming action operates with the sufficiently long time step of $\sim 1 \mu\text{s}$ at 93 m-long cable, thus the channel resistance has been decreased much slowly as the Joule heating is effectively limited by cable. Indeed, this experiment gives us quite

interesting insights because we have already found out that the properties of negative streamer near the breakdown time are almost independent of the cable length. That is, using this experimental technique, the streamer-to-arc transition process under the same (or, at least very similar) initial spark plasma condition can be investigated.

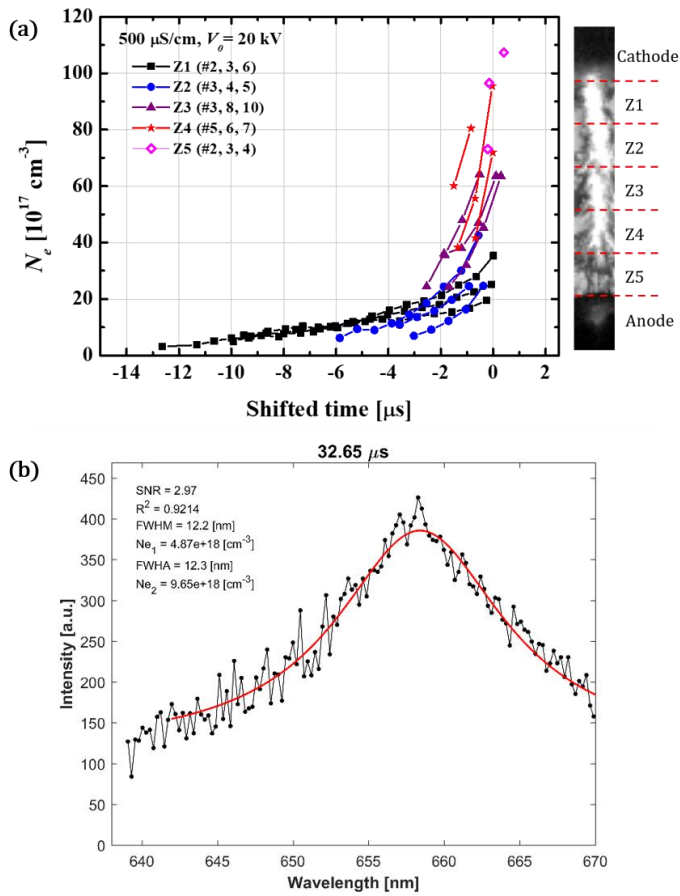


Figure 4.25. (a) Electron density measured at different vertical position of discharge channel and (b) example of H_α line spectrum acquired at Z5 position marked in the shadowgram.

Attempting to determine the initial condition of spark plasma that is almost instantaneously formed from the streamer channel, the evolution of electron density (n_e) has been measured at five different vertical positions (Fig 4.25(a)). Considering that this measurement is aimed at measurement of high n_e near the breakdown point, compared to the cathode region where the n_e value gradually increases from the relatively low level, the initial value as well as the increasing rate is much higher at the anode region. In fact, the electron density (n_e) at anode region was so high ($\sim 10^{19} \text{ cm}^{-3}$) that the four-fold variation of n_e was measured along the channel length. This feature is fairly consistent with the description on the later phase of streamer propagation (i.e., Ohmic regime), thus the local electric field near the head region is strong enough to cause the avalanche-streamer transition even at higher density condition of water vapor. The emission spectra corresponds to the head region in the anode vicinity (Fig. 4.25(b)) contains the strong continuum emission and shows large broadening of. The emission spectra corresponding to the head region in the anode vicinity (Fig. 4.25(b)) not only shows large broadening of H_α line but also contains the strong continuum emission. This partly indicates both the high density and the strong electric field at this position in the presence of the strong Stark broadening and the ionization potential lowering [61, 65].

In order to utilize experimental results to estimate the initial spark plasma condition, the procedure given in section 3.1.2 can be followed. Although it is unfortunate that the diagnostics on the plasma for a later period including the

streamer-to-arc transition is almost impossible so far, numerical model will cover many issues that cannot be explained experimentally. It should be noted that we have focused on the case of fast discharge ignition mode in the experimental observations on the negative subsonic streamers, since this mode is very beneficial for studying the characteristics of them. Although analysis given in the present work is simplified to some extent, the salient features of negative subsonic streamers could be effectively captured. In particular, the clear observation on the evolution of streamers in the very early phase of propagation gives valuable information on their propagation mechanism which changes from EHD to Ohmic regime. Moreover, uncertainties arising from the bubble formation stage has been remarkably reduced, so it is able to control the PSD process very accurately. Hence, in the following chapter, the experimental results acquired from the fast ignition mode will be mainly used for the discussion of shock wave formation process during the streamer-to-arc transition period.

Chapter 5. Development of Underwater Shock Wave by Pulsed Spark Discharge

In this chapter, we present the characteristics of rapidly expanding spark plasma and subsequent shock wave formation after the electrical breakdown occurs in the underwater PSD. Here, the self-consistent simulation model has been used extensively to describe the experimental results measured in the streamer-to-arc transition period.

5.1. Shock Wave Formation via Streamer-to-arc Transition

When the negative streamer touches the anode, the electrical breakdown occurs. From this moment, the spark channel is almost instantaneously (< 10 ns) transformed from the streamer, and the current flowing through the spark plasma rapidly rises. The damping factor of the capacitive circuit is determined by circuit parameters as

$$\zeta = \frac{R_{sys}\sqrt{L_{sys}C_{sys}}}{2L_{sys}}, \quad (5.1)$$

where $R_{sys}, C_{sys}, L_{sys}$ are the system resistance, capacitance, and inductance, respectively. Based on the values given in Table 3.1, the system becomes the underdamping state ($\zeta < 1$) when the load resistance is lower than 3.5Ω . Since the electrical conductivity of spark plasma determines the electrical power delivered to

the spark channel by Ohmic heating, its thermodynamic state is closely related to the electrical property. Besides, the electrical conductivity also can be described as a function of thermophysical properties such as mass density (ρ) and temperature (T), i.e., in the form of $\sigma(\rho, T)$, thus the dynamic evolution of the spark plasma should be described in a self-consistent manner. In this section, our interest is mainly focused on the formation of shock wave in the surrounding water region. The intensity of the underwater shock wave not only indirectly shows the variation of the thermodynamic characteristic of the spark plasma but also has an important meaning as a representative parameter showing the efficiency of the electrical energy converted into the hydraulic motion in the application aspect. Here, we present the experimental results associated with the streamer-to-arc transition and the subsequent formation of shock wave. Also, the detailed description on the hydrodynamic phenomena will be given with the advanced self-consistent model that is introduced in chapter 3.

5.1.1. Experimental Observations

Along with many references [37-43], we have reported the dependency of pressure wave intensity on the various experimental parameters, such as the storage capacitance (C_0), breakdown voltage (V_{bd}), hydrostatic pressure (p_{hs}), and cable length (l_C) [16, 36, 41]. However, all the previous experimental approaches have a common limitation that the progress of the pre-breakdown process varies greatly

depending on the discharge condition, so it was unable to control the initial state of the spark channel. In contrast, the experimental technique proposed by the present work, effectively handles this issue by minimizing the uncertainty originated mainly from the bubble formation stage.

Figure 5.1 shows the influence of the water conductivity, hydrostatic pressure, and cable length on the peak pressure value measured at 10 cm away from

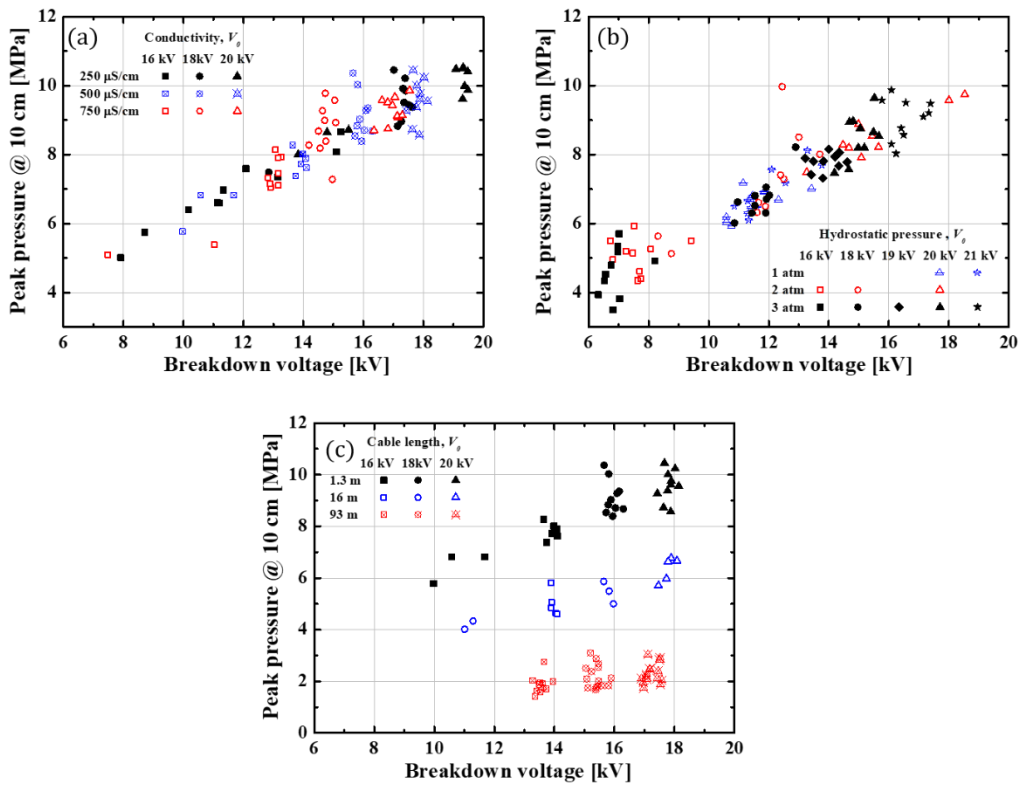


Figure 5.1. Variation of measured peak pressure with respect to the breakdown voltage for different (a) water conductivity, (b) hydrostatic pressure, and (c) cable length.

the water gap. Recalling from Sec. 4.4, no significant difference has been observed in the electrical measurement during the streamer-to-arc transition by variations of the water conductivity and hydrostatic pressure, whereas the effects of higher breakdown voltage and pulse forming action were present. Hence, the distribution of peak pressure values shown in Fig. 5.1 can be understood as a direct consequence of the streamer-to-arc transition process, or the effective power deposition into the spark channel, equivalently. That is, it can be confirmed once again that the increasing rate of the measured peak pressure due to the increase of V_{bd} is insensitive to the water conductivity and hydrostatic pressure conditions. To be more precise, in these cases, the degree of dispersion of the data is greater than the effect of changing those parameters, so they cannot be separately discussed. It is interesting that the linear dependence of the peak pressure on V_{bd} (~ 0.51 MPa/kV) holds in a quite wide range of operating condition with the shortest cable (1.3 m). Meanwhile, the distribution of peak pressures tends to strongly depend on the length of coaxial cable. Considering that the initial parameters of the spark plasma are practically independent on the cable length, it can be deduced that the change in the peak pressure mostly arises from the streamer-to-arc transition process. When the cable gets longer, not only the shock wave intensity is remarkably weakened but also the rate of increase with respect to V_{bd} is reduced. Indeed, the reduction in peak pressure is up to $\sim 70\%$, which is much larger than we expected. Recalling that the reduction in peak pressure is expected to be around 20% even at $l_c = 125$ m in the numerical results obtained

under the assumption of the uniform profile of plasma parameters (Sec. 3.2), this experimental result cannot be explained at all. Hence, because the positive streamers have been mainly studied in the previous works, it is worth investigating the effect of the radial structure of the spark plasma on the shock wave formation in the negative subsonic discharge regime. In this regard, while the OES technique which has been

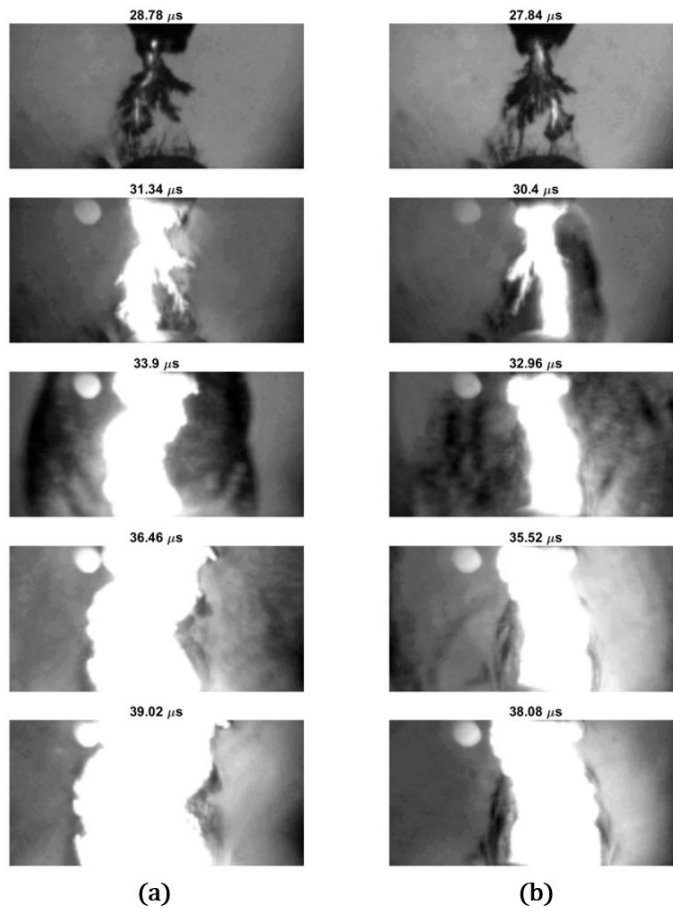


Figure 5.2. Shadowgraph images of the spark channel and shock wave. Images are acquired from different cable lengths: (a) 1.3 m, (b) 93 m. The breakdown delays are 30.9 and 29.6 μs , respectively.

applied to characterize the bubble discharge as well as the negative streamers is no longer applicable in the breakdown period, the experimental efforts have been focused to visualize the structure of spark plasma channel.

As described in Sec. 2.3, the optical components have been adjusted because of strong emission from the channel surface. In particular, the circular cut-off that is interposed between the focusing lens and the second field lens requires subtle adjustment in order to achieve the high quality of images. Otherwise, the entire image becomes completely saturated or the dynamic range becomes too narrow to distinguish imaging objects. Here, the initial heating on the spark channel has been limited by the pulse forming action of longer coaxial cable. Figure 5.2 shows a series of shadowgraph images obtained from the PSD with the different cable length ((a) 1.3 m and (b) 93 m). At the wide field-of-view (FOV) setting with the 128x8 pixel resolution, the maximum frame rate is limited to 390,804 fps, and the overall structure of the spark channel and the shock wave front could be visualized. Although only a few images contain the shock wave structure, we have confirmed that the radial positions of the channel surface and the shock front can be accurately identified. In addition, the external shape of spark channel indicated by the bright emission boundary in the image can be roughly approximated to the cylindrical shape in the early phase of transition.

Based on the above observations, the shadowgraph images focused on the mid-point of the spark channel have been obtained at the maximum frame-rate of

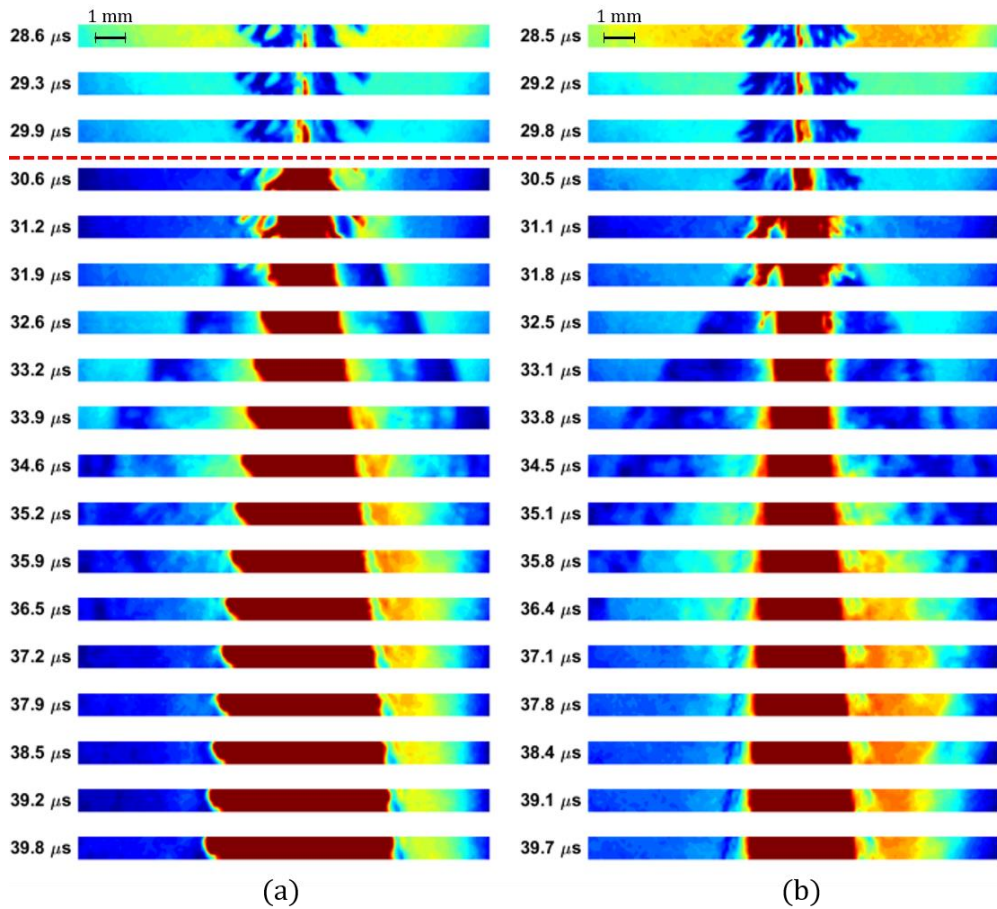


Figure 5.3. Shadowgraph images processed to measure the time-varying channel radius and shock position for different cable lengths: (a) 1.3 m and (b) 93m. Discharges are produced at water conductivity of $500 \mu\text{S cm}^{-1}$ and initial charging voltage of 20 kV. Dashed line indicates the breakdown moment.

1,511,111 fps, and the exposure time of $0.31 \mu\text{s}$, as shown in Fig. 5.3. The image intensity has been converted to a color map by image processing performed using MATLAB®. Starting from the breakdown moment indicated by the red dashed line,

it is possible to observe very clearly the process of the streamer-to-arc transition. During the breakdown period, the spark channel indicated by red color (i.e., bright pixels) rapidly expands and the shock wave front indicated by blue color (i.e., dark pixel) propagates radially outward. Here, if we assume the light emitting area in the imaged before the breakdown time as the highly conductive part in the streamer, we can catch the slight difference in the radial structure of spark channels shown by (a) and (b) in the figure. That is, this light emitting part of streamer, namely the conductive core, expands much slowly in longer cable case after the breakdown takes place. Although, we cannot accurately deduce the radial current density profile from the self-emission image, it is still possible to estimate the radial profile of the temperature, or the electrical conductivity equivalently, from the image of 30.5 μs in Fig. 5.3(b). Before the breakdown, the core radius was measured as 180 and 155 μm in (a) and (b), respectively. On the other hand, the outer channel radius distinguished as the region of lower brightness in (b) was measured at about 350 μm . That is, the initial spark channel just formed from the streamer has a highly conductive core region, and there is a less conductive outer layer covering it. The structure of the negative streamer, i.e., the plasma filament surrounded by the gas shell, has been already mentioned in other literatures [3, 6, 11], but our experimental result suggests that the radial structure may have an important role in the streamer-to-arc transition.

Experimental results focused on the streamer-to-arc transition period can be presented altogether as shown in Fig. 5.4. The channel radius and the position of shock

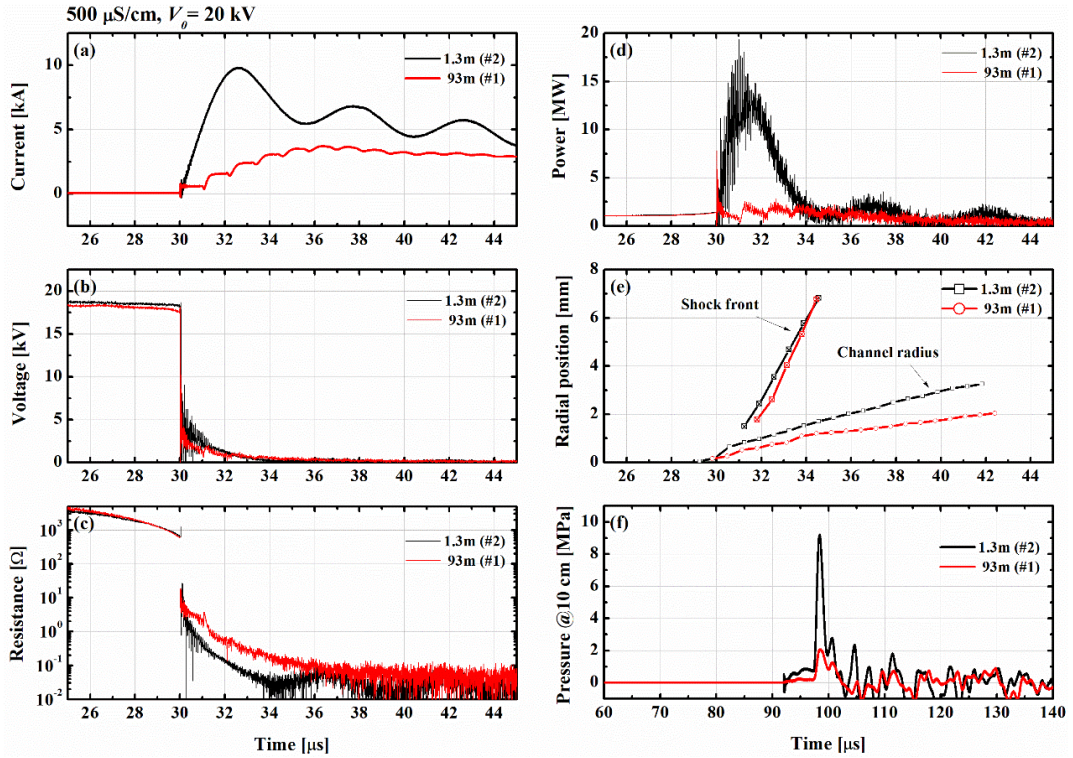


Figure 5.4. Measured parameters during the streamer-to-arc transition for different cable lengths: (a) breakdown current, (b) gap voltage, (c) channel resistance, (d) delivered power, (e) channel radius and shock position, and (f) pressure waveform measured at 10 cm away from the water gap.

front are measured from the images given in Fig 5.3, and corresponding data from the electrical measurements are compared at the same time-frame. In the analysis, the luminous part of the channel is estimated as the spark channel, so the sudden jump of the channel radius has been observed because the initially dark outer layer rapidly became luminous. Also, the resistance curve in (c) is calculated to represent the

channel resistance, so it is assumed that the resistance of water gap does not change. For the data set acquired from different cable length (1.3 and 93 m), the breakdown delay times derived from the inflection point of the resistance curve are 30.05 and 30.01 μs , respectively. In the case of 93 m cable, the stepwise variation of arc current is the direct consequence of the pulse forming action of coaxial cable, and it dominates the actual transition process. That is, the delivered power (in (d)) limited by the coaxial cable makes the channel resistance (in(c)) decrease more slowly. Apparently, this results in the slower expansion of spark channel and the much weaker pressure wave intensity. The parameters presented in the figure are actually the most important ones to interpreting the progress of the transition, thus they are used to confirm the validity of numerical results in subsequent sections.

Before discussing the formative process of underwater shock, the relation between the shock wave structure and the response of the pressure sensor has been examined. As shown in Fig. 5.5, the pressure wave produced by PSD has a rather complicated shape. Images are sampled to show the spark channel and the shock wave simultaneously, and the outline of electrode tips are drawn with the orange solid lines. In the case of a strong pressure wave in short cable cases, the shock front was clearly observed, and one or more shock fronts were overlapped depending on the channel shape. On the contrary, the pressure wave produced in long cable cases is observed in a spatially dispersed form having an unclear front. In fact, this feature is already shown in Fig. 5.3(b) with the broad band of wave front, which is distinguished by the second

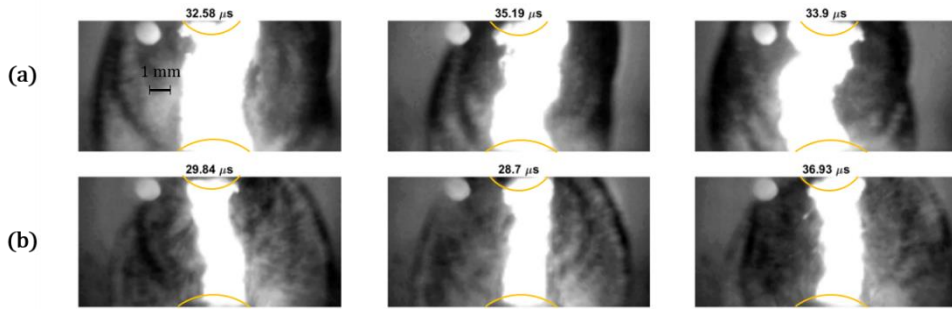


Figure 5.5. Shadowgraph images showing the structure of underwater shock waves produced at different cable lengths: (a) 1.3 m and (b) 93 m. The water conductivity is $500 \mu\text{S cm}^{-1}$ and the initial voltage is 20 kV.

derivative of the refractive index ($\partial^2 n / \partial r^2$). The spatially distributed shock front indicates that the radial expansion of the spark channel is nonlinear in time. Similarly, this feature may contribute to the pressure sensor response having the second peak which is comparable to the first one in the case of 93 m-long cable in Fig. 5.4(f). However, there also exist smaller oscillatory peaks in the decaying part of pressure waveform in the case of 1.3 m-long cable in the same figure, so it looks difficult to impose any physical meaning on the entire pressure sensor signal so far. In other words, it is possible that pressure sensor signals are distorted during the measurement process to some extent.

In order to confirm the response characteristics of the pressure sensor influenced by the shock wave structure, the underwater shock wave has been produced

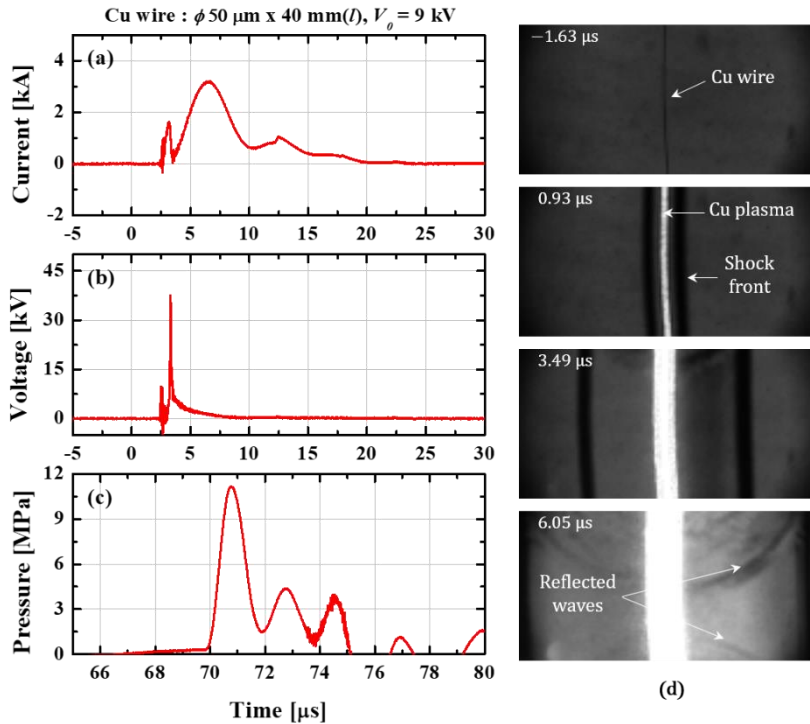


Figure 5.6. Measured waveform from the underwater electrical wire explosion: (a) discharge current, (b) voltage, (c) pressure, and (d) shadowgraph images. The dimension of Cu wire and initial voltage are marked on the top of figure.

by using the wire load instead of the water gap. In fact, the underwater electrical wire explosion is a very stable source of highly uniform cylindrical pressure wave as shown in Fig. 5.6(d). The measured peak pressure value at wire load was 11.5 MPa, similar to the short cable case shown in Fig. 5.4(f). However, in the discharge of metal wire, the smaller oscillatory peaks were measured again at the decaying period of the pressure waveform, even though the main shock wave having the single layered

structure was produced from the phase explosion which can be identified by the voltage spike [93] in Fig. 5.6(b). Hence, it is fairly confirmed that the following peaks other than the first one in the signal of pressure sensor cannot be trusted unless there is an additional signal processing. This issue associated with the nonlinear response of the piezoelectric pressure probe has been investigated by Grinenko *et al.* [94]. They focused on the gain deficit of the ICP type pressure sensor in high frequency range (>1 MHz), and demonstrated that the real pressure wave could be reproduced from the measured pulse using the frequency-dependent response function and the constraint of the energy conservation. However, there is a limitation that the priori information on the input pulse waveform is required in order to apply the energy conservation condition. It is also pointed out that the self-resonance of the gauge has a combined effect with the impedance mismatch at the crystal plane facing the water (i.e., the ambient medium), creating one or more resonance peaks [94]. From these reasons, the reconstruction of true pressure waveform is placed beyond the scope of this study, and only the first peak value is used in the following discussions.

5.1.2. Role of Outer Shell

Based on the fine shadowgraph image (Fig. 5.3) of the initial plasma structure which is composed of the highly conductive core and less conductive shell, it is able to model this structure by imposing the low initial temperature to the shell region. As already described in Sec. 3.1.2, the strong dependence of electrical conductivity (σ) on

temperature (T) for $T \leq 10^4$ K enables us to obtain the center peaked σ profile, as shown by Fig. 3.6. The model parameters for the initial spark channel can be given for the cases of Gaussian-like and uniform temperature profile as below:

- Gaussian-like: $r_0 = 350 \mu\text{m}$, $T_{c,0} = 15 \text{ kK}$, $T_{s,0} = 3 \text{ kK}$,
- Uniform: $r_0 = 150 \mu\text{m}$, $T_0 = 15 \text{ kK}$,

where r_0 is the outer channel radius and subscript c and e are for the core and shell, respectively. In both cases, the mass density ratio (δ_0) of 2×10^{-3} and the empirical correction factor (k_σ) of 0.1 for the electrical conductivity have been equally applied. The effective radius in the conductivity profile for the case of Gaussian-like temperature profile assumed here can be approximated as $\sim 150 \mu\text{m}$. Hence, the comparison with the case of uniform temperature profile with the initial radius of $150 \mu\text{m}$ reasonably illustrates the influence of cold shell on the streamer-to-arc transition. In this regard, Figure 5.7 shows numerical results of (a) the channel resistance, (b) delivered power, and (c) channel radius calculated using different initial plasma structures (i.e., core-shell and uniform). For the parameters shown in (a) and (b) of Fig. 5.7, the influence of the outer cold layer cannot be clearly distinguished. The channel radius (in (c)) also exhibits negligible difference in the early phase, while slightly faster expansion is observed in the later phase of expansion in the case of Gaussian-like profile. On the other hand, this figure shows a significant change depending on how the radiation loss term is treated in the energy balance equation. One extreme gives the maximum radiative power loss under the assumption of

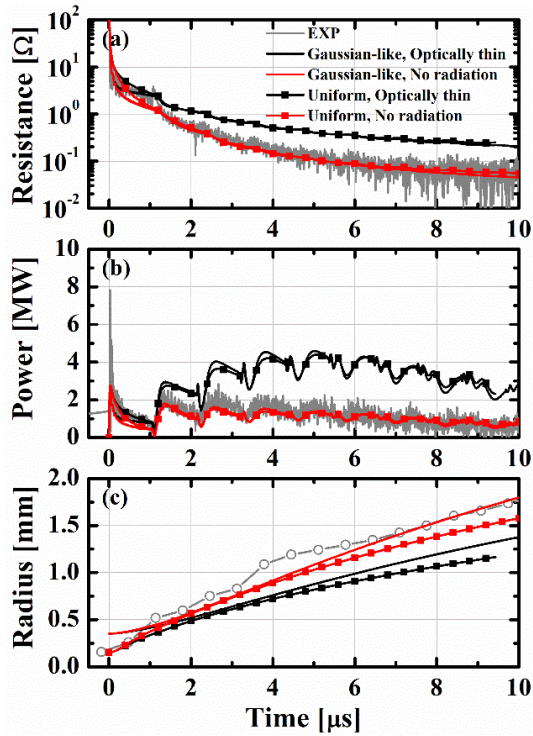


Figure 5.7. Comparison of numerical results based on different initial temperature profile of spark plasma and experimental results: (a) channel resistance, (b) delivered power, and (c) channel radius.

optically thin plasma for the entire plasma volume. The other extreme is given by ignoring radiative power loss. Accordingly, the reality is expected to be located between these extremes. Measured channel resistance (in (a)) initially follows the numerical results of optically thin case for $\sim 1 \mu\text{s}$, and gets close to the curve in the absence of radiation loss later. In the case of optically thin plasma assumption, the channel resistance decreases much slowly, so the delivered power tends to be over-

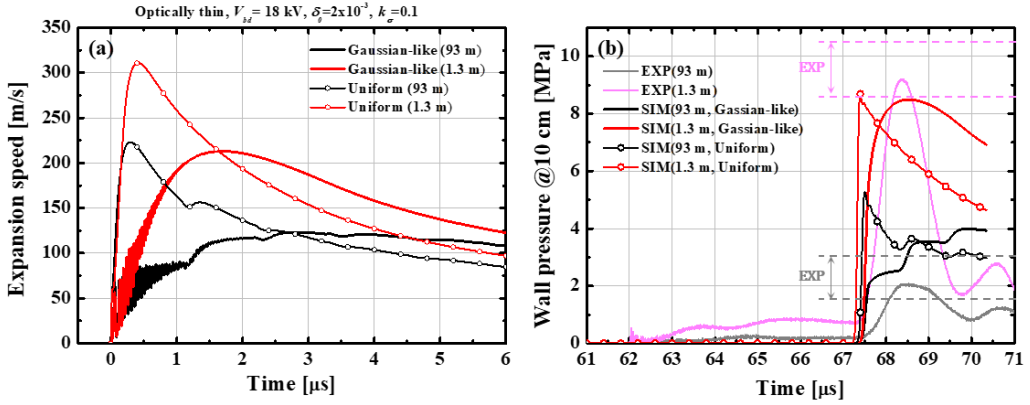


Figure 5.8. Comparison of numerical results based on different initial temperature profile of spark plasma and experimental results: (a) the expansion speed of spark channel and (b) the pressure at probing position (10 cm).

estimated. Nonetheless, the channel expands much slowly in the case of optically thin case because there is an excessive power loss by thermal radiation.

Focusing on the early phase of transition, that mostly determines the properties of shock front, hydrodynamic features with the optically thin plasma assumption are presented as shown in Fig. 5.8. Here, we compared the numerical results with different cable length (1.3 and 93 m) to confirm the influence of initial channel structure. Unlike the electrical signals which mostly overlap with each other, it is possible to recognize the clear difference in the evolution of channel expansion and subsequent pressure wave build-up. Indeed, the expansion speed based on the core-shell structure increases much slowly, and contains high frequency fluctuations that probably came from the multiple internal reflections of pressure wave inside the

spark channel. Moreover, in the case of 93 m-long cable exhibits the step-wise variation of the expansion speed which is originated from the pulse forming action of the coaxial cable. Meanwhile, in the case of uniform initial condition, the expansion speed rapidly increases as soon as the transition begins, and reaches the maximum point within a few hundred nanoseconds. The simulated pressure waveforms are showing such behaviors of spark channel at each condition. Apparently, the influence of initial plasma structure largely appears in the simulated pressure waveforms for longer cable (93 m) cases. In the presence of the outer shell, the step-wise variation of expansion speed leads to similar trend of pressure waveform with low intensity of the first shock front, whereas much sharper and larger spike emerges in the uniform profile case. This feature is mainly attributed to the damping action of outer shell that surrounds the conductive core. That is, the outward delivery of core pressure is delayed as the outer cold layer plays as a shock absorber. Similarly, the rising rate of pressure waveform is slightly delayed by considering the outer shell in the case of shorter cable (1.3 m), but the peak intensities are in a comparable level irrespective to the initial plasma structure. It should be noted that the measured pressure waveforms using 1.3 and 93 m-long cables could be adequately explained with the numerical results in the presence of outer shell. Although, in the numerical result, the second and third pressure waves have higher intensity than the first one, we cannot compare them with measured data except for the first shock front. Hence, considering the dispersion of measured peak pressure (indicated by the dashed line in the figure), the numerical

results with uniform initial structure significantly overestimate the pressure wave intensity.

The radial profiles of cylindrical pressure wave calculated from the numerical model for longer cable case can be shown as Fig. 5.9. Assumed the initially uniform plasma, the internal pressure of spark channel suddenly jumps to ~ 220 MPa, which appears to be caused by instantaneous peaking of heating immediately after the breakdown. In fact, it can be understood that such a high internal pressure has induced the serious overestimation of the pressure waveform. On the other hand, the pressure profile in the presence of cold shell shows the stepwise spatial distribution, and there found the interval (Δr_{sf}) between the successive shock fronts. Here, the value of $\Delta r_{sf} \sim 1.3$ mm corresponds to the traveling distance of acoustic wave in water for the period of pulse shaping time by the 93 m-long coaxial cable ($\delta t_c \sim 1 \mu s$). This Δr_{sf} value

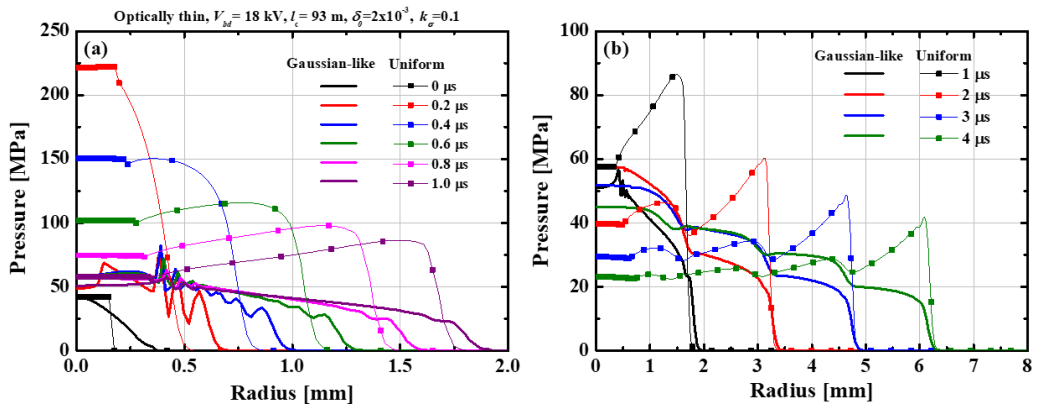


Figure 5.9. Spatial distribution of pressure at each time during the expansion of spark channel for different initial plasma structure in the (a) initial phase and (b) longer time period.

also can be found in Fig. 5.3(b) with the distance between the patterns of wave front. Also, the widely spread pressure wave images can be estimated as another evidence of complicated pressure profile in the longer cable cases.

Figure 5.10 shows the changes of expanding motion of spark channel and resulting pressure wave with respect to the cable length. The effective input energy is defined by subtracting the radiative loss from the input energy. Under given conditions, all variables shown in the figure are affected by the pulse shaping effect when the cable length is longer than 30 m. Focusing on the first plateau of the expansion speed

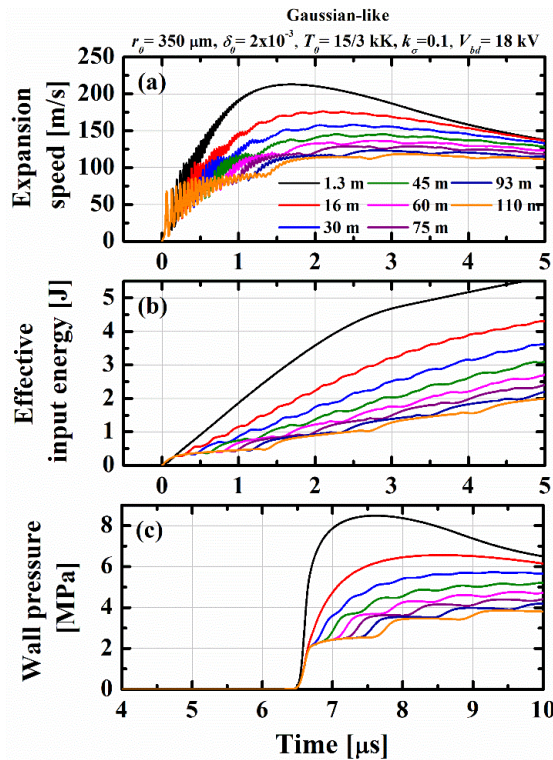


Figure 5.10. Variations of (a) expansion speed, (b) effective input energy, and (c) wall pressure (at 10 cm) calculated with increasing cable length.

curve (in (a)), the effective delivered energy until this point no longer has the simple linear relationship with the pressure wave intensity. This trend is particularly noticeable when the short cable is used and the radiation power loss increases rapidly, which can greatly affect the description on the initial behavior of spark channel. Thus, precise determination of the delivered energy becomes important as someone attempts the simple description as given in Ref. [36, 41].

The peak pressure values increasing with the breakdown voltage (V_{bd}) have been calculated from numerical model for different cable length cases. As shown in Fig. 5.11, the dispersion of peak pressure values observed in the experiment has been successfully reproduced by taking the outer shell into account in the initial plasma structure. In particular, the significant degradation of the peak pressure can be accounted for when the cable is extended from 1.3 m to 93 m. The peak pressure value

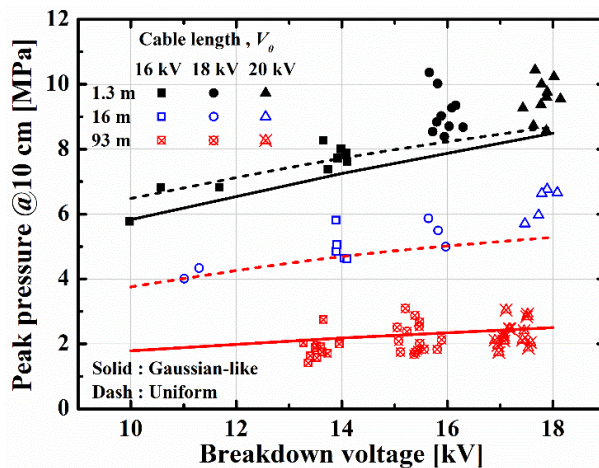


Figure 5.11. Comparison of measured peak pressure with numerical results calculated for different cable lengths with increasing breakdown voltage.

tends to weakly depend on V_{bd} at longer cable. This is because the effective input power cannot fully contribute to accelerate the expanding motion of spark channel due to the damping action of outer shell. In addition, comparing with the numerical results in the case of initially uniform plasma, the pressure wave can be further enhanced in the form of much sharper spike at its front by inducing such a uniform initial plasma. The electrical breakdown induced by the positive supersonic streamer is considered to be the case.

5.2. Evolution of Spark Channel

We have discussed the formative process of shock wave by the spark channel expansion in the early phase of streamer-to-arc transition so far. However, the thermophysical properties are so closely related to the electrical properties of the spark channel that the time evolution of spark channel should be described more carefully. In addition to the physical model of radiation power loss or the radiative heat transfer, the accuracy of EOS and electrical conductivity database get involved in the description of the channel evolution in longer time period (up to 10 μs in this work). In this section, the issues associated with the radiation power loss and the plasma compositions are discussed.

5.2.1. Influence of Radiation Loss

The discharge evolution in longer time period strongly depends on the radiation loss model. As illustrated in Fig. 5.12, the effect of radiation loss is directly related with the plasma resistance, so it can be clearly seen in the case of shorter cable (1.3 m). In the current waveform, the free-wheeling diode (FWD) path is activated at the voltage reversal across the capacitor, then the current is bypassed through the FWD path. This action is simply realized in the advanced circuit model without considering the non-

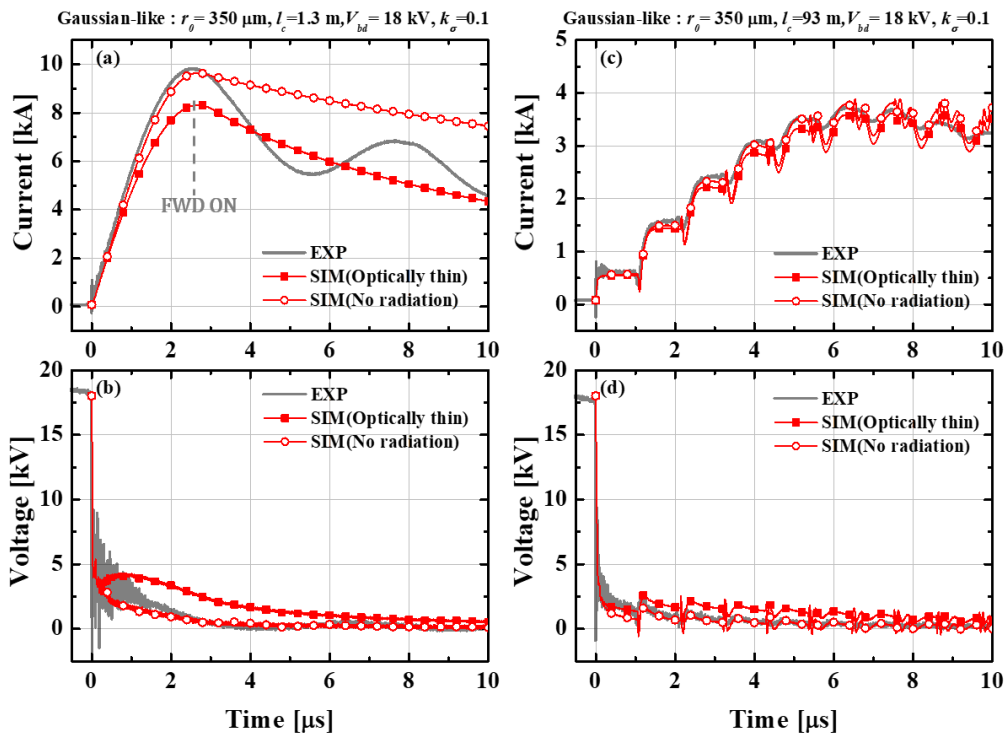


Figure 5.12. Influence of radiation loss on numerical results: (a) current and (b) voltage for the 1.3 m, and (c)-(d) for the 93 m cables, respectively.

linear interaction between the capacitor and the FWD, so there is no oscillation during the current decay of numerical results. On the contrary, since the discharge circuit with the 93 m-long cable has much larger system inductance, the current waveform has changed over a longer time period with smaller amplitude ($I_{peak} < 4$ kA).

The channel resistance and delivered power deduced from the data set presented in the previous figure can be drawn with the corresponding channel radius,

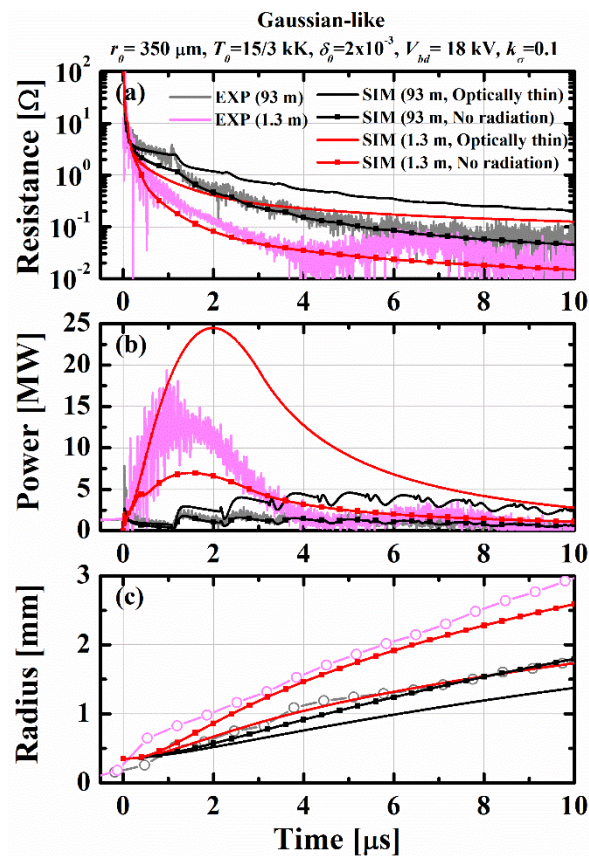


Figure 5.13. Numerical results for different cable length and experimental results: (a) channel resistance, (b) delivered power, and (c) channel radius. The influences of radiation loss are compared.

as shown in Fig. 5.13. Here, the significance of radiation loss model on the channel evolution can be emphasized further. Although we have already discussed the different treatment on the radiation loss in longer cable case with Fig 5.7, the contribution of radiation power loss to the channel dynamics appears to be much larger in shorter cable case. Obviously, the channel resistance (in (a)) rapidly decreases by three orders in magnitude within first 2 μs , and the arc state has been reached very quickly. However, it can be seen that despite the input power is larger, the expansion rate of the channel is slower in the presence of radiation loss (i.e., optically thin). This indicates that the significant amount of energy is emitted by thermal radiation. Similarly, the difference between the measured input power and the numerical results that ignores the radiation effect also allows us to estimate the scale of radiation power. Hence, in order to give a more reliable description on the channel evolution, it is necessary to evaluate the radiation loss more accurately for a given plasma profile.

Figure 5.14 shows the hydrodynamic features calculated for different radiation loss model and cable length to compare their influences. It is interesting that the expansion speed quickly reaches its maximum at $t \sim 1.5 \mu\text{s}$ in the case of 1.3 m-long cable, the extremely strong pressure wave ($P_{pk} \sim 20 \text{ MPa}$) has been produced when the radiation loss is neglected in the calculation. Since the increase of outer channel radius should be followed by pressure build-up within the outer shell, both the pressure and temperature of core region must be raised first. If the current rise rate

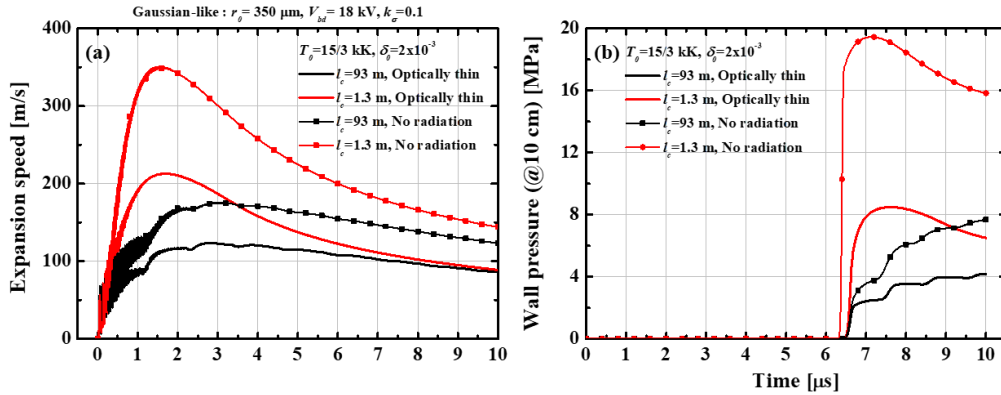


Figure 5.14. Influence of radiation loss on (a) the expansion speed and (b) the wall pressure.

(di/dt) is sufficiently high, the discharge current will be concentrated on the core region to cause this situation. However, this localized Joule heating also leads to the significant radiative heat loss as well as the rapid lowering of the effective channel resistance. Hence, even if the measured curves of channel resistance and channel radius were well described by neglecting radiation effect, they are physically misleading. This means that we have to suggest additional mechanism of accelerating channel expansion other than neglecting the radiation loss.

In order to evaluate the contribution of the radiative loss under the assumption of optically thin plasma, the volume integrated radiation power has been calculated as shown in Fig. 5.15. The graph shows that the emission of thermal radiation almost proportionally increases with the Joule heating on the spark channel. In this numerical result, the thermal radiation takes more than 90% of input power away from the plasma volume and only a small amount of energy can be converted

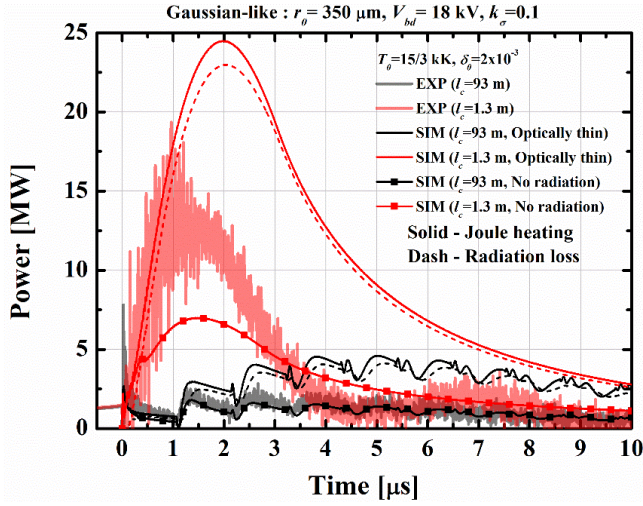


Figure 5.15. Comparison of delivered power and radiation loss calculated under the assumption of optically thin, or no radiation loss.

into the expanding motion of channel. This feature appears irrespective of the cable length, but particularly in the region where the arc plasma is well developed, a large fraction of the input energy disappears in the form of radiation. In this regard, since the localized Joule heating in the core region may lead to the highly center-peaked temperature profile of the spark plasma, it is necessary to re-examine the simple radiation loss model of optically thin body.

The validity of the radiation emission model for the optically thin plasma can be discussed by comparing some characteristic length for the photon absorption (l') with the plasma dimension (a_p) [83]. Indeed, it is well known that the heated body can be assumed as optically thin when $l' \gg a_p$. In this case, photons born inside the plasma easily escape the plasma volume due to the low attenuation along the travel

path. Hence, the optically thin body can emit the thermal radiation from the entire volume. On the contrary, the other extreme case for the radiative heat transfer can be given when $l' \ll a_p$, and this condition is called the *optically thick*. In this case, the photons born from the certain position will be quickly absorbed by the adjacent element. Accordingly, all photons emitted from the optically thick body are born at the surface. For comparison, assuming a uniformly heated body with a shape of cylinder (radius a and length L), total radiant power can be estimated for each case as [83, 95]:

$$P_{rad,thin} \cong (\pi a^2 L) \cdot \frac{\sigma_s T^4}{l_p} \quad (\text{for } l_p \gg a) , \quad (5.2)$$

$$P_{rad,thick} \cong (2\pi a L) \cdot \sigma_s T_s^4 \quad (\text{for } l_R \ll a) , \quad (5.3)$$

where σ_s is the Stefan-Boltzmann constant ($5.67 \times 10^{-8} \text{ [W m}^{-2} \text{ K}^{-4}]$) and T_s is the surface temperature [K]. Two different characteristic lengths of photon attenuation are used, namely the Planck mean free path (l_p) and the Rosseland mean free path (l_R), and they can be expressed in a simplified form as [83]:

$$l_p = 2.3 \times 10^{11} \frac{T^2}{n_a Z^2} \exp\left(\frac{I_H}{k_B T}\right) \frac{k_B T}{I_H} , \quad (5.4)$$

$$l_R = 9 \times 10^{10} \frac{T^2}{n_a Z^2} \exp\left(\frac{I_H}{k_B T}\right) , \quad (5.5)$$

where n_a is the atom density [cm^{-3}], Z is the ionization number, and I_H is the ionization energy of hydrogen ($I_H/k_B \sim 1.5 \times 10^5$ [K]). Eqns. (5.4) and (5.5) are derived by averaging over a frequency domain for hydrogen-like atoms. The Planck averaged mean describes the integrated thermal emission for an optically thin body,

while the Rosseland averaged mean can be used for the integrated energy flux for an optically thin body. It can be roughly said that the absorption and transport of photons can be illustrated by the Planck and Rosseland models, respectively. It should be noted that Eqns. (5.4) may cause large error because the main contribution is coming from the high-energy photons ($h\nu > I_H$) that no more satisfy the approximation to hydrogen-like atom. It is also known that l_P and l_R have a similar level of value, although the averaging method is different, and their difference is not more than factor of four in general.

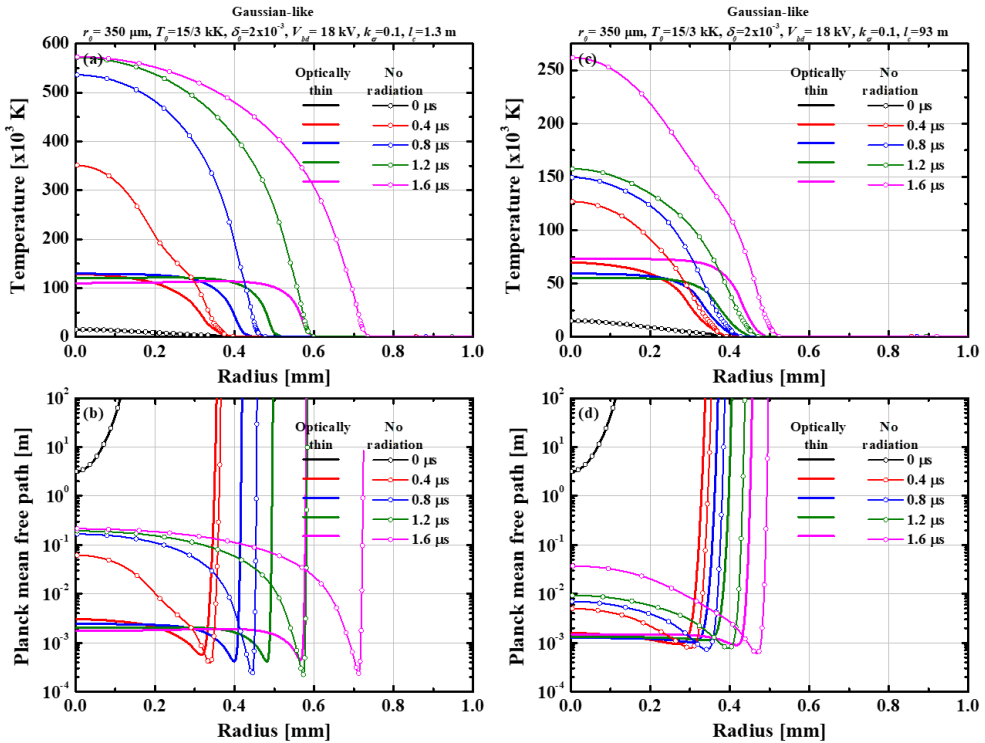


Figure 5.16. Radial profiles of (a) temperature and (b) Planck mean free path calculated for 1.3 m-long cable case, and (c)-(d) for 93 m-long cable case.

Figure 5.16 shows the radial profiles of temperature (in (a), (c)) and the Planck radiation mean free path (in (b), (d)) for the 1.3 and 93 m cable cases. In the 1.3 m-long cable case, the plasma temperature has a rather flat profile at $\sim 10^5$ K level when the optically thin plasma is assumed. The corresponding value of l_p is around 2-3 mm, and its profile is also flat within the core region. A sharp decrease of temperature near the surface leads to the deep trough of the Planck mean free path down to several hundred μs . This gives a possibility of re-absorbing the radiative heat that is emitted from other point of body. In addition, within the temperature range covered during the early transition phase, the overall value of l_p changes dramatically from several meters to submillimeter level. That is, the criterion for an optically thin body ($l_p \gg r_p$) can be violated in the middle of the streamer-to-arc transition. In this regard, it has been found out that the optically thin plasma model has a problem of predicting excessively large radiation loss for the period that requires the additional consideration on the re-absorption of radiation.

It is necessary to discuss the optically thick (or equivalently, blackbody) model as the other extreme of radiation loss model. In this case, the volumetric radiation loss power in the energy conservation equation can be replaced by introducing the radiation heat conduction term as [83, 95]

$$Q_{rad} = -\frac{1}{r} \frac{\partial}{\partial r} \left(r \kappa_{rad} \frac{\partial T}{\partial r} \right), \quad (5.6)$$

where the radiation thermal conductivity κ_{rad} is defined as

$$\kappa_{rad} = \frac{16}{3} \sigma_s l_R T^3. \quad (5.7)$$

As can be inferred from the form of Eq. (5.6), this model explains the simplest radiative heat transfer problem through the improved heat conduction by radiation. That is, it can be interpreted that the thermal radiation born at a specific position of the plasma is transferred to the adjacent element rather than escaping from the body. In principle, since the true loss from the entire plasma can be realized only at the surface, this model leads to the serious underestimation of radiation loss. Considering that above expressions are derived based on the diffusion approximation [83] which assumes the thermal equilibrium between the fluid and radiation field, it is inadequate to apply the optically thick model in this study. Nevertheless, this model will predict the numerical results similar to those case of neglecting the radiation effect in terms of the shock wave formation process. This is because they are unable to consider the radiation loss in the initial phase of transition. Moreover, the temperature flattening by the radiation heat conduction effectively raises the surface temperature. Hence, for some cases, the radiation loss at the surface increases prohibitively large, so the numerical model easily becomes unstable.

5.2.2. Discussions on Gas Composition

In this study, we have used the electrical conductivity (σ) value adjusted by multiplying an empirical correction factor (k_σ) to the original value of $\sigma(\rho, T)$ model calculated with EOS model of water plasma [53] to explain the experimental

results using numerical model. When the electrical conductivity is not adjusted in the numerical model, the channel resistance decreases much faster. Then, the shock wave intensity and channel expansion rate tend to be seriously underestimated regardless of how the initial conditions are set. The strong dependence of the $\sigma(\rho, T)$ model is considered to be the main cause of this problem, since the Joule heating is initiated and the plasma temperature is increased to higher than 10^4 K during the initial phase of transition. That is, considering that the initial Joule heating is localized mostly on the core region, the center peaked profile of the electrical conductivity dominates the effective channel resistance. However, due to the absence of physical background, the simple empirical correction on the electrical conductivity is likely to be criticized for an inconsistency with the EOS model. Therefore, we need to examine the deficiencies of the electrical conductivity model of pure water plasma when applied to the present study.

Among various factors, what we are currently paying attention to is the gas composition of plasma. Considering that the underwater streamer is initiated from the hydrogen bubble produced at the cathode surface, it is expected that the spark plasma is hydrogen abundant. In other words, the oxygen concentration has to be considered lower than that of pure water vapor. In order to compare two extreme cases: the pure hydrogen and the pure water, the EOS and $\sigma(\rho, T)$ tables are generated for the pure hydrogen plasma by modifying the water plasma model [53]. Figure 5.17 shows the

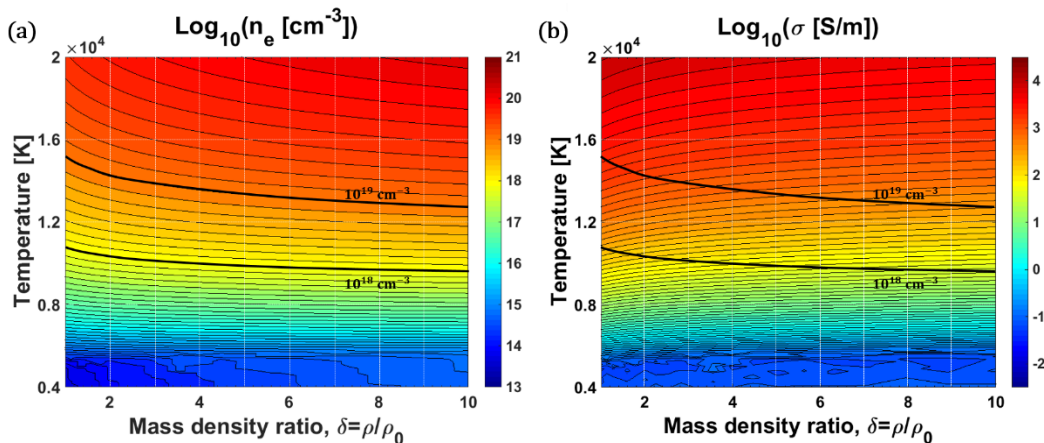


Figure 5.17. Maps for (a) the electron density and (b) electrical conductivity of hydrogen plasma. The plot range is adjusted near the initial plasma condition of PSD.

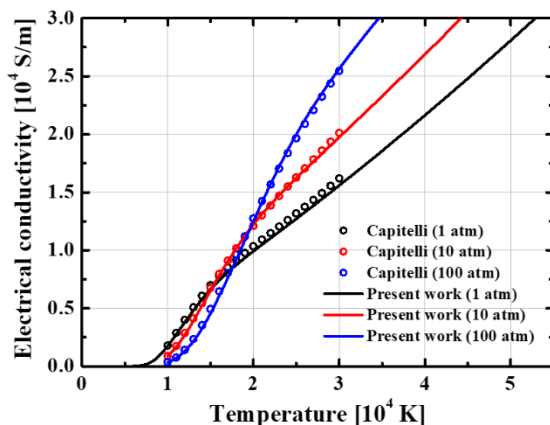


Figure 5.18. Comparison of electrical conductivities calculated by the this work and those by Capitelli [96] for constant pressure of 1, 10, and 100 atm.

maps for the electron density and the electrical conductivity of pure hydrogen plasma near the initial condition of spark plasma. Comparing this figure with Fig. 3.1 (i.e., the water plasma), the initial temperature range of hydrogen plasma estimated from

OES measurement is found lower and narrower. This means that the electron density on the order of $10^{18} - 10^{19} \text{ [cm}^{-3}\text{]}$ can be achieved at lower temperature in the absence of oxygen in the plasma. On the contrary, for a given initial temperature range, the electrical conductivity of hydrogen plasma is much lower than that of water plasma especially in the high density region. Since the ionization energies of hydrogen and oxygen atom are similar, this feature appears to be caused from the relatively large contribution of the electron-neutral collision in the case of hydrogen plasma. The electrical conductivity calculated for hydrogen plasma has been validated using the results presented by Capitelli *et al.* [96]. In order to obtain the electrical conductivity, the ionization equilibrium has to be solved first to determine the plasma composition. Hence, it can be said that the accuracy of the EOS is also indirectly examined by Fig. 5.18.

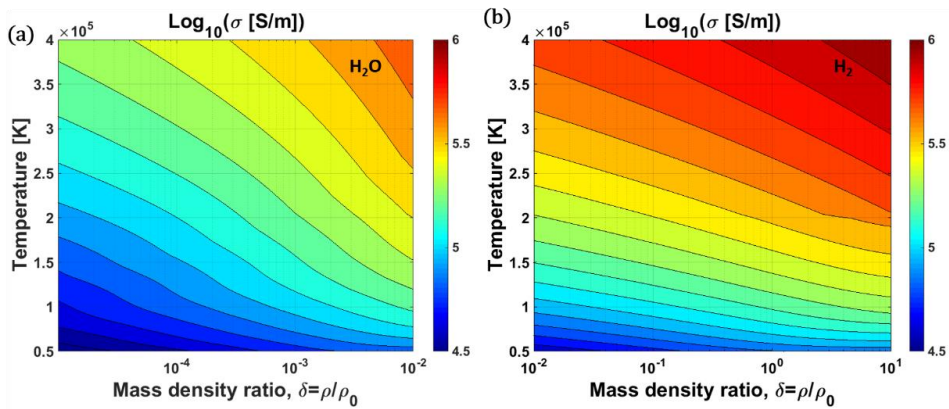


Figure 5.19. Electrical conductivity maps for (a) the water plasma and (b) hydrogen plasma in higher temperature region.

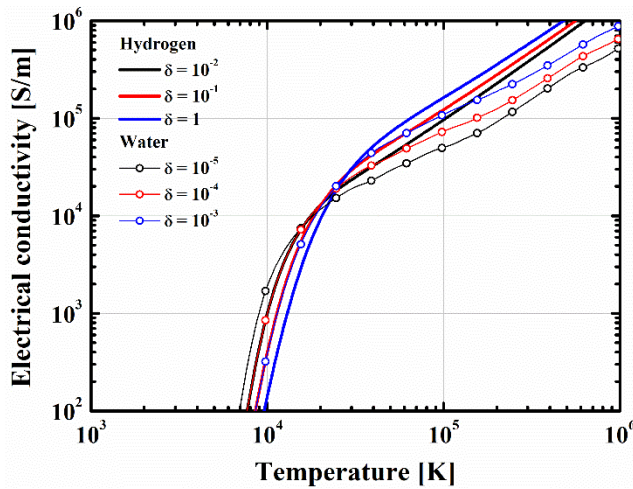


Figure 5.20. Comparison of electrical conductivities of water and hydrogen plasmas calculated at the sampled mass density ratios: $10^{-3} - 1$ for hydrogen and $10^{-5} - 10^{-3}$ for water.

If the temperature range is extended up to 4×10^5 K, the electrical conductivity maps for water and hydrogen plasmas can be compared as shown in Fig. 5.19. Here, the range of mass density ratio (δ) is adjusted to cover the entire spark channel expansion. As already shown by Fig. 5.17, the electrical conductivity of hydrogen plasma is lower than that of water plasma in relatively lower temperature. However, the electrical conductivity of hydrogen plasma increases more rapidly with increasing temperature. In fact, this is primarily originated from the energy partition to the oxygen ions whose ionization energy of upper ionization states are much higher than that of hydrogen. Accordingly, the excessive increase of the electrical

conductivity can be effectively prevented in the presence of the oxygen to some extent. When comparing the electrical conductivity values of hydrogen and water plasmas for some sampled densities as shown in Fig. 5.20, this trend appears even more clearly. In both plasmas, the electrical conductivity decreases with increasing density at low temperature range ($< 2 \times 10^4$ K), whereas this trend is reversed as the temperature is raised. From this reason, the electrical conductivity of hydrogen plasma is even more strongly depending on the temperature. Hence, during the transition of hydrogen plasma, the channel resistance is initially high and slowly decreases in the early phase. As the plasma temperature increases further, the electrical conductivity begins increases more rapidly, and the Joule heating rate will be reduced. Then, the channel expansion will become slower. In order to compensate this feature, one can consider the finite fraction of oxygen in the spark plasma rather than assuming the pure hydrogen plasma. Although, there is no measured data of the initial gas composition, this attempt can significantly contribute to reveal their influences on the streamer-to-arc transition dynamics and the detailed mechanisms.

Chapter 6. Conclusions and Recommendations for Future Work

This chapter summarizes the present study on the dynamic characteristics of underwater streamers and spark plasmas. Some interesting research topics are suggested in the form of recommendations for future work.

6.1. Summary and Conclusions

This work has aimed to investigate the dynamic evolution of underwater streamers and the formation of shock wave by concentrating on the process of streamer-to-arc transition. The improvements achieved in the experimental method and the simulation model can be summarized as follows. The negative subsonic discharge has been used to cause the electrical breakdown due to its morphological features favoring the shock wave formation. The practical limitation of negative subsonic mode originated from the screening effect is successfully compensated by preconditioning a gap with water electrolysis. In the fast ignition mode, the negative subsonic streamers can be directly initiated from the initial hydrogen bubble, so the uncertainty associated with the bubble formation process has been minimized subsequently. In order to measure the time-varying characteristics of underwater PSD, the optical diagnostics such as the

focused-shadowgraphy and the VPHG (volume phase holographic grating) spectrograph have been designed, constructed, and optimized. A closer observation on the streamer-to-arc transition period could be realized by decelerating the transition rate using a longer coaxial cable (93 m). The detailed behavior of electrical power transmission including the pulse forming action of coaxial cable could be efficiently described by T-sectioned cable model. This major improvement allowed the self-consistent simulation to become much more realistic particularly for the streamer-to-arc transition. The systematic analysis using simulation model has been carried out based on the measured initial plasma parameters, and the validity of numerical results is confirmed by comparing with experimental results.

Provided the proper position, size, and contact condition of initial hydrogen bubble, the fast discharge mode can be ignited, without additional bubble formation. Even if the preconditioning duration is shorter than the threshold value for the direct discharge ignition, initial microbubbles still act as nucleation sites for the vapor bubble formation and effectively shorten the overall pre-breakdown period. In the fast ignition mode, gaseous streamer discharge is produced inside a hydrogen bubble, and its electron density strongly depends on the applied voltage amplitude. It is found that this internal discharge requires the continuous charge removal at the bubble-water interface. Accordingly, the OES signals appear to be discernible only at higher conductivity water, and no abrupt change of electron density was detected at the moment of streamer inception. In the early phase of propagation, its motion is

governed by the electro-hydrodynamic (EHD) effect, while the propagation mode transition to the Ohmic will be followed as the streamer gets closer to the anode. This feature has been demonstrated by the propagating behavior of streamers exposed to the fluctuating voltage pulse. For the propagation mode transition, the threshold value of electron density measured at the channel base has been found as $5-8 \times 10^{17} \text{ cm}^{-3}$, so this transition occurs earlier in higher conductivity water. At the moment of breakdown, the electron density (n_e) measured at head region was so high ($\sim 10^{19} \text{ cm}^{-3}$) that the four-fold variation of n_e could emerge along the channel length.

In the breakdown period, the pulse shaping effect becomes pronounced especially in the early phase of channel expansion when we reduced the rate of streamer-to-arc transition by using a longer transmission line. The numerical results on the breakdown period demonstrated that the underwater streamer plays an essential role in the shock wave formation by determining the shape and composition of the initial spark plasma. In fact, there found a cold layer surrounding the highly conductive core in the initial spark channel experimentally. Corresponding profiles of the plasma density and temperature allows the outer layer to act as a shock absorber, the formation of shock wave slows down. In addition, as the internal pressure wave is dissipated within this outer layer, the initial expansion of spark channel is further influenced by the pulse forming action of coaxial cable. Accordingly, the strong dependence of the measured peak pressure on the breakdown voltage for different

cable lengths has been successfully reproduced by numerical model. During the early phase of streamer-to-arc transition that mostly determines the physical properties of shock front, relatively low plasma temperature makes the radiation absorption length larger than the plasma dimension. Thus, the shock wave formation process can be reasonably described without considering the re-absorption of radiation power inside the plasma volume. It is also revealed that even though the current rise rate is much increased, the energy transfer efficiency to the hydraulic motion becomes significantly degraded by the rapidly increasing radiation loss.

As attempting to operate the conventional underwater PSD technique to harsher conditions, e.g., high water conductivity, water flows, high hydrostatic pressure, and long transmission line, numerous difficulties have been encountered. Among them, some critical issues, that are associated with the prohibitively large energy loss during the bubble formation or the awfully low energy transfer efficiency to the shock wave formation due to damping effect of large bubble cluster, can be effectively handled by introducing our experimental technique: the electrolysis preconditioning and the negative subsonic discharges. Nevertheless, the degradation of the shock wave intensity caused by the extended transmission line proved unavoidable as long as the capacitive discharge system is retained. Therefore, the operation schemes such as using the secondary shock waves produced by the cavity collapses can be considered as alternatives.

6.2. Recommendations for Future Work

Experimental and numerical methods have been proposed to investigate the generation process of underwater shock wave. Extensions of this work, or studies with other perspectives can be pursued as future works.

The experimental techniques proposed by present work can be applicable to various industrial underwater PSD applications. Only minor modification for the preconditioning pulse modulation is necessary in the existing PSD system. The most evident benefit is the remarkable enhancement of energy efficiency for the generation of strong shock waves by reducing the pre-breakdown energy loss. Accordingly, the main operating parameters such as the main storage capacitance and initial charging voltage can be lowered, so some practical issues related to the erosive damages on the electrode surfaces or the system maintenance can be much relieved.

Further investigations on the initiation of supersonic streamers at lower applied voltages assisted by initial bubbles are also strongly recommended. When trying to produce the hydrogen bubbles on the anode surface, more complex circuit topology is required compared to the present preconditioning pulse modulator because of the opposite polarity between the main HV pulse and the preconditioning pulse. Nevertheless, it is worth noting that the positive supersonic streamer has much thinner outer layer and faster propagation speed, and these factors will result in the higher initial density of the spark plasmas that clearly contributes to the formation of strong

shock waves.

It is necessary to upgrade the equation of state and electrical conductivity models for the water vapor – hydrogen mixture based on the fact that the negative subsonic discharge has been ignited from a large hydrogen bubble. Until the propagation mode changes to the Ohmic regime, it is difficult to say that there is a continuous vaporization of water in front of the streamer head. Thus, it seems that almost half of the streamer consists of pure hydrogen rather than water vapor. However, we still expect that the hydrogen and water vapor will rapidly take well-mixed state after the breakdown occurs. Hence, the improved material property model needs to establish a brilliant way to consider the fraction of hydrogen and water vapor in their calculation.

Meanwhile, describing the dynamic evolution of the spark channel in longer time scale ($\sim 10 \mu\text{s}$) strongly requires the additional model of radiation transport inside the channel. In fact, the molecular reactions such as photodissociation and photoionization play a major role in the radiation absorption at low temperature ($T < 6000 \text{ K}$). Although the central temperature of spark channel is much higher than 6000 K during the breakdown period, the outer cold layer will contain much more water molecules than core region. Accordingly, it is highly probable that the radiation escaped from the hotter region can be reabsorbed at the outer cold layer, and thus the radiation transport must be included in the simulation model to precisely predict the rapid expansion of spark channel observed in the experiments.

OES system for the underwater PSD also can be improved further by adopting higher performance measurement device such as visible streak camera or ultrafast-frame camera. These devices typically have superior dynamic range, detector pixel resolution, and time resolution compared to existing fast-frame camera, so that additional OES techniques can be applied to measure the electron density using the Stark broadening of $H\beta$ line or the rotational temperature of $\text{OH}(A - X)$ from the Boltzmann plot method.

Finally, based on the fundamental understandings on the underwater PSD, sequential electrical breakdown of multiple gaps placed in series can be attempted. In the application oriented view point, this approach deserves to receive a special attention as it can effectively increase the treatment volume without up-scaling the pulsed power system. However, the shock wave intensities produced at each gaps are expected to be highly non-uniform due to different initial plasma conditions of each water gap. Hence, technical difficulties will emerge for minimizing the delay between the electrical breakdowns of adjacent water gaps.

Bibliography

- [1] P. K. Watson and A. H. Sharbaugh, "High-field conduction currents in liquid n-hexane under microsecond pulse conditions", *J. Electrochem. Soc.* **107**, 516 (1960).
- [2] H. M. Jones and E. E. Kunhardt, "Pulsed dielectric breakdown of pressurized water and salt solutions", *J. Appl. Phys.* **77**, 795 (1995).
- [3] V. Y. Ushakov, V F Klimkin, S. Korobeynikov, *Impulse Breakdown of Liquids*, Springer-Berlin (2007).
- [4] G. Touya, T. Reess, L. Pécastaing, A. Gibert, and P. Domens, "Development of subsonic electrical discharges in water and measurements of the associated pressure waves", *J. Phys. D: App. Phys.* **39**, 5236 (2006).
- [5] E. M. Bazelyan, Yu. P. Raizer, *Spark discharge*, CRC Press-New York (1998).
- [6] X. D. Li, G. Y. Zhou, S. W. Liu, Z. Y. Li, and F. C. Lin, "Subsonic streamers in water: initiation, propagation and morphology", *J. Phys. D: Appl. Phys.* **50**, 255301 (2017).
- [7] J. Qian, R. P. Joshi, E. Schamiloglu, J. Gaudet, J. R. Woodworth, and J. Lehr, "Analysis of polarity effects in the electrical breakdown of liquids", *J. Phys. D: Appl. Phys.* **39**, 259 (2006).
- [8] V. Giraud and P. Krebs, "The onset of electron localization in subcritical water vapor", *Chem. Phys. Lett.* **86**, 85 (1982).
- [9] H. M. Jones and E. E. Kunhardt, "Ionic sheath formation in water and aqueous solutions and its influence on pulsed dielectric breakdown," *Digest of Technical Papers. Tenth IEEE International Pulsed Power Conference*, Albuquerque, NM, USA, 1995, pp. 580-585.

- [10] V. A. Panov, L. M. Vasilyak, S. P. Vetchinin, V. Ya. Pecherkin, and E. E. Son, "Pulsed electrical discharge in conductive solution", *J. Phys. D: Appl. Phys.* **49**, 385202 (2016).
- [11] P. Ceccato, *Filamentary plasma discharge inside the water : initiation and propagation of a plasma in a dense medium*, Ph.D. Thesis, Ecole Polytechnique (2009).
- [12] J. C. Martin, "Nanosecond pulse techniques," in *Proceedings of the IEEE* **80**, 934 (1992).
- [13] T. H. Martin, A. H. Guenther, and M. Kristiansen, *J. C. Martin on Pulsed Power*, Plenum Press New York (1996).
- [14] R. J. Adler, *Pulse Power Formulary*, Albuquerque, NM: North Star Research Corporation (1991).
- [15] J. F. Kolb, R. P. Joshi, S. Xiao, and K. H. Schoenbach, "Streamers in water and other dielectric liquids", *J. Phys. D: Appl. Phys.* **41**, 234007 (2008).
- [16] K. J. Chung, S. G. Lee, Y. S. Hwang, and C. Y. Kim, "Modeling of pulsed spark discharge in water and its application to well cleaning", *Curr. Appl. Phys.* **15**, 977 (2015).
- [17] Y. Liu, Z. Y. Li, X. D. Li, S. W. Liu, G. Y. Zhou, and F. C. Lin, "Intensity improvement of shock waves induced by liquid electrical discharges", *Phys. Plasmas* **24**, 043510 (2017).
- [18] Yu. P. Raizer, *Gas Discharge Physics*, Springer, Berlin (1991).
- [19] K. C. Kao, J. P. C. McMath, "Time-dependent pressure effect in liquid dielectrics", *IEEE Trans. Electr. Insul.* **5**, 64 (1970).
- [20] V. M. Atrazhev, V. S. Vorob'ev, I. V. Timoshkin, M. J.. Given, S. J. MacGregor, "Mechanism of impulse breakdown in liquid: the role of Joule heating and formation of gas cavities", *IEEE Trans. Plasma Sci.* **38**, 2644 (2010).

- [21] S. M. Korobeynikov and Y. N. Sinikh, "Bubbles and breakdown of liquid dielectrics," Conference Record of the 1998 IEEE International Symposium on Electrical Insulation (Cat. No.98CH36239), Arlington, VA, USA, 1998, pp. 603-606.
- [22] B. R. Locke and S. M. Thagard, "Analysis and review of chemical reactions and transport processes in pulsed electrical discharge plasma formed directly in liquid water", *Plasma Chem. Plasma Process* **32**, 875 (2012).
- [23] L. Schaper, W. G. Graham, and K. R. Stalder, "Vapour layer formation by electrical discharges through electrically conducting liquids - modelling and experiment", *Plasma Source Sci. Technol.* **20**, 034003 (2011).
- [24] S. M. Korobeinikov, A. V. Melekhov, and A. S. Besov, "Breakdown initiation in water with the aid of bubbles", *High Temp.* **40**, 652 (2002).
- [25] P. Bruggeman and C. Leys, "Non-thermal plasmas in and in contact with liquids", *J. Phys. D: Appl. Phys.* **42**, 053001 (2009).
- [26] V. Stelmashuk, "Time-resolved processes in a pulsed electrical discharge in water generated with shock wave assistance in a plate-to-plate configuration", *J. Phys. D: Appl. Phys.* **47**, 495204 (2014).
- [27] V. Stelmashuk, "Microsecond electrical discharge in water in plate-to-plate configuration with nitrogen bubble injection", *IEEE Trans. Plasma Sci.* **44**, 702 (2016).
- [28] M. Burlion, P. Dancer, and F. Lacoste, "Design and characterization of a shock wave generator using canalized electrical discharge: Application to lithotripsy", *Rev. Sci. Instrum.* **65**, 2356 (1994).
- [29] M. Hamelin, F. Kitzinger, S. Pronko and G. Schofield, "Hard rock fragmentation with pulsed power," Ninth IEEE International Pulsed Power Conference, Albuquerque, NM, USA, 1993, pp. 11-14.
- [30] Y. Sun, J. Zhou, R. Fu., Y. Gao, P. Yan, and T. Jiang, "Experimental Study on

Rock Fracturing by using Pulsed Power Technology”, 2014 IEEE International Power Modulator and High Voltage Conference (IPMHVC), Santa Fe, NM, USA, 2014, pp. 229-232.

- [31] M. S. Mazzola, M. G. Grothaus, M. Walch, and J. Jones-Meehan, “New electrical control methods to prevent power plant fouling,” in Proc. 10th IEEE Int. Pulsed Power Conf., Albuquerque, NM, USA, 1995, pp. 34–39.
- [32] J. W. Mackersie, I. V. Timoshkin, and S. J. MacGregor, “Generation of high-power ultrasound by spark discharges in water”, IEEE Trans. Plasma Sci. **33**, 1715 (2005).
- [33] K. J. Chung, S. G. Lee, J. J. Dang, G. H. Choi, Y. S. Hwang, C. Y. Kim, and Y. J. Park, “Feasibility study for the cleaning of well screens using high-voltage pulsed discharge”, J. Eng. Geol. 23, 29 (2013) (in Korean).
- [34] G. Houben and C. Treskatis, *Water Well Rehabilitation and Reconstruction*, New York: McGraw-Hill, 2007.
- [35] K. J. Chung, Y. S. Hwang, C. Y. Kim, and S. C. Jeon, “Cleaning horizontal water wells using shock wave generated by underwater spark discharge”, in Proc. Euro Asian Pulsed Power Conference with BEAMS and MEGAGAUSS 2016, Estoril, Portugal, No. 301.
- [36] K. Lee, K. J. Chung, Y. S. Hwang, and C. Y. Kim, “Underwater spark discharge with long transmission line for cleaning horizontal wells”, J. Appl. Phys. **121**, 243302 (2017).
- [37] D. D. Caulfield, “Predicting sonic pulse shapes of underwater spark discharges”, Deep-Sea Res. **9**, 339 (1962).
- [38] W. J. Guman and B. G. Humphrey, Jr., *Studies on an electric discharge underwater sound source*, Fairchild Hiller Corporation, Republic Aviation Division, New York, (1968).
- [39] J. W. Mackersie, I. V. Timoshkin, and S. J. MacGregor, “Generation of high-

power ultrasound by spark discharges in water”, IEEE Trans. Plasma Sci. **33**, 1715 (2005).

- [40] I. V. Timoshkin, R. A. Fouracre, M. J. Given, and S. J. MacGregor, “Hydrodynamic modelling of transient cavities in fluids generated by high voltage spark discharges”, J. Phys. D: Appl. Phys. **39**, 4808 (2006).
- [41] S. G. Lee, K. J. Chung, and Y. S. Hwang, “Correlation of the peak pressure generated by an underwater spark discharge with energy absorption in a spark channel”, J. Korean Phys. Soc. **66**, 1845 (2015).
- [42] X. D. Li, Y. Liu, S. W. Liu, Z. Y. Li, G. Y. Zhou, H. Li, F. C. Lin, and Y. Pan, “Influence of deposited energy on shock wave induced by underwater pulsed current discharge”, Phys. Plasmas **23**, 103104 (2016).
- [43] Y. Liu, Z. li, X. D. Li, G. Zhou, H. Li, Q. Zhang, and F. C. Lin, “Energy transfer efficiency improvement of liquid pulsed current discharge by plasma channel length regulation method”, IEEE Tans. Plasma Sci. **45**, 3231 (2017).
- [44] A. I. Ioffe, “Theory of the initial stage of an electrical discharges in water”, J. Appl. Mech. Tech. Phys. **7**(6), 47 (1966).
- [45] J. A. Cook, A. M. Gleeson, R. M. Roberts, and R. L. Rogers, “A spark-generated bubble model with semi-empirical mass transport”, J. Acoust. Soc. Am. **101**, 1908 (1997).
- [46] X. Lu, Y. Pan, M. Liu, and H. Zhang, “Spark model of pulsed spark discharge in water”, J. Appl. Phys. **91**, 24 (2002).
- [47] A. W. H. Kratel, *Pulsed power discharge in water*, Ph.D. Dissertation, California Institute of Technology (1996).
- [48] S. Lan, J. X. Yang, A. Samee, J. L. Jiang, and Z. Q. Zhou, “Numerical simulation of properties of charged particles initiated by underwater pulsed discharge”, Plasma Sci. Technol. **11**, 481 (2009).

- [49] E. Gidalevich, R. L. Boxman, and S. Goldsmith, “Hydrodynamic effects in liquids subjected to pulsed low current arc discharges”, *J. Phys. D: Appl. Phys.* **37**, 1509 (2004).
- [50] E. Gidalevich and R. L. Boxman, “Sub- and supersonic expansion of an arc channel in liquid”, *J. Phys. D: Appl. Phys.* **39**, 652 (2006).
- [51] O. A. Sinkevich and A. L. Shevchenko, “Numerical investigation of electric discharge in water”, *Fluid Dyn.* **18**, 422 (1983).
- [52] J. W. Robinson, “Finite-difference simulation of an electrical discharge in water”, *J. Appl. Phys.* **44**, 76 (1973).
- [53] K. J. Chung and Y. S. Hwang, “Thermodynamic properties and electrical conductivity of water plasma”, *Contrib. Plasma Phys.* **53**, 330 (2013).
- [54] I. Kim, D. K. Kim, S. H. Baek, and S. Y. Song, “Magnetohydrodynamic behavior of warm dense plasmas created by underwater wire explosion”, *Proceedings of 33rd EPS Conference on Plasma Physics*, 2006. P-5.064.
- [55] G. S. Settles, *Schlieren and Shadowgraph Techniques-Visualizing Phenomena in Transparent Media*, Springer-Verlag Berlin (2001).
- [56] G. C. Burdiak, *An Investigation of Cylindrical Liner Z-pinches as Drivers for Converging Strong Shock Experiments*, Ph.D. Thesis, Imperial College London (2012).
- [57] <https://www.thorlabs.com>
- [58] P. Bruggeman, D. Schram, M.A. Gonzalez, R. Rego, M. G. Kong, and C. Leys, “Characterization of a direct dc-excited discharge in water by optical emission spectroscopy”, *Plasma Sources. Sci. Technol.* **18**, 025017 (2009).
- [59] W. Z. Wang, M. Z. Rong, J. D. Yan. A. B. Murphy, and J. W. Spencer, “Thermodynamic properties of nitrogen plasmas under thermal equilibrium and non-equilibrium conditions”, *Phys. Plasmas* **18**, 113502 (2011).

- [60] K. C. Mehr, N. Tiwari, and S. Ghorui, “Thermodynamic and transport properties of nitrogen plasma under thermal equilibrium and non-equilibrium conditions”, *Plasma Chem. Plasma Process* **35**, 605-637 (2015).
- [61] H. R. Griem, *Spectral Line Broadening by Plasmas*, Academic, New York (1974).
- [62] M. Ivkovic, S. Jovicevic, and N. Konjevic, “Review: low temperature density diagnostics: development of optical emission spectroscopic techniques and some applications to microwave induced plasmas”, *Spectrochim. Acta B* **59**, 591 (2004).
- [63] D. E. Kelleher, W. L. Wiese, V. Helbig, R. L. Greene, and D. E. Oza, “Advances in plasma broadening of atomic hydrogen”, *Phys. Scr.* **T47**, 75 (1993).
- [64] G. A. Kobzev, I. T. Iakubov, and M. M. Popovich, *Transport and Optical Properties of Nonideal Plasma*, Plenum Press, New York (1995).
- [65] A. Descoedres, Ch. Hollenstein, R. Demellayer, and G. Walder, “Optical emission spectroscopy of electrical discharge machining plasma”, *J. Phys. D: Appl. Phys.* **37**, 875 (2004).
- [66] M. A. Gigosos, M. . Gonzalez, and V. Cardenoso, “Computer simulated Balmer-alpha, -beta and -gamma Stark line profiles for non-equilibrium plasmas diagnostics”, *Spectrochim. Acta B* **58**, 1489 (2003).
- [67] M. A. Gigosos and V. Cardenoso, “New plasma diagnosis tables of hydrogen Stark broadening including ion dynamics”, *J. Phys. B: At. Mo. Opt. Phys.* **29**, 4795 (1996).
- [68] S. Koneshan, J. C. Rasaiah, R. M. Lynden-Bell, and S. H. Lee, “Solvent structure, dynamics, and ion mobility in aqueous solutions at 25 C”, *J. Phys. Chem. B.* **102**, 4193-4204 (1998).
- [69] J. F. James, *Spectrograph Design Fundamentals*, Cambridge University Press, Cambridge, UK (2007).

- [70] M. Capitelli, G. Colonna, and A. D'Angola, *Fundamental Aspects of Plasma Chemical Physics*-Chapter 6, Springer (2012).
- [71] D. Kim and I. Kim, "Calculation of ionization balance and electrical conductivity in nonideal aluminum plasma", *Phys. Rev. E* **68**, 056410 (2003).
- [72] R. J. Zollweg and R. W. Liebermann, "Electrical conductivity of nonideal plasmas", *J. Appl. Phys.* **62**, 3621 (1987).
- [73] M. R. Zaghoul, "A simple theoretical approach to calculate the electrical conductivity of nonideal copper plasma", *Phys. Plasmas* **15**, 042705 (2008).
- [74] W. Ebeling, W. D. Kremp, and D. Kraeft, *Theory of Bound States and Ionization Equilibrium in Plasmas and Solids*, Akademie-Verlag, Berlin (1976).
- [75] M. R. Zaghoul, "A consistent model for the equilibrium thermodynamic functions of partially ionized filbe plasma with Coulomb corrections", *Phys. Plasmas* **10**, 527-538 (2003).
- [76] T. Dheane and D. d. Zutter, "Selection of lumped element models for coupled lossy transmission lines", *IEEE Trans. Comput. Aided Des.* **11**, 805 (1992).
- [77] P. J. Nahin and O. Heaviside, *The Life, Work, and Times of an Electrical Genius of the Victorian Age*, JHU Press (2002).
- [78] P. W. Smith, *Transient Electronics: Pulsed Circuit Technology*, John Wiley & Sons, (2011).
- [79] S. R. Brinkley Jr., J. G. Kirkwood, "Theory of the propagation of shock waves", *Phys. Rev.* **71**, 606 (1947).
- [80] Q. Liu and Y. Zhang, "Shock wave generated by high-energy electric spark discharge", *J. Appl. Phys.* **116**, 153302 (2014).
- [81] I. Z. Okun, "Use of similitude and dimensional methods in investigation of electrical discharges in water", *Sov. Phys. Tech. Phys.* **37**, 1729 (1967).

- [82] V. I. Oreshkin, S. A. Chaikovskiy, and N. A. Rarakhin, “Water bath effect during the electrical underwater wire explosion”, *Phys. Plasmas* **14**, 102703 (2007).
- [83] Ya. B. Zel’dovich and Yu. P. Raizer, *Physics of Shock Waves and High-Temperature Hydrodynamic Phenomena*, Dover Publications Inc., New York (2002).
- [84] O. R. Enriquez, C. Hummelink, G. W. Bruggert, D. Lohse, A. Prosperetti, D. v. d. Meer, and C. Sun, “Growing bubbles in a slightly supersaturated liquid solution”, *Rev. Sci. Instrum.* **84**, 065111 (2013).
- [85] R. S. Schechter, A. Graciaa, and L. Lachaise, “The electrical state of a gas/water interface”, *J. Colloid Interf. Sci.* **204**, 398 (1998).
- [86] N. Yu. Babaeva, R. S. Berry, G. V. Naidis, B. M. Smirnov, E. E. Son, and D. V. Tereshonok, “Kinetic and electrical phenomena in gas-liquid systems”, *High Temp.* **54**, 745-766 (2016).
- [87] A. H. Sharbaugh, J. C. Devins, and S. J. Rzed, “Progress in the field of electric breakdown in dielectric liquids”, *IEEE Trans. Electr. Insul.* **EI-13**, 249 (1978).
- [88] Yu. D. Varlamov, Yu. P. Meshcheryakov, S. I. Lezhnin, M. R. Predtechenskii, and S. N. Ul’yankin, “Evolution of a vapor cavity during explosive boiling on a film microheater: experiment and numerical simulation”, *J. Appl. Mech. Tech. Phys.* **48**, 534 (2007).
- [89] K. Lee, K. J. Chung, and Y. S. Hwang, “Enhanced shock wave generation via pre-breakdown acceleration using water electrolysis in negative streamer pulsed spark discharges”, *Appl. Phys. Lett.* **112**, 134101 (2018).
- [90] A. Fridman, *Plasma Chemistry*, Cambridge University Press, Cambridge, UK, 2008.
- [91] P. K. Watson, W. G. Chadband, and M. Sadeghzadeh-Araghi, “The role of electrostatic and hydrodynamic forces in the negative-point breakdown of liquid dielectrics”, *IEEE Trans. Elec. Insul.* **26**, 543 (1991).

- [92] J. R. Melcher, “Electrohydrodynamic charge relaxation and interfacial perpendicular field instability”, *Phys. Fluid* **12**, 778 (1969).
- [93] K. J. Chung, K. Lee, Y. S. Hwang, and D. K. Kim, “Numerical models for electrical explosion of copper wires in water”, *J. Appl. Phys.* **120**, 203301 (2016).
- [94] A. Grinenko, V. Ts. Gurovich, Ya. E. Krasik, A. Sayapin, S. Effimov, and J. Felsteiner, “Analysis of shock wave measurements in water by a piezoelectric pressure probe”, *Rev. Sci. Instrum.* **75**, 240 (2004).
- [95] L. Warne, R. Jorgenson, and J. Lehr, *Resistance of Water Spark*, Sandia Report No. SAND2005-6994, Sandia National Laboratory, 2005.
- [96] M. Capitelli, R. Celiberto, C. Gorse, A. Laricchiuta, D. Pagano, and P. Traversa, “Transport properties of local thermodynamic equilibrium hydrogen plasmas including electronically excited states”, *Phys. Rev. E.* **69**, 026412 (2004).

Abstract in Korean

수중 펄스 스파크 방전에서 스트리머-아크 천이에 의한 충격파의 생성

이 건

에너지시스템공학부

(펄스파워 및 플라즈마공학 전공)

서울대학교 대학원

수중 펄스 스파크 방전(PSD, pulsed spark discharge)은 주변 매질인 물과 활발히 상호작용하며 빠르게 팽창하는 고에너지 플라즈마를 수반한다. 수중 펄스 스파크 방전은 물속에 삽입된 전극 양단에 고전압펄스를 인가함으로써 발생하며, 소요 에너지가 크다는($> 100 \text{ J/pulse}$) 특징이 있다. 큰 입력 파워는 스파크 플라즈마의 급격한 팽창과 그로 인한 수중 충격파의 발생을 야기한다. 이에 서울대학교에서는 수중 펄스 스파크 방전 기술을 전기적 파라미터를 통해 제어하는 수중 충격파의 발생원으로서 연구해왔다. 이 기술은 지하수 관정에서 관석에 의한 스크린 공막힘의 해소와 상수 처리시설에서의 녹조류 처리에 적용하고자 시도되어왔다.

일반적인 수중 스파크 방전의 진행과정은 다음과 같다. 수중 갭에 고전압 펄스가 인가되면 전기장이 집중되어 있는 전극 팁의 주변부에서 활발한 줄 가열(Joule heating)이 일어난다. 일정한 형성시간이 지난 후 증기 버블(vapor bubble)이 발생, 팽창하게 된다. 전기-유체역학적(electro-hydrodynamic) 불안정성에 의하여 팽창한 버블의 표면에서 돌출부(protrusion)가 형성되면 곧 이 부위는 수중 스트리머(streamer)로 변화하여 빠른 속도로 상대편 전극을 향해 이동하기 시작한다. 이 스트리머가 전극간 사이를 완전히 가로지르면 최종적인 전기 절연과괴(electrical breakdown)가 일어난다. 이때, 스파크 플라즈마는 스트리머의 형태로부터 수 ns 이내의 짧은 시간 내에 거의 순간적으로 형성되어 그 물리적 특성이 매우 큰 폭에서 빠르게 변화한다. 특히 스파크 플라즈마의 전기적 특성은 충격파 생성에 매우 핵심적인 역할을 하는데, 이는 플라즈마의 전기적 특성이 플라즈마 부하(load)와 펄스 전원 시스템간의 전력 전달을 결정하는 요소이기 때문이다.

본 연구에서는 스파크 플라즈마의 초기 파라미터를 밝혀내기 위해 수중 스트리머의 시변 특성을 규명하는 실험적 연구를 수행하였다. 또한, 스파크 방전에 대한 자기일관적 시뮬레이션 모델을 이용하여 수중 충격파의 생성과정을 상술하기 위한 노력을 기울였다. 그 결과, 플라즈마 파라미터의 동적 변화와 주변부 물의 유체역학적 거동을 동시에 기술할 수 있었다.

아음속 스트리머(subsonic streamer)의 특성 및 아크 상태로의 신속한 전이과정을 면밀히 관찰하기 위해 새로운 실험 방법을 제안하였다. 본 실험에서는 음극 표면에서 스트리머가 개시되는 아음속 음극 방전모드를

활용하였다. 일반적인 아음속 양극 모드와 비교할 때 아음속 음극 모드의 스트리머는 줄기 주위에 큰 버블 클러스터가 없는 나무 형태(tree-like structure)를 띄고 더 빠른 전파속도를 갖고 있으므로, 절연과피로 이어질 때 충격과 생성에 훨씬 더 효과적인 것으로 기대하였다. 스크리닝 효과(screening effect)에 의해 버블 생성속도가 심각하게 지연된다는 음극 방전모드의 가장 큰 문제점은 전기분해를 이용하여 수중 갭을 전처리(preconditioning)함으로써 성공적으로 해결되었다. 음극 표면에서 전기분해에 의해 생성되는 수소 버블 덕분에 전반적인 전-절연과피 과정(pre-breakdown process)이 크게 단축되었고, 이에 따라 버블생성 프로세스가 내포하는 확률적 특성(stochastic nature)과 이로부터 기인하는 불확실성을 최소화 할 수 있었다. 수중 펄스 스파크 방전의 시변 특성을 관찰하기 위하여 그림자 촬영법(shadowgraphy) 및 광학적 발광 분광분석(optical emission spectroscopy, OES)과 같은 광학진단계가 설계 및 구축되었다. 수중 스트리머와 스파크 채널의 유체역학적 특성은 그림자 이미지를 통하여 파악하는 한편, 플라즈마 방전의 시변 전자 밀도는 OES 분석을 통하여 도출하였다.

전기분해 전처리를 충분히 길게 지속 할 때 생성되는 결합된 형태(merged form)의 수소버블에 고전압 펄스가 인가되는 경우, 추가적인 버블생성 단계가 생략되고 즉각적으로 스트리머 방전이 시작된다. 긴 동축 케이블 (93 m)의 충전효과(line charging effect)에 의한 전류-전압 변동(fluctuation)은 수소버블 내부 방전(internal discharge)의 전자밀도 변화와 유사한 경향을 보였으나, 정작 스트리머의 개시시점에는 전자밀도의 눈에 띄만한 증가가 관찰되지 않았다. 대신, 채널 하부(channel base)에

서의 전자밀도는 스트리머의 전파속도가 크게 증가하는 시점에 함께 증가하였으므로, 전기유체역학(EHD)에서 오믹(Ohmic)모드로 전파모드가 전환됨을 알 수 있었다. 이 모드 전이를 위한 채널 하부의 문턱(threshold) 전자 밀도 값은 $5 - 8 \times 10^{17} \text{ cm}^{-3}$ 로 나타났으며, 이 조건은 전기전도도가 높은 물에서 더 빨리 충족되었다. 절연파괴가 일어나는 순간에 채널 상부(channel head) 영역에서 측정된 전자밀도는 매우 높아($\sim 10^{19} \text{ cm}^{-3}$) 채널의 길이방향을 따라 약 4배만큼의 전자밀도 변화가 나타났다. 측정된 전자밀도 값과 함께, 그림자 촬영법으로 관찰된 초기 스파크 채널의 반경 방향 구조는 전산모사를 이용한 연구에 활용되었다.

스트리머의 특성을 충격파 형성과정과 연관시키는 포괄적인 이해를 위하여 일차원 스파크 방전 전산모사 모델을 집중적으로 사용하였다. 동축케이블의 길이를 달리함으로써 스트리머-아크 전이의 속도를 제어할 수 있었으며, 펄스 성형 효과(pulse shaping effect)는 스파크 채널 확장의 초기 단계에서 특히 두드러졌다. 이와 관련하여, 전산모사 모델은 동축 케이블을 알파벳 T 형태로 조립된 저항, 인덕터 및 커패시터를 포함하는 작은 조각들의 직렬 조합으로 간주하여 전송선 내부에서 이뤄지는 전력전송 과정을 효과적으로 계산할 수 있도록 개선되었다. 향상된 전산모사 결과는 아음속 스트리머가 초기 스파크 채널의 형태와 조성을 결정하므로 충격파 생성에 핵심적인 역할을 함을 보여준다. 실제 실험에서는 초기 스파크 채널에 전도성이 높은 코어영역이 차가운 외층에 둘러싸인 모습이 관찰된 바 있다. 이에 상응하는 플라즈마 밀도, 온도분포에서는 완충작용을 하는 외층이 충격파의 생성을 지연시킨다. 더욱이, 초기 온도가 높은 중심부의 압력이 이 외층에서 감쇠되므로 스파크 채널의 초기 팽

창운동은 동축 케이블의 펄스 성형효과에 의하여 한층 더 영향을 받는다. 이에 따라, 절연과괴 전압에 따른 충격파 세기의 변화경향이 케이블 길이에 매우 크게 의존하는 측정결과를 전산모사 결과를 통해 성공적으로 설명할 수 있었다. 충격파 전면의 특성을 대부분 결정하는 스트리머-아크 천이의 초기 구간에서 상대적으로 낮은 플라즈마의 온도에서는 복사선 흡수거리 (absorption length)가 플라즈마의 크기보다 충분히 길다. 따라서 충격파의 생성과정은 플라즈마 체적내부에서 일어날 수 있는 복사선의 재흡수를 고려하지 않더라도 효과적으로 설명할 수 있다. 또한, 전류의 상승률이 더욱 높아진다 하더라도 복사열로 손실되는 에너지 역시 급격히 증가하므로, 스파크 채널 및 물의 운동에너지로 전환되는 에너지 비율은 크게 감소할 것임을 알 수 있다.

Keywords; 수중 펄스 스파크 방전, 충격파, 스트리머-아크 천이, 사전 절연과괴 가속, 음극 아음속 스트리머, 전기분해, 자기일관적 전산모사, 전송선 모델

학 번: 2012-21007